Preparations for the Measurement of the Pointing Precision of a CTA Mid-size Telescope Prototype Using CCD Cameras

-

MASTERARBEIT

zur Erlangung des akademischen Grades
Master of Science
(M. Sc.)
im Fach Physik

eingereicht an der
Mathematisch-Naturwissenschaftlichen Fakultät I
Institut für Physik
Humboldt-Universität zu Berlin

von
Frau Sandra Grünewald
geboren am 07.08.1987 in Oranienburg

Gutachter:

1. *Prof. Dr. Thomas Lohse*
2. *Prof. Dr. Alexander Kappes*

eingereicht am: *15.April 2013*

Abstract

The Cherenkov Telescope Array (CTA) will pioneer a new era of Imaging Atmospheric Cherenkov Telescopes (IACTs) since the project will allow studies in the very-high-energy γ-ray Astronomy with unprecedented accuracy. In order to achieve a high precision, CTA will consist of two telescope arrays which are composed of three different telescope sizes. The construction of a prototype for the Medium Size Telescope (MST) is almost completed in Berlin Adlershof. This prototype will be equipped with several test devices to study the telescope's performance, e.g. a set of five Charged Coupled Device (CCD) cameras. One of these cameras will be directed towards the sky to support the identification of the telescope pointing. For this purpose, the used CCD camera and two diverse optics were investigated. The optics differ in the size of the provided field of view and allow the detection of a different number of stars. The center of gravity of one star or rather the center of gravities of several stars are used for an orientation in the sky. The single star method is compared with a multiple star method, known as astrometry, via star measurements to ascertain a precise procedure for the telescope pointing. In addition, conclusions for the accomplishment of further measurements could be drawn from the analysis of the images.

Zusammenfassung

Das Cherenkov Telescope Array (CTA) wird eine neue Ära von abbildenden atmosphärischen Cherenkov Teleskopen einleiten, da das Projekt Studien in sehr hohen Energiebereichen der γ-Astronomie mit noch nie dagewesener Präzision durchführen wird. Um die hohe Präzision von CTA zu erhalten, wird es zwei Anordnungen mit mehreren Teleskopen geben. Drei verschiedene Teleskopgrößen sorgen für die vollständige Abdeckung des Energiebereichs. Der Prototyp eines mittelgroßen Teleskops (Medium Size Telescope - MST) ist in Berlin Adlershof nahezu fertig gestellt. Er wird mithilfe von verschiedenen Prüfgeräten, zum Beispiel mit fünf CCD Kameras, bestückt sein, um die reale Umsetzung des Teleskops zu überprüfen. Eine dieser CCD Kameras wird dabei direkt auf den Himmel zeigen, um die Ausrichtung des Teleskops zu ermitteln. Aus diesem Grund sind die genutzte CCD Kamera und zwei verschiedene Optiken näher untersucht worden. Die Optiken unterscheiden sich durch die Größe ihrer Sichtfelder, mit deren Hilfe man verschiedene Anzahl von Sternen detektieren kann. Das Zentrum eines Sterns bzw. die Zentren mehrer Sterne können zur Orientierung am Sternenhimmel genutzt werden. Für die Ermittlung eines genauen Messverfahrens für das Ausrichten des Teleskops wurde die Einzelstern-Methode mit der Multiplenstern-Methode (Astrometrie) anhand von Messungen verglichen. Außerdem, anhand der analysierten Bilder der Sterne Schlussfolgerungen für weiterführende Messungen gezogen werden.

Contents

List of Figures

List of Tables

Introduction

For several thousand years men had striven to identify the celestial objects around us. Since the ancient world, astronomy has become a fundamental principle of science. Due to a high technical development observational astronomy today exceeds the visible light range which makes it even more important to know where celestial objects are monitored.
Since the 1980's the most energetic part of the electromagnetic spectrum, the γ-rays, which are created by celestial events, e.g. supernova explosions, have been observed. The observational technique is based on the monitoring of Cherenkov light which is created when γ-rays hit the atmosphere and is carried out by Imaging Atmospheric Cherenkov Telescopes (IACT). There are currently three operating IACT systems, H.E.S.S., MAGIC and VERITAS, which cover different energy ranges.
A new project called Cherenkov Telescope Array (CTA) will combine the different energy ranges. To achieve this combination, arrays of three different telescope sizes on different locations on the Earth surface will be built. The Middle Size Telescope (MST) prototype is currently under construction in Berlin Adlershof. Several measurements will be established on this prototype in order to test the performance of the telescope before it is fabricated in a large number. The optical measurements are carried out by Charged Coupled Device (CCD) cameras. A specific camera, the sky CCD, will support the telescope's pointing since it will identify the camera's field of view in the sky.
During this thesis, the used equipment and the method for orientation in the sky were elaborated to achieve a high performance on the prototype. The characteristics of the CCD camera which is part of the equipment of digital imaging was contemplated which is demonstrated in this thesis. Also, the optics, represented by a zoom objective which was manually changed in order to achieve a higher focal length, was investigated further. During measurement tests on celestial objects the zoom objective showed several improper behaviors concerning image formation, therefore it was dealt with the specification of a suitable optics. The problems according to the optics led to the acquisition of a new objective which provides a bigger field of view in comparison to the zoom objective. A greater field size established the basis for a higher number of detected stars.
As the use of the zoom objective was accompanied with an orientation method in the sky via a single star, the new objective offers the opportunity for a more accurate and flexible orientation method using multiple stars. For this purpose, the astrometry method was proposed, which uses at least three reference stars in the field of view for the identification of the imaged sky.
After characterizing the equipment in the laboratory and theoretical elaborations on the method, practical star imaging tests were accomplished in order to evaluate their practicality at Berlin's night sky. The positive tests led to results which can be used for measurement adjustments in the future e.g. the estimation of exposure

times based on measurements and calculations of the bright star Vega.
The thesis concludes with measurement proposals to improve the pointing method further and gives an estimation of the usability of the optical system for the CTA project based on the comparison between imaging devices concerning pointing on other IACT projects.

Chapter 1

γ-ray Astronomy

1.1 Introduction

Victor Hess is one of the most important scientists since he pioneered astroparticle physics when he discovered charged cosmic rays about 100 years ago. Although a century has passed since the discovery, one of the biggest questions remains concerning the origin of those cosmic rays.
During the last two decades Astroparticle Physics was fast-paced as the observational techniques improved continuously. Even so, the identification of the origin of charged particles remains a challenge because they are deflected repeatedly on their way to the Earth. For this reason Astroparticle Physicists rely on the uncharged particles like neutrinos (ν) and gamma rays (γ) to identify sources in the universe. The detection of γ-rays led to a new field of research: the γ-astronomy.
The most energetic quantum in the electromagnetic provides an insight into the most energetic processes and phenomena of our universe. The energy of the γ-rays ranges from several 100 keV to more than 100 TeV. This energy range gives the possibility for two different detection techniques.
The first one is a direct measurement method which is not possible on the surface of the Earth as the atmosphere is opaque. The method is carried out by "spaceborne γ-ray experiments", e.g. satellites and high altitude experiments. These experiments have only a small effective area since they are subject to mass limitations due to the fact that they have to be launched to space. One example is the the Fermi satellite with the Large Area Telescope (LAT) [AAA$^+$09c] which has been examining the sky since 2008. During this measurement period the Fermi Collaboration was able to reconstruct a sky map, shown in Fig. 1.1, of our Milky Way with several thousand γ-ray sources.
The map shows a bright emission in the center of the image which follows the plane of the Milky Way. Moreover, bright pulsars and active galactic nuclei are scattered over the whole map. The origins and characteristics of many sources cannot be understood without the detection of γ-rays. Several sources have been found which have their energy peak in the γ-ray band e.g. pulsars or quasars. Furthermore, neutron stars, stellar-mass black holes, supernova remnants cannot be clearly characterized without γ-ray properties as well.
The direct measurement extends only from an γ-ray energy of 500 keV to around 100 GeV [Sch01]. These low-energy γ-rays are absorbed or scattered in the atmosphere. The other technique is carried out by "ground based γ-ray experiments" detecting photons with energies greater than 100 GeV. These experiments are carried out

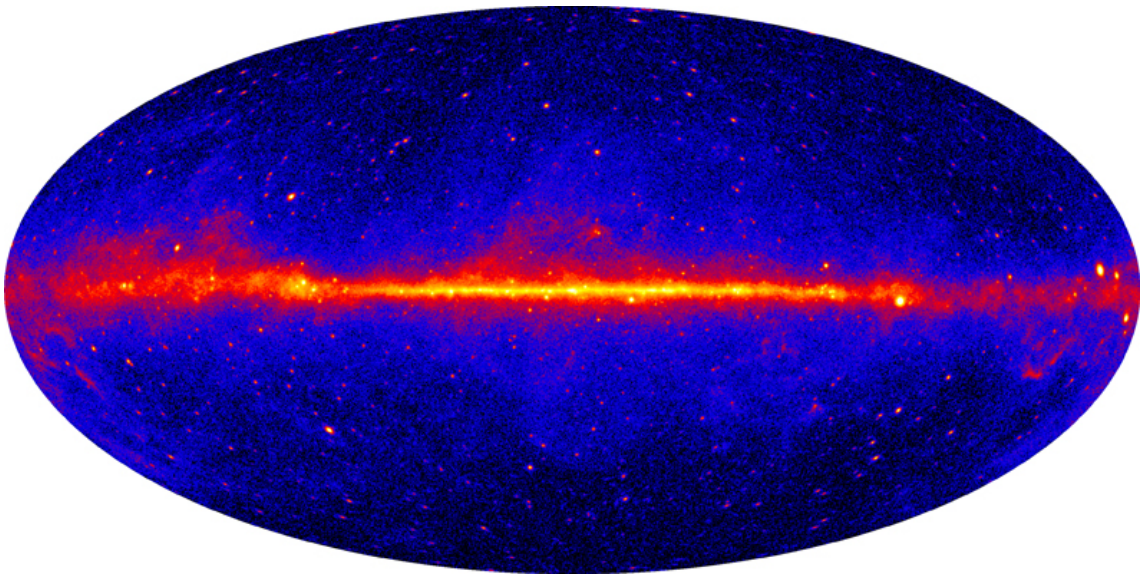

Figure 1.1: This all-sky view from the satellite experiment Fermi LAT reveals bright emissions of γ-rays in the plane of the Milky Way (center), bright pulsars and super-massive black holes [Tea11].

with telescopes which use an electromagnetic cascade produced by very high energy (VHE) γ-rays hitting the Earth atmosphere. The breakthrough of this part of γ-ray astronomy arose in the 1980s when instrumental techniques were developed to detect Cherenkov light which is produced by high energy cosmic ray interactions in the Earth atmosphere.

1.2 Ground based γ-ray Astronomy

The ground based γ-ray astronomy is based on the detection of Cherenkov light which is emitted by electrons when γ-rays strike the Earth's atmosphere. The detection technique is comparatively inexpensive and easy to carry out since Imaging Atmospheric Cherenkov Telescopes (IACTs) merely consists of a mirror like reflector and several Photomultiplier Tubes (PMTs) [VFB07]. The following paragraph shall give a small introduction to the technique of ground based γ-ray astronomy.

1.2.1 Electromagnetic Air Showers

Particles coming from an intergalactic source interact vigorously with the molecules in the Earth's atmosphere and initiate two basic types of showers. Due to the thickness of the atmosphere it is not possible for primary cosmic rays to reach the Earth's surface unaffected. If a hadron reaches the atmosphere it will mostly interact with the atmosphere via the strong force which will result into an hadronic shower. Whereas electrons and photons induce an electromagnetic shower as they are interacting via the electromagnetic force. The development of electromagnetic showers will be described in more detail as they are produced by γ-rays.
The predominant interaction in an electromagnetic cascade is pair production. This describes the transformation of a photon into an electron-positron pair which can only appear in the presence of a third body to conserve the momentum and the energy. After the γ-ray hits the atmosphere its energy is transfered to a resultant

electron-positron pair which is emitted in the forward direction.
After traversing a certain radiation length the particles interact with air molecules and transfers a part of its kinetic energy to a secondary γ-ray produced via bremsstrahlung. The process continues trough the atmosphere with an increasing number of secondary electrons, positrons and γ-rays up to the shower maximum when the mean energy approaches the critical energy $E_0 \approx 80$ MeV in air. At this point the energy is dissipated by ionization and excitation rather than by bremsstrahlung. The shower typically vanish at an altitude of roughly 10 km above sea level. In Fig. 1.2 this shower process is illustrated.

As the electromagnetic cascade is tightly bundled along the projection of the origi-

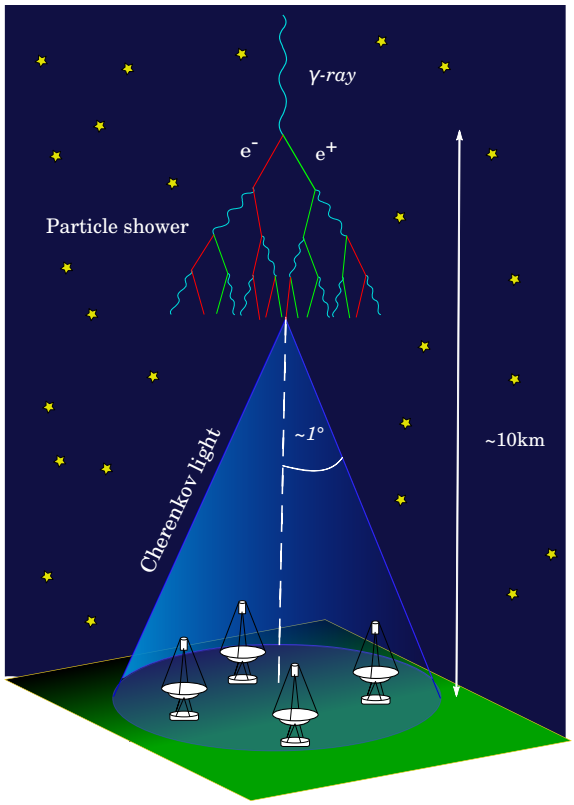

Figure 1.2: If a γ-ray hits the atmosphere it will lead to pair production and bremsstrahlung due to interaction with the atmosphere. An electromagnetic cascade is produced. One side-effect is the emission of Cherenkov light. Due to this effect air showers can be detected by Arrays of Imaging Atmospheric Cherenkov Telescopes.

nal γ-ray it can be easily distinguished from e.g. hadronic cascades [AKL+96]. After detecting the cascade astronomers are interested in determining [Wee03]:

- the origin of the particles to construct a map of their sources,
- the energy to ascertain the energy spectrum and
- the time of arrival to know the variability in the emission.

1.2.2 Cherenkov Radiation

The velocity v of the generated secondary particles is often greater than the speed of light in air c_n

$$v \geq c_\mathrm{n} = \frac{c}{n}, \tag{1.1}$$

which is given by the ratio of speed of light c and the index of refraction of air n. Due to the abrupt change in the electric field near an air molecule when the particle passes by, the atoms emit the so-called 'Cherenkov radiation'.
Outward from the particles direction the radiation is concentrated into a cone which is shown schematically in Fig. 1.3. Based on the sketch the half opening angle Θ of

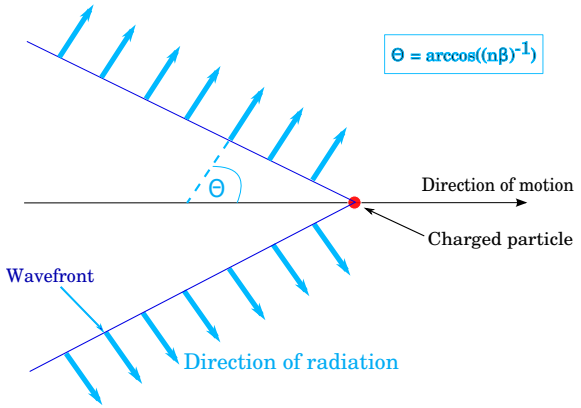

Figure 1.3: If a charged particle traverses the air faster than the speed of light the air molecules will emit the so-called 'Cherenkov radiation' due to an abrupt change in the electric field of the air molecule. The angle θ is the half opening angle of the produced Cherenkov light cone.

the cone is calculated by

$$\Theta_C = \arccos(\frac{1}{n\beta}). \tag{1.2}$$

The typically yielded Cherenkov light is two to three times that of the primary particle (hadron, electron or photon) of the same energy. Moreover the light is emitted from the charged particles in the shower which have an energy above the Cherenkov threshold. For electrons and positrons the threshold corresponds to a kinetic energy [Gru05] of

$$E_{\text{kin}} = E_{\text{total}} - m_0c^2 \approx 21 \text{ MeV}. \tag{1.3}$$

In order to examine the air showers the Cherenkov light is recorded by so-called Cherenkov telescopes.

1.2.3 Cherenkov Telescopes

The principle to examine γ-rays is based on the detection of Cherenkov light, which is spread over a radius of r $\approx$ 120 m assuming an opening angle of the Cherenkov cone (cf. Eq. 1.2) around $\Theta_C \approx 1°$ [Gru05]. Cherenkov detectors are often constructed with a parabolic mirror which collects the light. For recording the light typically a set of photomultipliers is located at the focal point of the mirror.
Due to the relatively large angular size of the Cherenkov emission from a shower the telescopes do not need the standards of optical astronomy and are therefore comparatively inexpensive.
For maximizing the sensitivity of a Cherenkov light detector the light collecting area should be as large as possible. In γ-astronomy a preferred method to get large light collecting areas at low costs is the use of an tessellated composition of spherical mirrors with the same focal length. If these mirrors are located on an optical

support structure with the same radius of curvature as two times the focal length (Davies-Cotton design [DC57]) a decent image will be gained. The disadvantage of this construction is a spread of the arrival times of Cherenkov photons.
The individual mirrors have typically either a round (inexpensive) or a hexagonal (complete coverage of the mirror area [BCC+03])shape. For a better ultraviolet response the mirrors, which are made of e.g. glass, can have an aluminized front. Moreover, a fast, ultraviolet sensitive and widely-used light collector for recording the Cherenkov light is needed. A common choice with such characteristics at low costs are photomultiplier tubes (PMTs) although they are easily damaged by excessive light. Several PMTs represent the camera of a Cherenkov telescope [WT77] and within each pixel the light level is recorded. Using the geometrical and physical properties of the air shower the incoming particles can be characterized.
A detection area of $5 \cdot 10^4$ m^2 [Wee03] results from the radius of the Cherenkov light pool on the ground. This area is used for multiple telescopes which are combined to an array of Imaging Atmospheric Cherenkov Telescopes (IACT) that takes several images of the same shower which overall increases the precision of the measurement. The present generation of IACTs has in recent years opened the realm of ground based γ-ray astronomy in the energy range above 50 GeV. Three of the current major IACTs are VERITAS, MAGIC and H.E.S.S. that will be mentioned further in this thesis.
The Very Energetic Radiation Imaging Telescope Array System (**VERITAS**) operates in southern Arizona, USA. It is an array of four 12 m optical reflectors which were designed based on the Whipple telescope which has been running since 1968 in Arizona. VERITAS is constructed with the highest sensitivity in the 50 GeV to 50 TeV band with a maximum sensitivity between 100 GeV and 10 TeV. The covered field of view of the telescope is 3.5° [Adm13].
The same field of view is covered by the Major Atmospheric Gamma-ray Imaging Telescope (**MAGIC**) which is located on La Palma, Canary Islands. MAGIC includes two 17 m telescopes being 85 m apart from each other with a maximum sensitivity between 50 GeV and 30 TeV. It was the largest Cherenkov telescope before H.E.S.S. II was built which is so far with a diameter of 30 m the biggest IACT [Wag12].
The High Energy Stereoscopic System phase II (**H.E.S.S. II**) in Namibia was recently updated with an additional 30 m diameter telescope. Before the update the array operated with four telescopes 120 m apart from each other each of which has a 12 m diameter optical reflector. The four small telescopes of the H.E.S.S. II experiment have a field of view of 5° whereas the large telescope reaches a field of view of 3.5°. The detected energy ranges from several tens of GeV to several tens of TeV [Col13]. An image of the H.E.S.S. II array is shown in Fig. 1.4.

1.2.4 Pointing at IACTs

For an exact definition of the origin of an individual γ-ray the precise measurement of the location where the telescope points to is a significant challenge for γ-ray astronomers. The necessity of a proper pointing accuracy is demonstrated by the example of the Blazar 3C66A. After a measurement period of MAGIC I in 2008, the blazar was classified as a BL Lacertae object [AAA+09b]. The BL Lacertae objects are typically characterized by an energy peak at E > 100 GeV. But at that particular time two objects, including Blazar 3C66A, were detected with an atypi-

Figure 1.4: One of the present generation IACTs, H.E.S.S. II, consists of four 12 m *telescopes located on the corners of the array. In the center stands the recently added fifth telescope with a* 30 m *reflector [Wik12b].*

cal high-frequency peak at an energy of E $\approx$ 200 GeV. Hence the MAGIC I group concluded the existance of another source in the field of view of the telescope which emits more energy than a BL Lacertae object. As the pointing on MAGIC I was not accurate enough the galaxy 3C66B, which is 0.12° apart from the Blazar, seemed a legitimate solution for the origin of those VHE γ-rays.
In 2009 the VERITAS group disproved MAGIC's solution as their pointing method concluded an emission coming only from the blazar [AAA$^+$09a]. Even the MAGIC collaboration made the same conclusion after the update to MAGIC II. The additional telescope of the MAGIC II array pioneered a more precise pointing measurement [AAA$^+$10] even though the observation time was relatively small.
This example shows the significant role of a pointing measurement with high accuracy at IACTs and shows the need for further investigation in this domain.

Chapter 2

The Cherenkov Telescope Array Project

The Cherenkov Telescope Array (CTA) [AAA+11] will be a next generation ground based VHE γ-ray instrument which will investigate non-thermal processes among others in the universe. For covering an energy range between several GeV and a few TeV the array will consist of at least three different sizes of telescopes. The majority of the telescopes will be dedicated to the medium energy range of 100 GeV to 1 TeV which therefore requires careful considerations and investigations concerning costs and performance. For those investigations a medium-sized telescope (MST) prototype is currently built in Berlin Adlershof on which different measurements will be done to determine the behavior of the telescope structure that are presented in this section.

2.1 Introduction

The CTA project will provide a deep insight into the non-thermal high-energy universe. For a high efficiency the project will serve as an open observatory with a transparent access to data, analyzing tools and user trainings. Moreover the experiment will operate in close cooperation with other experiments which investigate other wavelength ranges of the electromagnetic spectrum and other messengers, e.g. neutrinos.
The design of CTA foresees an improvement in the VHE γ-ray regime of five to ten times in sensitivity compared to the currently operating IACTs. Furthermore it will extend the accessible energy range below 100 GeV and above 100 TeV [Her10]. The achievement of high sensitivity will be the result of an array of many tens of telescopes detecting the air showers induced by a γ-ray over a large area on the ground. Up to now most of the showers are only detected by two or three telescopes over a small area. In contrast, the much larger number of telescopes in CTA will provide a higher number of views of each shower and suppress the background of cosmic ray events which will improve the angular resolution significantly [BCS08].
A possible design scenario for CTA, allowing a full-sky coverage, is the construction of telescopes in the northern and southern hemisphere [AAA+11]. The greater array, which will be spread over an area of a few square kilometers, forsees a construction on the southern hemisphere with three different sizes of telescopes. In order to cover the full energy range different mirror sizes for the telescopes are planned. The array focuses on the wealth of sources in the central region of our Galaxy and the

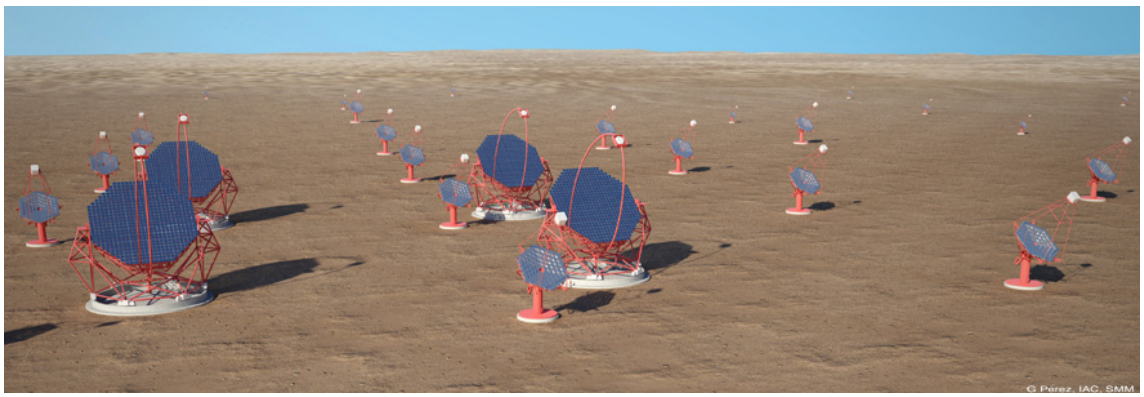

Figure 2.1: An artist's view of the CTA project in the southern hemisphere. For an optimum shower detection three telescopes sizes (large, medium and small) are required. Four LSTs are surrounded by several MSTs. At the edges of the array a few SSTs are located.

abundance of their morphological features. In contrast, the array in the northern hemisphere will be spread over one square kilometer with only two larger telescope types. Its will be the observation of Active Galactic Nuclei as well as the formation of stars and their evolution.
In order to achieve higher flux sensitivities for deep observations, instruments covering three different energy ranges are developed [AAA+11].
The high sensitivity in the range of a few ten GeV up to 100 GeV is carried out by the development of the **Large Size Telescope (LST)** [TBS+11], an instrument of 24 m in diameter. The array includes three to four telescopes with a moderate field of view about $4 - 5°$ spaced 100 m apart which will give the highest performance for this energy domain.
In contrast, to the LST will the **Small Size Telescope (SST)** [VCM+13] focus on γ-rays over 10 TeV and operate only in the Southern hemisphere. At higher energies the amount of emitted light is also higher therefore the showers can be detected beyond the radius of the Cherenkov light pool. An appropriate performance will be achieved if the telescopes with a possible diameter of four to six meters and a field of view of around 10° are distributed over several square kilometers. Currently investigations are carried out about possible structures which will give the highest performances at low costs.
To cover the "core" energy range of 100 GeV to 1 TeV a **Medium Size Telescope (MST)** is the detector of choice and will make up the majority of instruments. An artist's view of an array of the CTA experiment in the Southern hemisphere is shown in Fig. 2.1.

2.2 Medium Size Telescope (MST)

Although the shower detection and reconstruction is well-known from former experiments, the requirements for an array of MSTs [D+] will be much more specific:

- each telescope with diameter of $10 - 12$ m
- each telescope's field of view $6 - 8°$
- a sensitivity down to a milli-Crab

- use of grid of telescopes with a spacing of 100 m in between
- array size larger than the Cherenkov light pool

This results in an improved sensitivity and better shower reconstruction due to the amount of telescopes. Moreover, the the light pool is uniformly sampled which means that a higher number of images can be recorded close to the optimum distance from the shower axis where the light intensity is large and fluctuations are small. The shower axis is also viewed at a sufficiently large angle which leads to a more efficient reconstruction of the shower direction. To meet those requirements, the structure of the telescope needs to be investigated, therefore a prototype of the MST is under construction in Berlin Adlershof.

2.2.1 The MST Prototype

The DESY (Deutsches Elektronen Synchroton) at Zeuthen and Humboldt University's Physics Department are currently working on the establishment of the prototype in Berlin Adlershof which is planned to be fully constructed in spring 2013. The main goal of the prototype is a design test of the mechanical structure, the drive system, the Active Mirror Control (AMC), software [BCH$^+$12] as well as the calibration [BBG$^+$12] and commisioning.
The constructed telescope has a modified Davis-Cotton type reflector with a diameter of 12 m, a focal length of 16 m and radius of curvature of 19 m. In 16 m distance a dummy camera without PMTs is going to be mounted and should resemble the effect of a real PMT camera. In addition a drive system, the AMC, several Charged-Coupled Device (CCD) cameras, a weather station and some additional sensors are installed for testing the behavior of the steel structure. Some of the events will be marked with a time stamp via the Network Time Protocol (NTP) or the Global Positioning System for correlating them in the offline analysis.
The purpose of our group's work is the study of fabrication methods, possible costs and providing a test bench for mounting mirrors. For this reason realistic operation scenarios of the prototype are going to be emulated [OBB$^+$12].

2.3 Measurements on the MST Prototype

The observation of the steel structure and the test devices on an operating telescope requires different measurement tools. Concerning the dynamics of the steel structure, non-optical sensors are used, whereas specific observations as for example the dummy camera or the mirrors are examined via optical devices.

2.3.1 Non-Optical Measurements

The five types of non-optical sensors [Sch13] are widely distributed over the whole telescope as is illustrated in Fig. 2.2.
Acceleration sensors will measure the vibrations caused by winds and telescope movements on two main locations, on a quad tube at the rope connection where forces stress the tubes the most, and at one important CCD camera.
Inclination sensors will monitor the bending on the upper tower, on different locations on the dish and mirrors.
A **combination** of **acceleration** and **inclination sensors** will be installed on

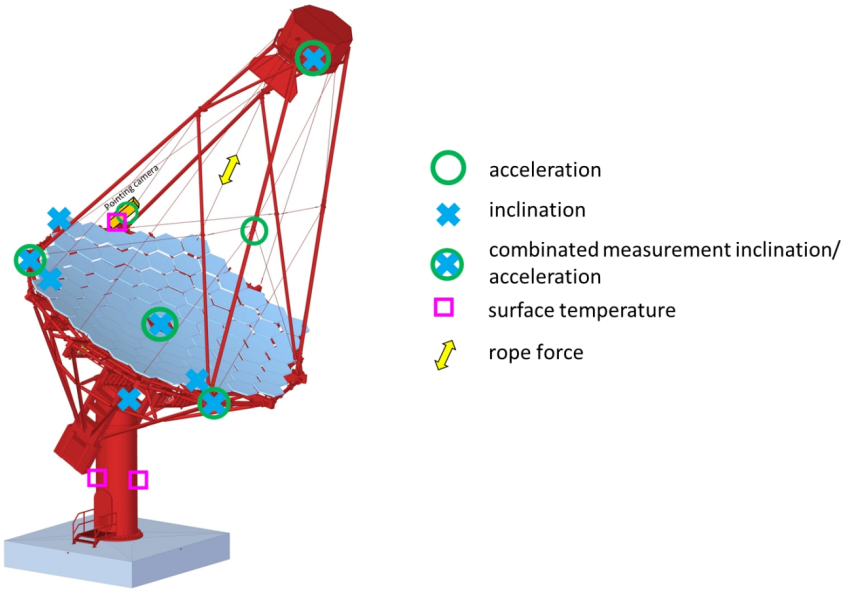

Figure 2.2: The MST prototype based upon a modified Davies-Cotton design highlighted with several markers where non-optical sensors will monitor the steel structure at points where the structure is stressed the most [Sch13].

the dish and the dummy camera for the examination of gravitational influences at different elevation angles. Additional sensors monitor the **surface temperature** of the steel structure and the **tension** of the connection **ropes**.

2.3.2 Optical Measurements

The most important tool for checking different tasks of the prototype is a set of CCD cameras which are distributed over the whole telescope as shown in Fig. 2.3. Each camera is assigned to a different measurement purpose for the prototype.

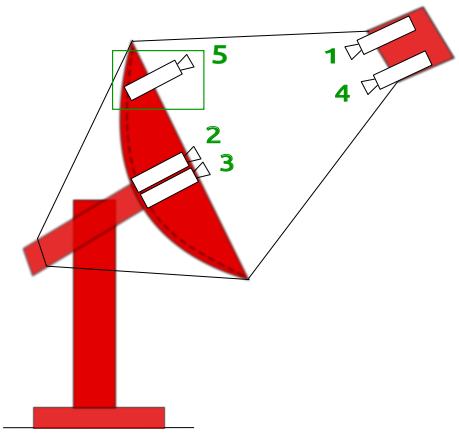

Figure 2.3: Five CCD cameras are distributed over the whole prototype to perform optical measurement tasks. The framed CCD camera is the sky CCD which is studied closer in this thesis.

The cameras labeled with the numbers **1** and **2** will support mirror alignment. For this purpose CCD camera **1** on the dummy camera will image all mirrors on the dish in order to verify that every mirror is fully illuminated by star light which is comparable to a method the VERITAS collaboration uses [MHKM10].

In contrast, camera **2** in the middle of the dish focuses the lid of the dummy camera. This resembles the H.E.S.S. mirror alignment where each mirror is adjusted so that the reflected light spot of a star is centered in the middle of the camera lid [CGJ+03]. After the mirror alignment camera **3** will carry out a point spread function (PSF) measurement and vibration observations for which a white screen with LEDs in its corners will be installed on the camera dummy. On the screen the reflected star light from the mirrors can be easily observed and additionally the movement of the LEDs gives information about camera vibrations.
Camera **4** observes camera **5**, the sky CCD, which is equipped with LEDs to monitor possible movements of the camera. The sky CCD is needed for pointing to a star which is explained in the next chapter.
All data will be stored in a data base and can be accessed later on especially the CCD images will be written into a widely-used data format, the standard astronomical FITS (Flexible Image Transport System) data.

2.3.3 Telescope Pointing

After aligning the axis of the sky CCD camera which is located five metres away from the dish center [Bae12b] with the telescope axis, the telescope will be driven to a star with well-known coordinates until it appears in the field of view of the sky CCD. From this point on, the star will be tracked by the whole telescope to adjust the telescop mirrors in a way that the light of the star is concentrated on the white screen of the dummy camera. Images are recorded by the sky CCD and CCD camera 3 which monitors the screen. Afterwards, the relative position of the star's center of gravity in the recorded image of the sky CCD is determined in order to match the position with the image of the star's PSF via coordinate transformation. Due to this approach the pointing of the whole telescope is determined. To achieve a high precision, stars on different azimuth and altitude are going to be imaged. During those observations the steel structure and the pointing camera are monitored, thus the irregularities can be considered in the offline analysis and the true pointing of the telescope will be ascertained.
Concerning the pointing of the sky CCD two different methods can be considered: a single star and a multiple star method. The single star method uses only one well-known star for the identification of the sky CCD's field of view. The motion of the star can be monitored in order to make a statement of the position change of the PSF. In comparison, the multiple star method uses at least three stars in the sky CCD's field of view to identify the location of the stars via astrometry. As the stars are also focussed via the telescope, the information for matching the telescope pointing according to the images can be collected with a single adjustment. For convenient execution of the single star method a very small field of view is considered, assuring the recording of only one bright star, whereas for the multiple star method a big field of view is more reasonable. Both methods will be discussed during this thesis in order to evaluate an appropriate choice for the pointing of the sky CCD at the MST prototype.
Moreover, requirements for the MST prototype are set up demanding a post pointing calibration of the whole telescope which should not exceed an uncertainty of 7" (arcsec) [HB12]. To guarantee such high precisions all possible sources of uncertainties have to be analyzed precisely.

Chapter 3

CCD Cameras at the MST Prototype

The preferred image recording devices for the MST prototype are CCD cameras. This is due to the fact that they proved in previous experiments to have moderate sensitiviy at reasonable costs, a connection to a computer, etc. In this chapter the working principle and characteristics of CCD cameras are outlined. Additionally, the chosen CCD camera for the MST prototype and the planned pointing equipment are presented.

3.1 Working Principle of a CCD Camera

The term CCD describes an electronic light sensor which consists of an array of closely spaced metal oxide semiconductor (MOS) capacitors which are the pixels. There are two basic types of CCDs, the surface channel CCD (SCCD) and the buried channel CCD (BCCD). Charge is stored and transferred at the semiconductor surface in the SCCD, whereas in the BCCD the charge packets are stored and transferred in the bulk semiconductor beneath the surface. Most manufactured CCDs use the buried channel structure today as the charge transport is much faster due to a electrostatic potential which guarantees an exchange of electrons between the valence band and the conduction band without losses [T$^+$98].
The CCDs pixel composition made of a thin n-type over a thick p-type silicon layer is shown in Fig. 3.1 diagram (a). The depletion region in the n-type silicon x_n covers the whole n-layer, whereas it covers only a fraction of the p-type layer x_p. The n-type silicon is protected by a layer made of silicon oxide which is in contact with a metal electrode with a gate voltage V_G for charge transportation.
The collection of the charge within the pixel is based upon the photoelectric effect. If a photon with the appropriate energy $E = h\nu$ hits the CCD, it will be absorbed. The band gap energy of silicon is around $E = 1.14$ eV. So photons in the energy range of 1.14 eV $< E <$ 4 eV are easily absorbed [How06]. Due to the incoming photons electrons are excited to the conduction band and holes are left in the valence band. The holes migrate to the p-type silicon and the electrons are collected in the n-type silicon by a potential well.

The diagram (b) of Fig. 3.1 illustrates the behavior of a BCCD pixel when no charge $Q_{sig} = 0$ has been collected yet. The potential Ψ_{max} describes the maximum

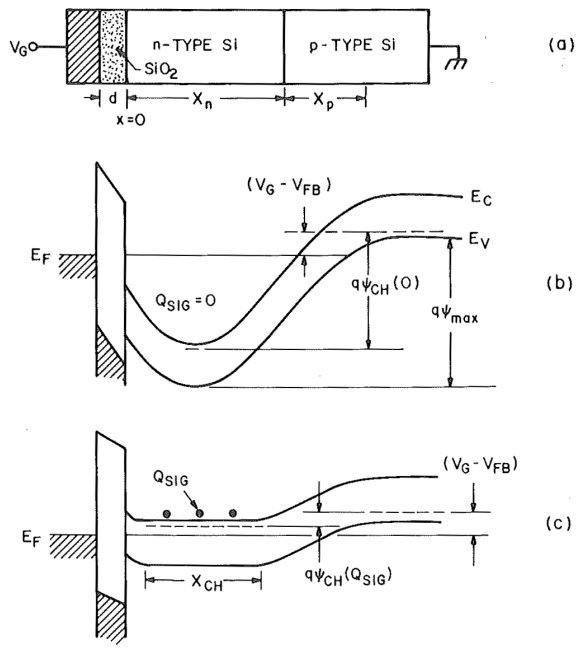

Figure 3.1: The performance of a CCD camera pixel (a) is based on a potential well that depends on the amount of collected charge (no charge collected (b), charge collected (c)) [Sze08].

potential depth in the given pixel and is given by

$$\Psi_{max} = \Psi_J(1 + \frac{N_A}{N_D}) \quad \text{with a junction potential} \quad \Psi_J \equiv \frac{qN_A}{2\epsilon_S}x_p^2. \tag{3.1}$$

It depends on the density of acceptors N_A and donors N_D in the energy-bands, the permittivity of the given material (silicon: $\epsilon_S = 11.68 \cdot \epsilon_0$) and on the length of the p-type layer's depletion region.
If an acceptor concentration of $N_A = 10^{14}$ cm^{-3} and a donors concentration of $N_D = 10^{16}$ cm^{-3} [SHLK87] is considered for a 1 μm thick n-type and $20 - 30$ μm large p-type layer with a depletion region of $x_p \approx 10$ μm, the maximum potential depth will be in the order of $\Psi_{max} \approx 8$ V. The more fundamental effectiveness of the CCD pixel results from the applied gate voltage V_G which typically varies from 0 to +15 V [SHLK87] since it defines the potential Ψ_{CH} until read-out occurs. In diagram (b) of Fig. 3.1 the potential has its maximum as no charge has been collected yet whereas in diagram (c) the charge has been collected as a result of the potential well and therefore the potential reaches the minimum until it is read-out. This means the amount of collected charge will increase if the gate voltage is raised since the potential well gets depper.
The read-out process itself is sophisticated since each pixel consists of three gates which are subpixel sized electrodes with different applied voltages. The voltage of one gate equals zero whereas one other is higher than the main gate voltage. All three electrodes are controlled via a clock circuit. The charge stored in a pixel will be transferred into the pixel above if the gates change their voltage. Each pixel column of the camera is connected in parallel. During one clock cycle the row of pixel values can move up by one row. The top row is then shifted off the array into an output register. At the end each pixel voltage of the shifted row is readout and changed via an analog to digital (A/D) converter into a digital number [How06].

3.2 CCD Camera Characteristics

The **quantum efficiency (QE)** is the percentage of photons hitting the CCD camera that are detected by producing electrons. The CCD device is essentially composed of pure silicon whose response depends on the wavelength.
The behavior of photons in matter is characterized by three main interactions: photoelectric effect, Compton scattering and pair production [Leo94]. The absorption of photons is mainly based on the photoelectric effect which appears in the low energy range between a few eV and 1 MeV. The effect is based on the excitation of an electron from an atom after the absorption of a photon.
In the energy range between several keV and 10 MeV Compton scattering becomes more significant. Compton scattering is the elastic scattering of photons on weakly bound electrons within the material. The interaction is based on scattering und absorption as the average energy is transferred to the recoil electron which turns its energy in the material.
In the high energy range, which begins at twice the rest energy of an electron, pair production increases. It is characterized by the transformation of a photon into an electron-positron pair and therefore is based on absorption.
Concerning the CCD camera the photoelectric effect is the main interaction process for the formation of a photon absorption curve for silicon which mirrors the Quantum Efficiency (QE) curve of a typical CCD device. The silicon absorbs photons according to Beer's law

$$I = I_0 \cdot \exp(-\mu t) \tag{3.2}$$

with the absorption coefficient $\mu = \sigma(N_a \frac{\rho}{A})$ [Dem05]. The equation shows the light I which remains after the incident light I_0 passes through a material. The decrease of light can be described by an exponential function of the product of the absorption coefficient μ and the thickness t of the material.
The absorption coefficient μ can be calculated with the Avogadro constant N_A, the mass density ρ, the Atomic number A and the absorption cross section σ which is characterized by the mentioned physical interactions.
The signal within the CCD can be calculated by multiplying a number of photons falling on a camera pixel with the QE which generates a number of electrons N_e

$$N_e = QE \cdot P. \tag{3.3}$$

This signal is amplified by a factor called **gain**. It is given in terms of a number of electrons needed for producing the precision of one digital number in the A/D converter.
If the corresponding noise sources are understood the **signal to noise ratio** [How06]

$$\frac{S}{N} = \frac{QE \cdot P \cdot G}{\sqrt{(N_P + (n_{pix}(N_B + N_T + N_R^2))}}. \tag{3.4}$$

can be determined which is a comparison between a desired signal to the background noise level.
The main sources of noise within a CCD camera are the sensor readout noise N_R,

thermal noise N_T, backgroundlight noise N_B and photon noise N_P. The readout noise N_R is an inherent property of the sensor. The combination of the process of amplification and the conversion of the photoelectrons into voltage is described by this variable. Furthermore every material is subject to thermal noise N_T at a temperature above 0 K which is expressed as a dark current. If thermal agitation is high enough electrons will be freed from the valence band and collected in a potential well. During the readout those electrons are part of the signal. The variance of this noise is given by Poisson statistics as the square root of charge arising from thermal effects

$$\delta_{dark} = \sqrt{N_T}. \tag{3.5}$$

The dark current is negligible if the CCD is cooled down or is used with short exposures. Additional, photon noise N_P is coming from the effect of the photons P which generate a signal of N_e electrons due to the QE and the gain G. It follows the Poisson statistic and is determined by

$$\delta_{sign} = \sqrt{N_P} = \sqrt{QE \cdot P \cdot G}. \tag{3.6}$$

As the light in an image does not exclusively come from the imaged object, the backgroundlight noise N_B has to be considered in the signal to noise ratio as well. Together with the photon noise and the thermal noise the backgroundlight noise follows the Poisson statistic.
Since the readout noise, the thermal noise and the backgroundlight noise occurs in every pixel these noise factors have to be multiplied by the number of pixels n_{pix} involved in the signal to noise calculation.
If the gain is very high another noise has to be introduced

$$\delta_{gain} = \sqrt{N_G} = \sqrt{G^2 \cdot \sigma_f^2} \tag{3.7}$$

with a factor σ_f, which depends on the internal electrical workings of the A/D converter. Due to this noise CCD cameras are typically used at a low gain.
Another important characteristic of the CCD camera is the **full well capacity** which gives the amount of charge a pixel can hold until the signal leaks out to neighboring pixels. The higher the full well capacity the more accurate the signal.

3.3 The Prosilica GC1350 CCD Camera

For the MST prototype the Prosilica GC 1350 from Allied Vision Technologies was chosen. As this CCD camera has been used at DESY before, an interface and software are already available. This led to the purchase of a series of Prosilica GC1350. The chosen CCD is shown in Fig. 3.2. The specifications for the camera are listed in Tab. 3.1.

The quantum efficiency curve of the used Prosilica camera is given in Fig. 3.3. The curve shows a maximum at around 520 nm with a quantum efficiency up to 38%. Up to 1000 nm the curve decreases roughly exponentially. The best quantum efficiency of this camera is reached in the visible light range.

The camera software used during this thesis was Video Client which is the second

[1]Each pixel is assigned to a numerical value in the computer via an A/D converter. The bit depth determines how finely the signal of one pixel can be divided. The A/D Converter can distinguish between $2^{(\text{bit depth})}$ information levels.

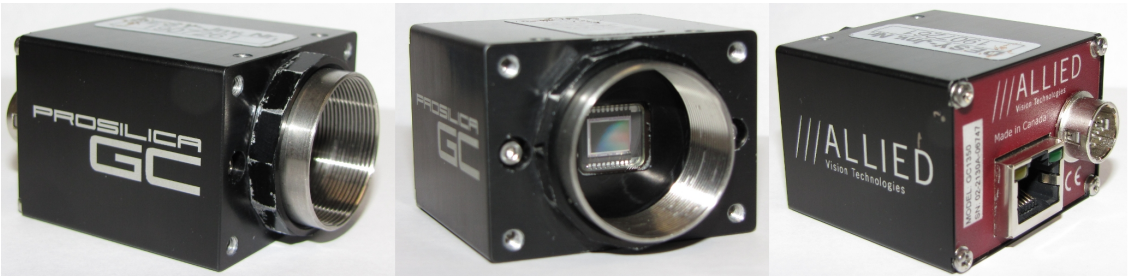

Figure 3.2: The Prosilica GC 1350 CCD camera is used as sky CCD camera. The camera is shown from different angles to discern the C-mount (left), the sensor (middle) and the different connections (right).

Camera	**Prosilica GC 1350**
Sensor	Sony ICX205
Sensor Size	Type 1/2
Chip Size	(1360 pixel x 1024 pixel)
Pixel Size	4.65 μm x 4.65 μm
Bit Depth [1]	8/12 Bit
Gain Range	0-25 dB
Exposure Range	12 μs - 60 s
Mount	C
Interface	Gigabit ethernet

Table 3.1: Some important specifications of the Prosilica GC 1350 CCD camera which is used as sky CCD camera [Doe12].

edition of a program to acquire and analyse video data. The program was developed for the Photo Injector Test Facility (PITZ) at DESY Zeuthen. Its requirements for stable operation are listed in Tab. 3.2.

It is possible to save pictures taken by the camera in BMP or IMC(Image Media

Readout Electronic Requirements	
Data Rate	1 MB/s
Readout Frequency	5 Hz
Network Connection	100 MBit
PC Requirements	Pentium III 1000 MHz processor
Operating System	Windows (7, XP, 2000 and older)
Other requirements	TINE (Three-fold Integrated Network Environment) data protocol

Table 3.2: The requirements for a fluent operation of the Video Client software which is used to take images with the CCD camera [WMD10].

Compressed) format which only supports 8 bit image data.
A tool, called universal slow control, which can change the exposure time and gain was developed by David Melkumyan [WMD10] and was used during the measurement process. It is a Java based controlling tool and is independent of the operating system.

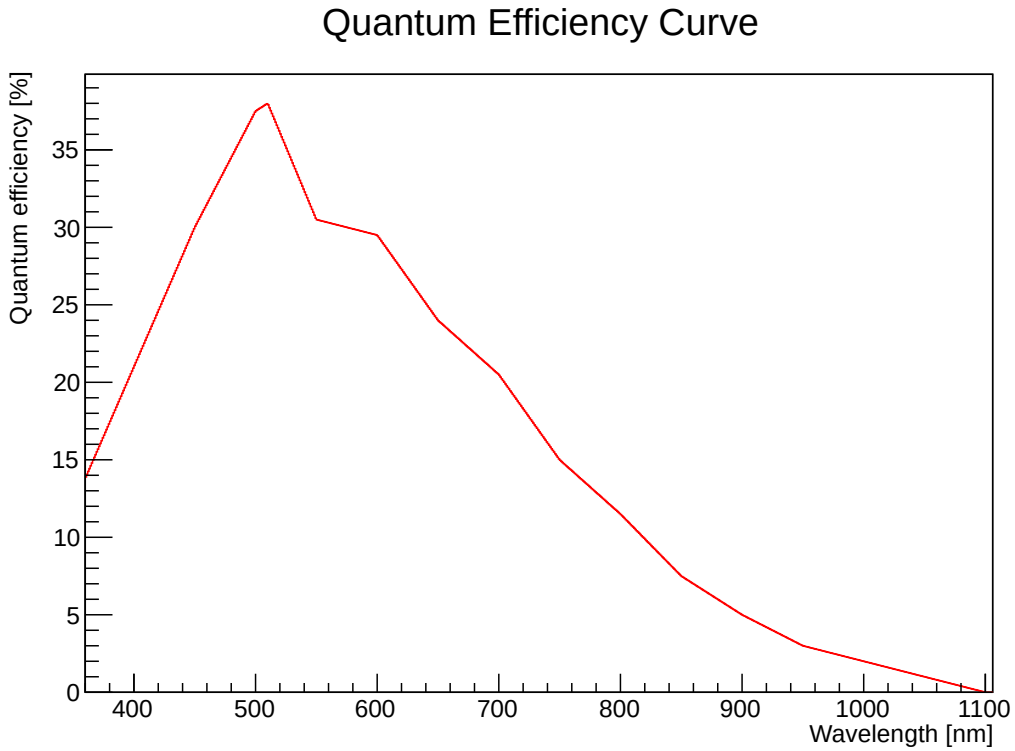

Figure 3.3: The diagram shows the quantum efficiency curve of the Prosilica GC 1350 CCD camera based on the data from the camera manual [Doe12]. The X-axis presents the wavelength, whereas the axis of ordinates shows the quantum efficiency in percent. The highest efficiency of 38% *is yielded at a wavelength of* $\lambda \approx 510$ nm.

3.3.1 Examination of Readout and Thermal Noise

In order to evaluate the image quality and sensitivity of the CCD camera its characteristics were determined and compared with the information from the company (see appendix B).
The different aspects of noise were presented in a previous chapter. The presented photon noise and backgroundlight noise depend on light exposure to the sensor and varies with its time and intensity. Therefore, it is much simpler to measure the noise originating from the CCD camera itself since a variation in dark frames (images where the camera is shielded from light exposure) will only occur if the operating temperature changes. There are two different noise factors: the readout noise according to the CCD's electronics and the thermal noise from the silicon semiconductor which is temperature dependent. Moreover, at higher gains the gain noise N_G is added.
The readout noise is determined from images which were taken with the smallest exposure time possible $t_{small} = 10$ μs since those images are influenced predominantly by the CCD electronics. Afterwards they were analyzed to determine the width of the distributed digital numbers regarding to their occurrence in the image. This width is expressed by the variance which is calculated by

$$\sigma^2 = \frac{1}{N-1} \sum_{i,j} (y_{ij} - \mu)^2. \tag{3.8}$$

Here μ represents the mean of the sample and y_{ij} the pixel value where i is the row index and j the column index . The variance's square root is multiplied by

the amount of electrons theoretically needed to change the digital number in the image by one unit. This value, also known as the inverse overall system gain 1/G, is predicted by the ratio of the full well capacity given by the manufacturer and the highest digital number achieved

$$\frac{1}{\mathrm{G}} = \frac{11737\mathrm{e}^-}{255\mathrm{DN}} \approx 46\frac{\mathrm{e}^-}{\mathrm{DN}}. \tag{3.9}$$

The obtained values depending on the gain is plotted in Fig. 3.4 and is represented by the black data points.
Moreover, two data series of dark images with an exposure time of $t = 10$ ms were recorded to examine additional thermal noise. One sequence was recorded after a camera operation of six hours (green) the other after a prolonged[2] camera use (blue).
The graphs show an exponential increase which rises a bit stronger from gain of

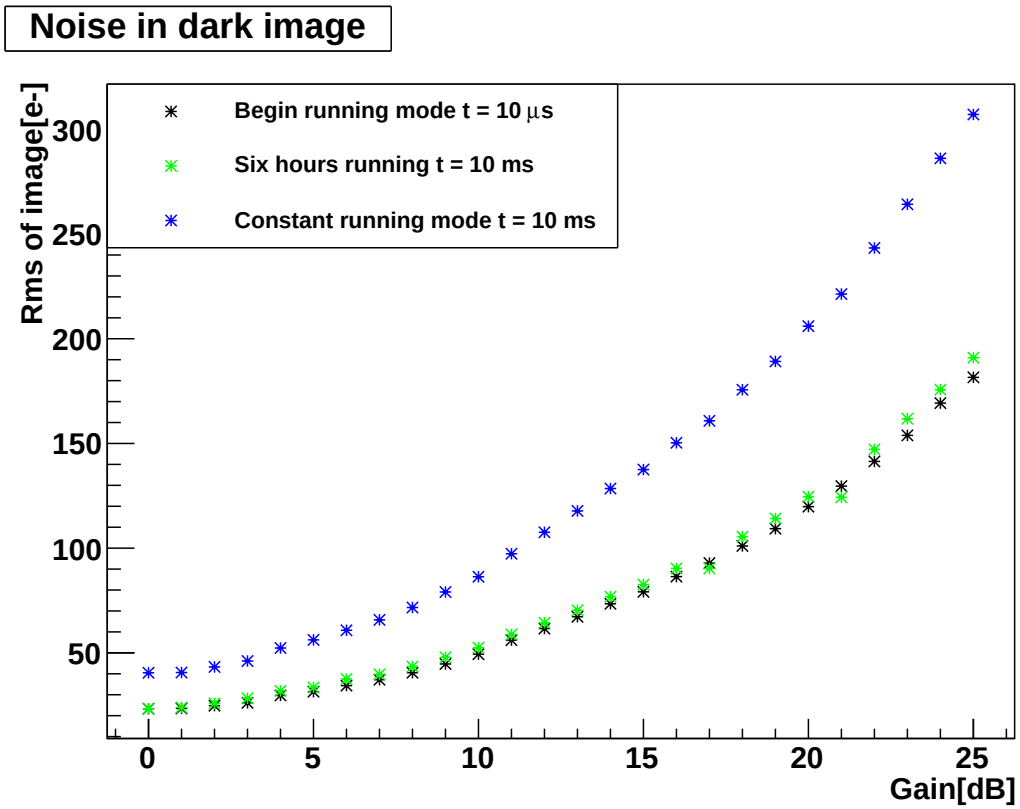

Figure 3.4: The noise of an image represented by the root mean square of the signal (Y-axis). It rises roughly exponentially with the gain (X-axis). At the lowest exposure time of an imaged dark frame (shielded from light) only readout noise affects the root mean square whereas at higher exposures and a longer running mode thermal noise is added.

5 dB since the gain noise is added. The noise after prolonged use (blue) is about twice as high as in the beginning regardless of the gain. It results on the one hand from thermal noise and on the other hand from additional noise related to a feature which tries to suppress thermal noise. This feature is an electronic element which often subtracts an estimated noise value per pixel when the CCD's temperature elevates. As a consequence it also adds noise which is compared to the extent of the

[2]For this measurement the only CCD camera available has been running in Davids office for an undetermined time.

basic thermal noise negligible. Since the differentiation of two noise values is not possible due to a lack of dark current compensation information, only the combined noise can be examined. The noise's onset can already be seen after six hours of use. The manufacturer declares the readout noise at zero gain to be $N_r = 18\ e^-$ which was determined from 12 bit images. In comparison the measurement data yield a readout noise of $N_r = 23\ e^-$ which approximately doubled after a prolonged use to $N_r = 41\ e^-$. Even if the measurement test settings of the manufacturer are different, the readout noise of both measurements have the same order of magnitude.
In conclusion for further measurements the gain will be attempted to be as small as possible since the graphs show a large noise development at high gains. Besides the thermal noise's effect on the whole image is examined more closely in the next paragraph.

3.3.2 Dark Current

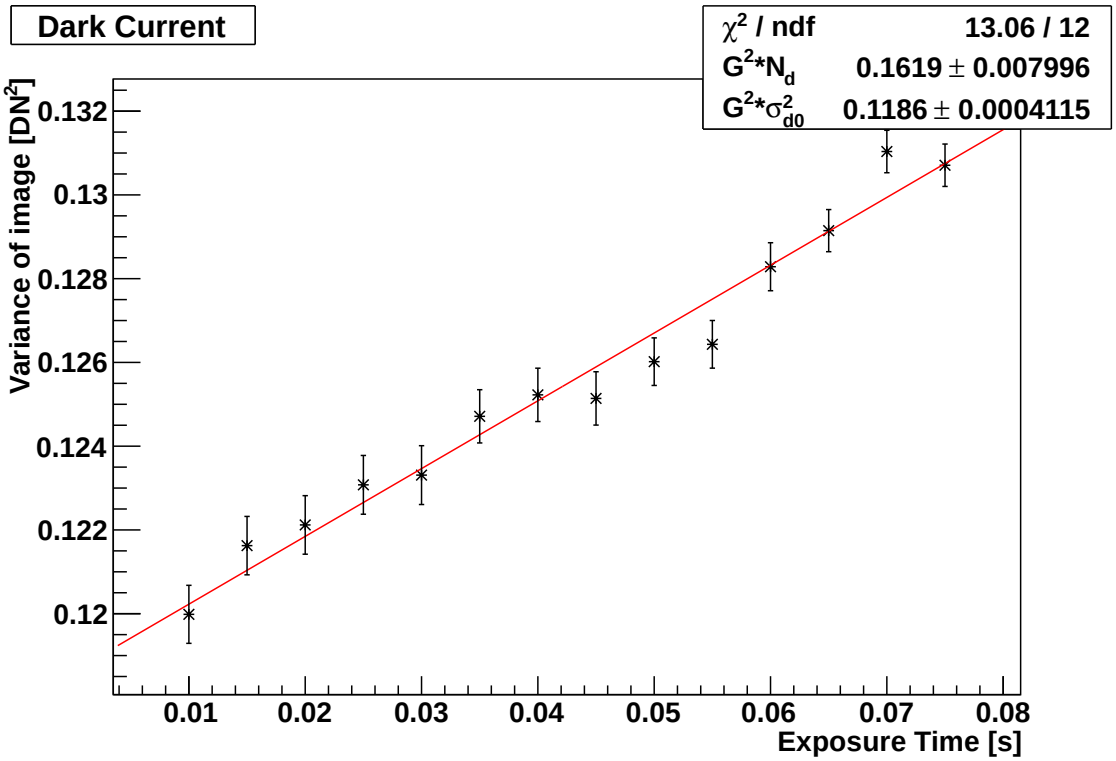

Figure 3.5: Plot of the correlation between the variance of a dark image with the exposure time to calculate the dark current from the slope of the linear regression via the overall system gain G. The dark current describes the thermally generated electrons in the silicon of the CCD camera within a time. The intercept gives information about the pedestal's variance σ^2_{d0} of the images.

Dark current is formed by thermally generated electrons in the silicon during exposure time and adds charge to the pixels while the camera operates. It is highly dependent on the temperature during the operation. Around room temperature the dark current doubles each time the temperature increases by $\sim 8°$ [Die04].
The current's fluctuation is thermal noise which was mentioned in the previous section. As its origin follows a Poisson distribution, the mean number of electrons taking part in the dark current formation equals their variance. However, this is not

the case if a dark current compensation feature is part of the CCD camera. The Prosilica camera offers such a compensator therefore the correspondence

$$N_d = \frac{\sigma^2_{y,temp,dark} - G^2\sigma^2_{d0}}{G^2 \cdot t_{exp}} \tag{3.10}$$

is used for computing the dark current [Die04]. As the feature cannot fully suppress the dark current, the resulting noise depends not only on the dark current. According to the equation, the variance $\sigma^2_{y,temp,dark}$ of a dark image and the corresponding exposure time t_{exp} also are taken into account. The variance was determined in the same way as mentioned before. Afterwards the variance was plotted dependent on the exposure time. The resulting diagram is shown in Fig. 3.5.
A fit based on Eq. 3.10 was applied to the data points where the dark current can be computed from the slope and the offset current from the intercept. By multiplying the slope with the squared inverse overall system gain the rate of thermally generated electrons is obtained. The value was determined as

$$N_d = (343 \pm 17 \pm 18)\frac{e^-}{s} \tag{3.11}$$

with a statistical uncertainty of 17 electrons and 18 electrons arising from systematic errors which were computed by the variation of the slope when data points far away

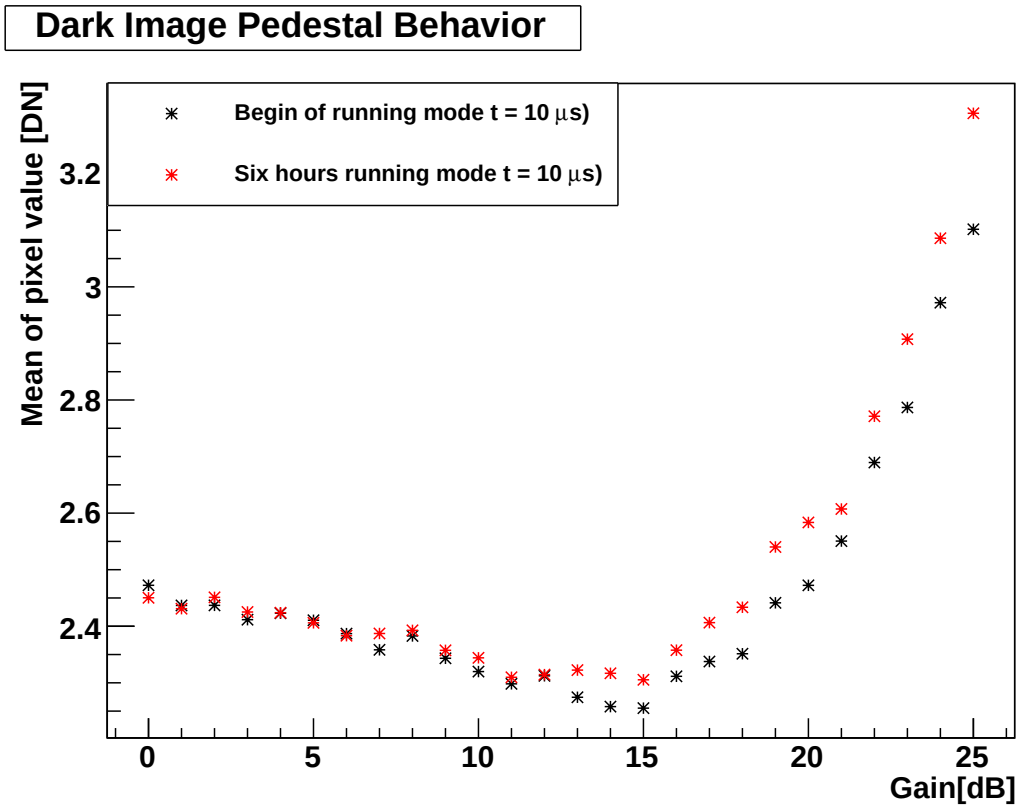

Figure 3.6: The mean pixel value (Y-axis) within a dark frame was ascertained while the gain (X-axis) was increased. The pedestal was examined for a measurement at the beginning of the CCD's running mode (black) and after six hours of running (red). A minor decrease of the data points up to a gain of 15 dB *can be seen wehreas the increase at greater gains is more pronounced for the measurement after several hours of operation.*

from the fit are left out. The company ascertained the dark current as

$$N_d \approx 408 \frac{e^-}{s}. \tag{3.12}$$

Since they did not determine the uncertainties of their measurement and applied the same linear fit of this section on data points which are not exactly linear distributed (see Fig. B.4 in appendix B) a comparison between the results is difficult. Moreover, each time the temperature changes the dark current is influenced. Although these factors change the outcome, the values are at least in the same order of magnitude. For further measurements, the CCD camera should be cooled or at least used in a thermally stabilized environment.

3.3.3 Pedestal

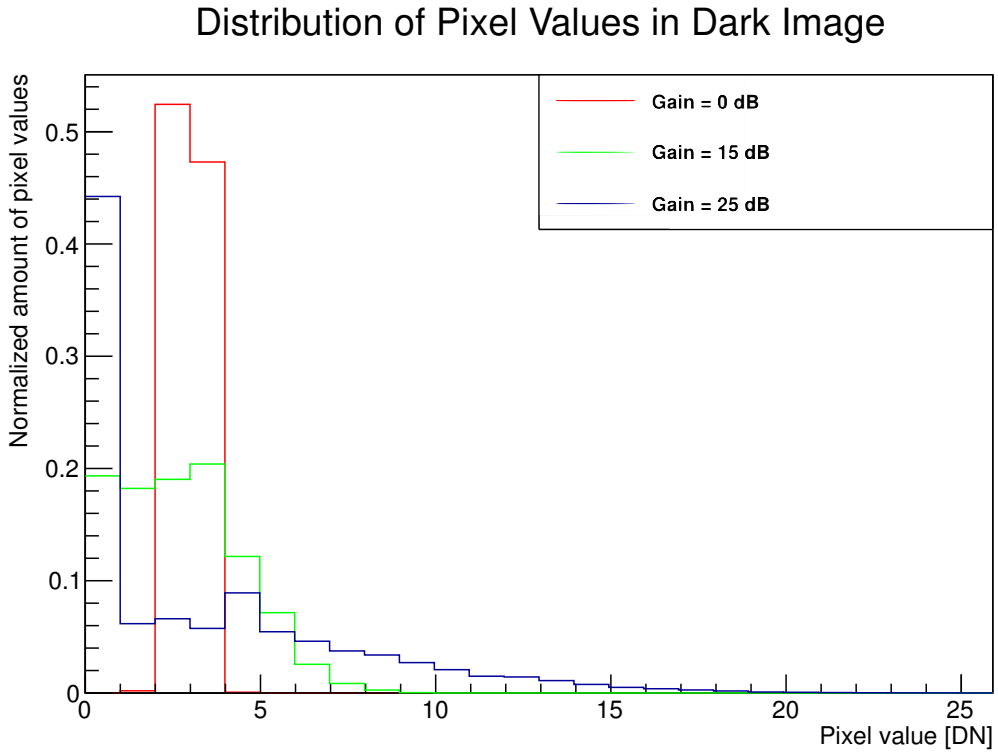

Figure 3.7: The pixel value of a dark frame is set on the ordinate whereas the normalized number of occurence of the pixel value is set on the abscissa. The distribution of pixel values within an image is shifted to lower digital numbers and broadens when the gain is increased.

Each pixel has an electric charge even if the camera is not exposed to light which occurs due to readout noise and pixel artifacts (e.g. pixel which have a much higher/lower dark current as their neighbors). This results in a pedestal in each image. In order to examine the pedestal, the mean pixel value of dark images μ_{dark}, called "mean" for further use, with the smallest exposure time possible t = 10 μs is computed. The image consists of N pixels each with a pixel value y_{ij} which is needed for calculating the mean

$$\mu_{dark} = \frac{1}{N} \sum_{ij} y_{ij}. \tag{3.13}$$

For each gain a dark image was taken and its mean was determined. The mean was plotted against the gain which is shown in Fig. 3.6.
Two different curves determined from two different measurements are shown. The first measurement, illustrated by the black data points, was done at the beginning of the camera operation. The higher the gain is the smaller gets the mean value of the dark image which describes the curve from gain 0 dB to 15 dB. From gain 16 dB upwards the mean increases roughly exponentially. The curve's unusual shape can be explained by the range of the pixel values occuring at zero exposure time. When the gain is increased a broader distribution arises which can be seen in Fig. 3.7. The three histograms of different gain steps show the amount of pixel in an image normalized to one assigned to the pixel value in digital numbers. For gain 0 dB the main digital numbers are concentrated at two and three, whereas for gain 15 dB they are mainly distributed between zero and four which results in a smaller mean value. For gain 25 dB the distribution widens which leads to an arrangement of digital numbers between zero and 15 which explains the higher mean.
The curve with the red data points is the second measurement after the CCD camera had been operating for six hours. For gains between 0 dB and 12 dB the curve resembles the previous measurement but with higher gains it rises more rapidly.
In conclusion the CCD camera should be operated at a gain between 0 dB and 15 dB because the pedestal is small for those amplifications. However, in further measurements gains < 10 dB should be used since the noise will increase rapidly at higher gains even if the pedestal is minimized.

3.4 Optics

Figure 3.8: The zoom objective used for the optical system which records star images. On the left the attached amplifier is visible whereas the right image shows the opening without the first lens which had been removed.

In Sec. 2.3.3 the technique of pointing at the MST prototype was elaborated which includes the requirement of a small field of view. As the technique was developed based on the H.E.S.S. pointing model the optic was chosen according to the H.E.S.S. requirements [DE10]. An objective with a focal length of $f = 800$ mm and an aperture of $f/6.7$ is used. Since optics with such a high focal length are expensive, an objective which is less cost-intensive was investigated and modified [Bae12a]. On this account the "Macro Video Zoom Lens" constructed by the company Optem International was acquired. During this thesis it will be referred as zoom objective. The specifications of the zoom objective are presented in Tab. 3.3.

The zoom objective's focal length ranges from 18 to 108 mm. In order to increase the focal length the first lens for macro close-up adjustments was removed and a teleconverter was mounted. The teleconverter is a secondary lens which is mounted between the camera and a photographic lens and increases the focal length according to the zoom objective's modification and decreases the aperture by a factor of two. For this purpose a "CAT#$29-30-42$ 2xAmplifier" from the company Optem International was chosen. Since the removal of the first lens and addition of the teleconverter change the focal length of the optical system, measurements were undertaken to define the new focal length of the camera lens including the teleconverter which are explained in detail in the next chapter.
The whole optical system is shown in Fig. 3.8 where the teleconverter can be seen as well as the front side of the zoom objective without the first lens.

Optics	**Optem Macro Video Zoom Lens**
Camera Format	2/3" or smaller
Mount	C
Weight	$\approx$ 590g
Length	159mm
Diameter	62mm maximum
Focal Length	$(18-108)$mm
Aperture	f/2.5 - closed
	Optical system with teleconverter without first lens
Focal Length	determined in next section
Aperture	F/5 - closed

Table 3.3: The specifications of the Optem Macro Video Zoom Lens [gra12]. The second part of the table gives some specifications after the first lens was removed and a teleconverter was attached on the objective's ending.

Chapter 4

Optical Measurements

The modification of the previously presented zoom objective lead to optical changes, therefore the following chapter describes the measurement procedure for determining a focal length. The resolution was determine and some star images were taken in order to evaluate the optical system.

4.1 Introduction

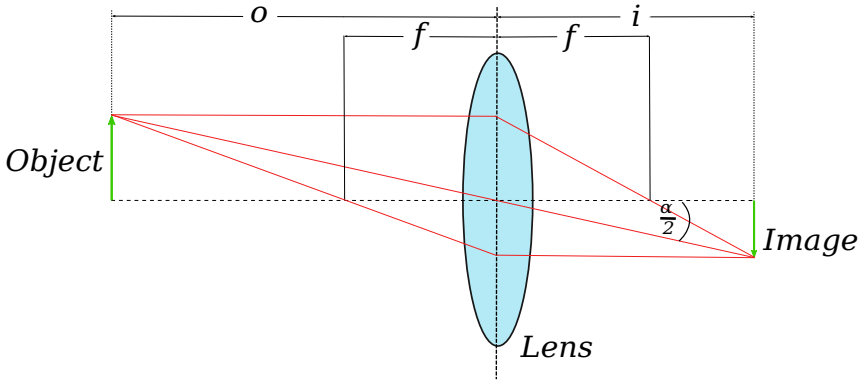

Figure 4.1: A schematic illustration of the dependencies between an object and its image after focusing through a lens. Via the intercept theorem, the thin lens equation and reproduction scale can be derived.

The formation of a sharp image is expressed by the thin lens equation. It describes the connection between the object distance o, image distance i and focal length f. The construction of an image is illustrated in Fig. 4.1. By means of the intercept theorem the thin lens equation

$$\frac{1}{\mathrm{f}} = \frac{1}{\mathrm{o}} + \frac{1}{\mathrm{i}} \tag{4.1}$$

can be derived. Also the reproduction scale R is a useful quantity for describing an optical system. It is the ratio between the image I and the object size O

$$\mathrm{R} = \frac{\mathrm{I}}{\mathrm{O}} \tag{4.2}$$

and gives the lateral amplification of an image. The same amplification is given through the ratio of the image and object distance and can be calculated with the

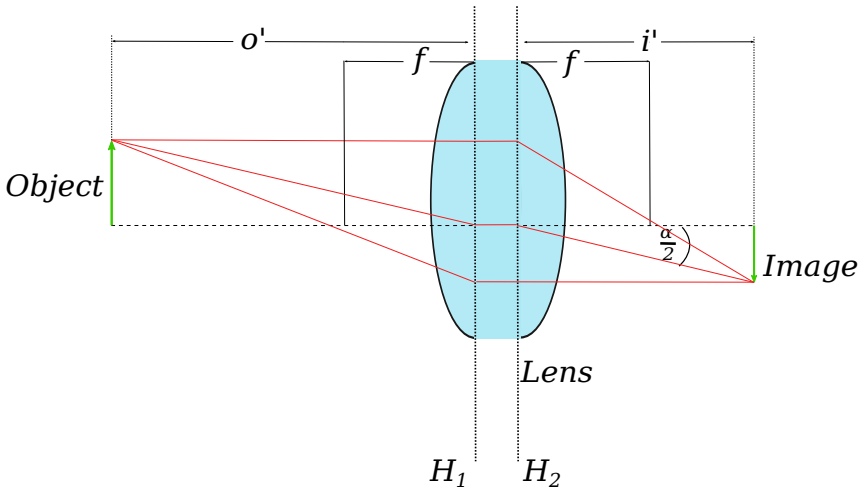

Figure 4.2: A schematic illustration of the dependencies in a thick lens equation. In comparison to the thin lens two main plain distances seperate the object distance from the image distance. The thick lens equation is used for describing the optical path in an objective.

aid of Fig. 4.1 and the intercept theorem.
In general, an objective consists of several lenses whose specifications and alignment are - a priori - not known. This leads to the conclusion, that the thin lens equation is not a good approximation for the zoom objective. The equation for thick lenses is more appropriate. If the lens system in an objective is regarded as a black box with the characteristics of a thick lens, the equations will only differ in the definition of the image and object distance. This is illustrated in Fig. 4.2. When a thick lens is considered, the image and object distances are measured from the first H_1 and second principle plain H_2, which are separated by the thickness of the lens. Consequently the equation is modified to

$$\frac{1}{\mathrm{f}} = \frac{1}{\mathrm{o'}} + \frac{1}{\mathrm{i'}} \quad \text{with} \quad \mathrm{o'} = \mathrm{o} + \mathrm{x}_1 \quad \text{and} \quad \mathrm{i'} = \mathrm{i} + \mathrm{x}_2 \tag{4.3}$$

where x_1 and x_2 give the proper range which changes the image or object distance in the thick lens equation.

4.2 Focal Length Measurements

A test setup was arranged in which the Prosilica CCD camera and the zoom objective have been installed on an optical bench to investigate the focal length. The installation is illustrated in Fig. 4.3. In a short distance o from the camera a LED panel was set up with a cased United States Air Force 1951 (USAF 1951) grid. For longer distances o the USAF 1951 grid was too small, therefore a rope was imaged. The USAF grid consists of lines which are ordered in several groups. Within each group the lines are getting smaller and have different distances to each other which is used to measure the resolution. The resolution behavior and determination is described in the next chapter.
In addition to the lines, squares are arranged on the grid. One of those squares or the rope with an object size O was imaged with the CCD camera and afterwards its size I in the image was determined. Whereas the square on the LED panel/rope

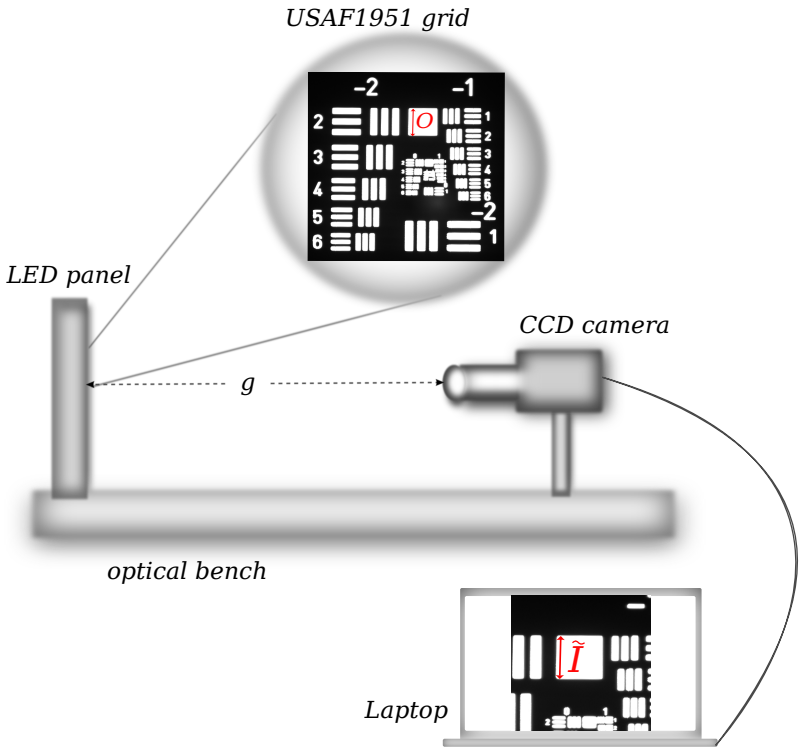

Figure 4.3: The measurement setup for determining the focal length f and the resolution ρ_0 of the zoom objective. The distance, o, between LED panel and CCD camera is varied. Also, for each step the reproduction scale is calculated and the last resolved line group is determined via the USAF1951 grid.

O was measured in meter, the imaged square/rope $\tilde{I}$ was given in pixel. After multiplying the amount of pixels of the square/rope $\tilde{I}$ with the pixel size x_{pixel} of the Prosilica GC 1350 (see Tab. 3.1) the reproduction scale

$$R = \frac{I}{=} = \frac{x_{\text{pixel}} \cdot \tilde{I}}{O} \tag{4.4}$$

was determined via Eq. 4.2.
The distance between the camera and panel was varied which gives a new reproduction scale for each distance. Since the zoom objective has no labeled scale for the focal length only the maximum and minimum adjustment of the focal length was measured. Furthermore, the focal length's minimum adjustment will be referred to as f_{min} and the maximum adjustment used for star imaging as f_{max}. The varied distance against the inverse reproduction scale for f_{min} and f_{max} was plotted. The results are given in the diagrams of Fig. 4.4 and 4.5. All diagrams are analyzed and plotted with the data analysis framework called ROOT [Tea12].
The solid lines within those diagrams represent the fit results. Combining the thick lens equation and Eq. 4.2 of the reproduction scale results in the fit equation

$$\frac{1}{\mathrm{R}} = \frac{\mathrm{o'}}{\mathrm{f}} - 1 \quad \text{with} \quad \mathrm{o'} = \mathrm{o} + \mathrm{h_1} \ . \tag{4.5}$$

The error bars of the data represent systematical uncertainties during the measurement. The distance's uncertainties were estimated from the used measurement device and increased at longer distances because of the absence of a longer device.

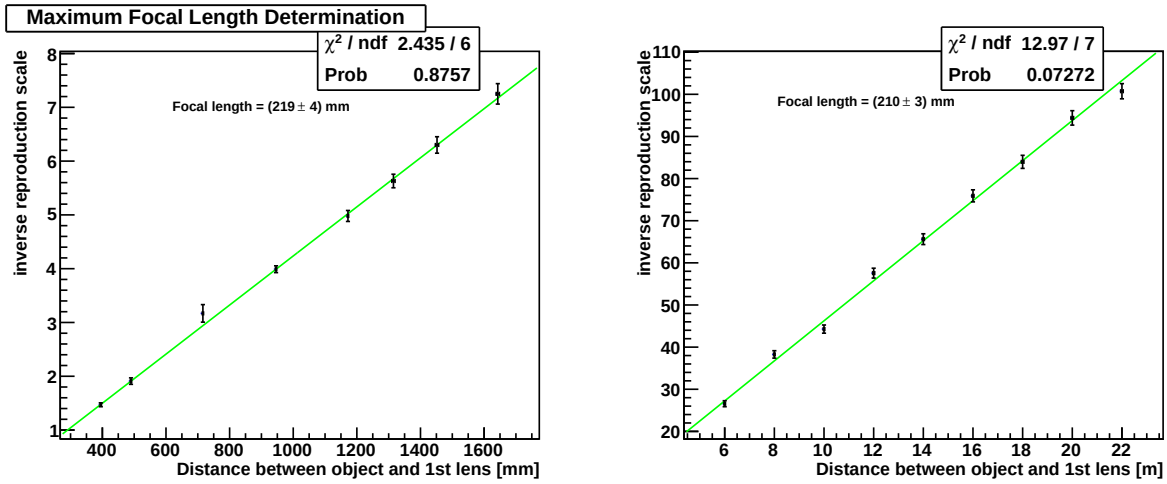

Figure 4.4: The focal length $f_{\max}$ for the zoom objective was determined from two different ranges of object distances (X-axis) depending on the inverse reproduction scale (Y-axis). The fit was executed with two parameters. One is the focal length whose result is shown within the plots.

For the reproduction scale the errors were approximated by the difference between the illuminated square and unexposed grid which stretched over several pixels. Also the grid is not manufactured precisely which is added in the error calculation.
The uncertainties for the object distance o were transfered into the diagrams without change whereas the errors of the inverse reproduction scale 1/R had been calculated via the propagation of uncertainties.

The adjustment $f_{\max}$ is more relevant for the pointing method and since stars are objects at an infinite distance, the focal length associated with larger distances was measured. The distance between the CCD camera and the new object (a rope) was increased and the fraction of the rope visible on the computer screen was determined respectively. The measured data points are displayed in the right plot of Fig. 4.4. The different measurement methods yield the nearly the same result for the focal length.
As the $f_{\min}$ adjustment is needed for another optical task on the prototype, a precise measurement of this observable was also important. The determined data of the $f_{\min}$ adjustment was compared with data points of a fixed 35 mm objective where the measurement was executed similarly. This was done to check the measurement method and to evaluate if the minimum adjustment of the focal length is higher or lower as $f = 35$ mm. The result is shown in the right hand plot of Fig. 4.5. The focal length $f_{\min}$ is in fact higher than the $f = 35$ mm of the fixed focal length objective, which could be determined precisely.

The focal lengths yielded by means of the fit Eq. 4.5 are shown in Tab. 4.1.

	Maximum focal length $f_{\max}$	Minimum focal length $f_{\min}$
1st measurement	$\approx (219 \pm 4)$ mm	$\approx (38 \pm 1)$ mm
2nd measurement	$\approx (210 \pm 3)$ mm	$\approx (40 \pm 2)$ mm
Final results	$\approx (213 \pm 3)$ mm	$\approx (38 \pm 1)$ mm

Table 4.1: The table shows the determined focal length for $f_{\max}$ and $f_{\min}$ adjustment of the zoom objective from Fig. 4.4 and 4.5. The final results are calculated via the weighted mean and its weighted uncertainties of the different measurements.

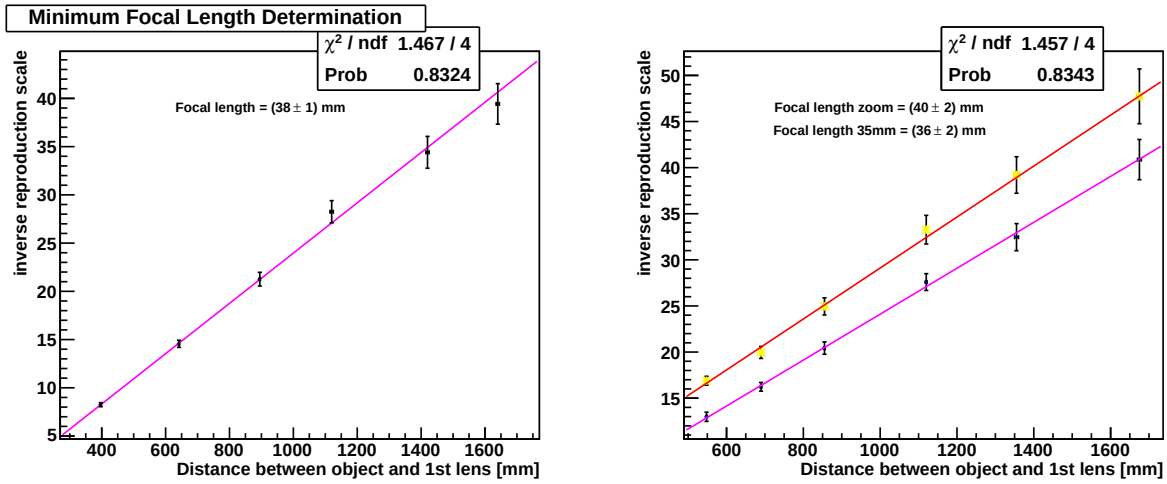

Figure 4.5: The determination of the focal length $f_{\min}$ for the zoom objective with the object's distance on the X-axis and the inverse reproduction scale on the Y-axis with a two parameter fit. The right image compares the fits of a fixed focal length lens of f= 35 mm (pink) with the zoom objective (orange) for a crosscheck of the measurement method.

The final focal length and its error is determined by the weighted mean and its error propagation of the focal length different measurement procedures.
The determined focal length will be used in the following chapters.

4.3 Field of View

Field of View	(1360 × 1024)
18mm	20° x 15°
108mm	3.34° x 2.52°
38mm	$(9.5 \pm 0.2)°$ x $(7.2 \pm 0.2)°$
213mm	$(1.72 \pm 0.02)°$ x $(1.26 \pm 0.02)°$
Resolution	
18mm	53.3" per pixel
108mm	8.9"per pixel
38mm	(25 ± 1)"per pixel
213mm	(4.5 ± 0.2)"per pixel

Table 4.2: The table gives the calculated values for the angle-of-view of the Prosilica CCD chip with dimensions of $(1360 \times 1024) \cdot 4.65$ *μm and for one pixel with the dimension of* 4.64 *μm. The calculations were done for the zoom objective with and without the teleconverter.*

To calculate the field of view and the theoretical resolution per pixel, the schematic illustration of Fig. 4.1 has to be considered. An image is obtained when light is passing through a lens after the distance o and the rays are focused into an image with size I on the CCD chip after a distance i. If the image of the object fills the whole sensor (or one pixel), the angle α between the edges of the sensor will be called angle-of-view.
This angle α can be calculated via the law of tangents. If the camera lens is set to

infinite focus, the distance i between the lens and the image will be set as the focal length f. This leads to an equation for the angle-of-view of

$$\alpha = 2 \cdot \arctan(\frac{I}{2 \cdot f}). \tag{4.6}$$

To obtain the field of view and the theoretical resolution per pixel of the Prosilica CCD together with the zoom objective with or without the optical amplifier, the chip size and pixel size have to be considered respectively. The results can be found in Tab. 4.2.

4.4 Resolution

4.4.1 Theoretic Resolution Limits

The wave nature of light rays implies diffraction by small objects, slits or apertures meaning a point source is not imaged as a point but as a diffraction pattern which consists of radially symmetric maxima and minima called Airy discs. The variation in intensity with angle behind an optical arrangement is given by

$$\mathrm{I}(\theta) = \mathrm{I}_0 \left(\frac{2J_1(|\vec{r}|\, r \sin\theta)}{|\vec{r}|\, r \sin\theta} \right)^2, \tag{4.7}$$

where r is the circular aperture, I_0 the intensity of the center of the Airy disc, $|\vec{r}|$ the absolute value of the wave vector and J_1 the Bessel function of first kind in leading order. The smaller the aperture, the larger is the spot size at a given distance and the greater gets the divergence of the diffracted beam.
The Airy disc has a central spot in the focal plane with a radius to the first minimum given by

$$\rho_0 = 1.22 \cdot \mathrm{k}\lambda \tag{4.8}$$

with k as the f-number (focal length divided by diameter) of the imaging optics and λ the wavelength of the incident light. If two point sources are not very far away from each other, their Airy discs will overlap, they are therefore visible as one source in the image. But if the sources are imaged in the focal plane with a distance equal to or greater than ρ_0 between the centers of the Airy discs, they will be visible as different light sources. Hence, the radius of the first minimum of a diffraction pattern affects the resolution limit of an image.

4.4.2 Resolution Measurements in the Laboratory

Concerning the zoom objective the sources in the focal plane have to be $\rho_0 \approx 3.2\mu$m [1] away from each other to appear as independent light sources. As the pixel size x_{pixel} is bigger than the radius ρ_0, the size of the pixel dictates the theoretical resolution limit.
For the determination of the experimental resolution the USAF1951 grid (Fig. 4.1)

[1] with $\lambda = 520$nm, which has the maximum quantum efficiency in the visible light range

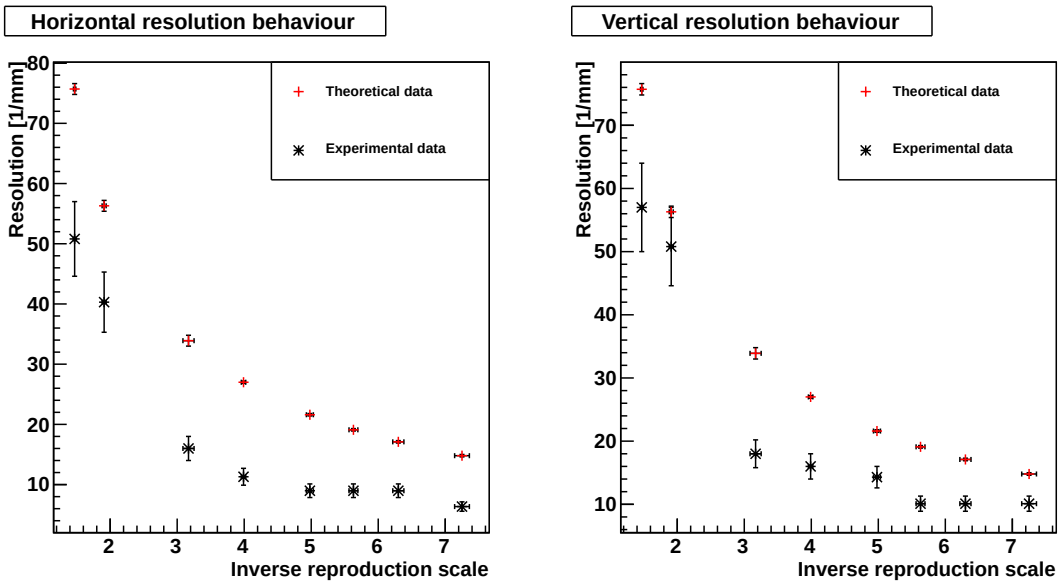

Figure 4.6: The inverse reproduction scale (X-axis) is dependent on the resolution (Y-axis) of the $f_{\max}$ focal length of the zoom objective. The resolution was determined via the USAF1951 grid. The measured data points (black) are significantly away from the theoretical (red) ones probably because image aberrations limit the resolution.

was used. Each of the grid's line groups consist of five line pairs in both vertical and horizontal direction. Images were taken for different reproduction scales and the smallest group of lines that were distinguishable was determined. Via a table (see appendix A) the groups can be assigned to the resolution limit of the optics in line pairs per millimeter (mm^{-1}). The reproduction scale is in the same way ascertained as in the previous section. The horizontal and vertical resolution for both focal length $f_{\min}$ and $f_{\max}$ were determined. The corresponding diagrams are shown in Fig. 4.6 for $f_{\max}$ and in Fig. 4.7 for $f_{\min}$. The red data points resemble the theoretical resolution limit which was multiplied with the reproduction scale, wherein the black points describe the measured data.

The uncertainties for the theoretical data are calculated via error propagation and the error of the reproduction scale. The difference between the smallest line group resolved and the biggest group unresolved is computed for the measurement uncertainties .

The theoretical data are in all figures above the measured data and only a few theoretical data points of $f_{\max}$ range in the area of two times the uncertainties of the measured data. In comparison, for $f_{\min}$ the resolution is a bit better as around three theoretical values lie in the error range of the measured data.

There are multiple reasons for the reduced resolution behavior. Manual focusing and the big resolution difference between two different line groups are possible explanations for the $f_{\min}$ focal length. For $f_{\max}$ these systematical errors are almost not decisive but image aberrations are a possible reason. To examine the zoom objective's usability for the prototype more closely images of stars were taken. These measurements show the degree of aberrations according to a point source and are presented in the next section.

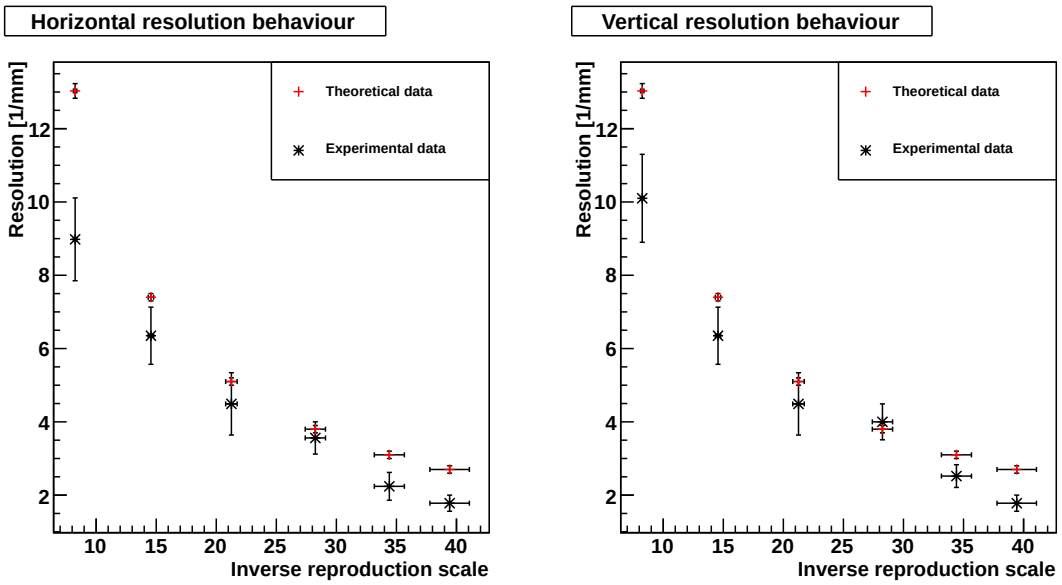

Figure 4.7: The resolution (Y-axis) was determined via a USAF1951 grid while the inverse reproduction scale (X-axis) of the $f_{\min}$ focal length was increased. The theoretical data (red) points are in good agreement with the measured data points (black).

4.4.3 Usability Tests of the Zoom Objective

The usability of the objective for the pointing technique mentioned in Sec. 2.3.3 has to be determined. For this reason images of stars were taken to evaluate their appearance according to the MST requirements.
In order to solve this task the zoom objective and the Prosilica GC 1350 CCD camera was used in Berlin Biesdorf. According to the movement of the Earth the stars change their position on the local night sky therefore a tracking tripod is needed during long exposure times. For the purpose of this thesis a tracking tripod with equatorial mount which has to be adjusted to the right ascension and declination for following the star's motion was borrowed from a local observatory. With the aid of this equipment stars with an apparent magnitude [2] m_a were imaged whose intensity distribution in the image resembles a Gaussian function which is an effect of the atmospheric turbulences [Gyl50]. The atmospheric turbulences are caused by the changes of the refractive index in the different layers of the atmospheric air which corresponds to the change in density. As a result the position of stellar images varies which is expressed by the image coordinates fluctuate statistically around the average. If the image is free of blurring which is induced by optical aberrations or diffraction the average light intensity during an exposure time will be distributed in the focal plane. The amount of light which gets into the elementary area $dxdy$ with coordinates x and y in the intervals $x + dx$ and $y + dy$ is proportional to

$$\mathrm{e}^{-\frac{x^2+y^2}{z^2}}\,\mathrm{dx}\,\mathrm{dy}. \tag{4.9}$$

In this equation z equals the standard error of the Gaussian coordinate distribution multiplied by $\sqrt{2}$ and is called turbulence constant.
A series of Vega images, a star in the constellation Lyra with an apparent magnitude

[2] The apparent magnitude is a measure to describe the brightness of celestial objects as seen by an observer on the Earth. In the calculation the magnitude is adjusted to the value it would have without the atmosphere.

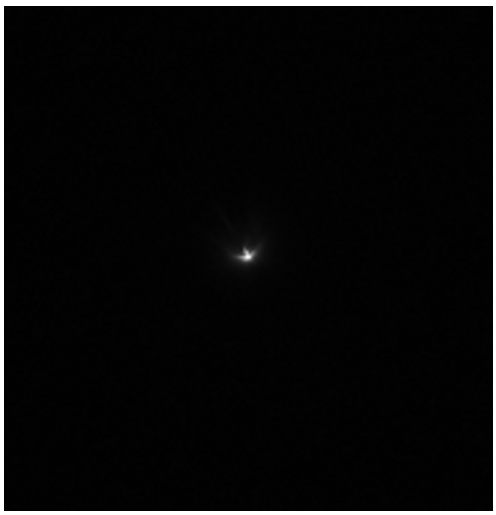

Figure 4.8: A $0.7° \times 0.7°$ *detail of the imaged star Vega which was recorded near the image center with exposure time* $t = 200$ ms *and gain* $g = 0$ dB *in order to reproduce the star's shape using the zoom objective.*

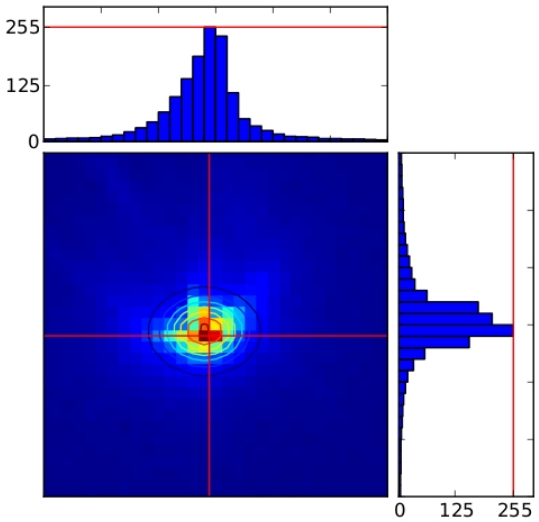

Figure 4.9: The analyzed Vega image in a $0.04° \times 0.04°$ *detail in a 2D plot. The red lines, whose pixel values are shown in the histograms, cross at the star's center of gravity.*

of $m_a = +0.03$, was recorded with different exposure times at a gain of $g = 0$ dB. At an exposure time of $t = 200$ ms Vega's signal went into saturation. An extract of the whole monochromatic image is shown in Fig. 4.8. The star is located near the center of the image which is characterized by a minimum of aberration. Due to the behavior of the atmosphere the imaged star should equal the shape of a Gaussian function in this case a symmetrical circle. The image shows extensions in y-direction as observable in Fig. 4.8. In Fig. 4.9 the star was analyzed and put into a 2D-plot. Within the analysis procedure, the center of gravity was determined. Moreover, projections along the axis which intersect the centre of gravity are drawn on the edges of the 2D-plot.

In the plots the misshaping of the light distribution is clearly visible. Due to the extensions the preferred shape of the light distribution is not achieved and the projections of the x-axis show an unsymmetric function.

During the measurement process the focusing of the Vega image was challenging. This was scarcely noticed during running time because the star was small in comparison to the whole image. In order to examine the focussing an overexposed image was taken. For this purpose Deneb of the constellation Cygnus with a magnitude of $m_a = +1.25$ is used for this measurement. The gain is at a maximum of $g = 25$ dB and an exposure time of $t = 900ms$ is adjusted. The best focusing possible is shown in Fig. 4.10. A diffused circle in direction of one edge away from the center occurs which confirms the previous focusing problem. The extent of the irregularly shaped star image becomes clearer after analyzing the image. The 2D plot in Fig. 4.11 with the projections along the axis intersecting the center of gravity and the 3D histogram shown Fig. 4.12 depict the saturated part of the image which appears as a semi circle shape. A blurred circle arises also radial from the semi circle center and diagonal from the image center. Neither in the projection nor in the 3D histogram the Gaussian function is an appropriate function describing the star's image shape nor another symmetric function.

In Fig. 4.13 the Gaussian function was plotted over the 3D histogram [OG12]. A shift towards the center of the diffused circle is visible which distorts the computation of the center of gravity. In addition the quality of the plot is poor which is based on an $\chi^2/ndf \approx 4.6$.

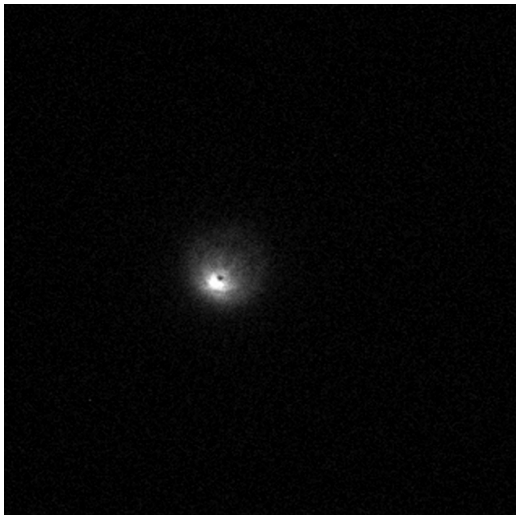

Figure 4.10: A $0.8° \times 0.8°$ *detail of the imaged Deneb star. The star's signal was amplified with a gain of* 25 dB *and exposure time* $t = 900$ ms *to examine sharpening problems.*

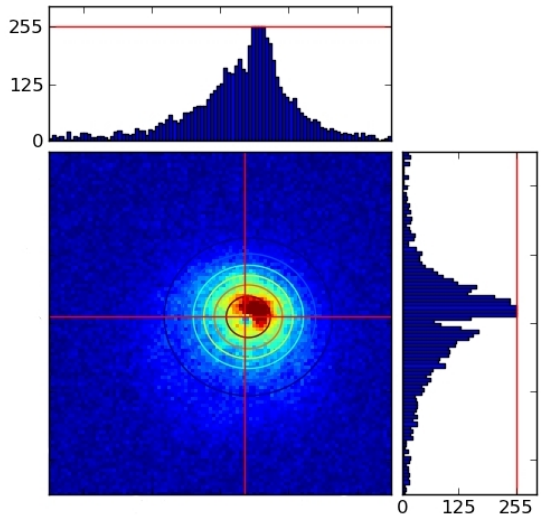

Figure 4.11: The analyzed Deneb image in a $0.11° \times 0.11°$ *detail in a 2D plot. The red lines, whose pixel values are shown in the histograms, cross at the calculated star's center of gravity. The plot illustrates the complex structure of the imaged star.*

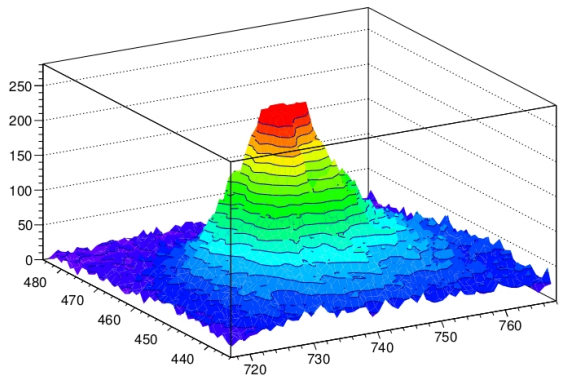

Figure 4.12: The histogram's X- and Y-axis show the assigned pixel number of the imaged Deneb star. Each pixel equals around one millidegree. The pixel values are shown in the histogram's Z-axis. The plot underlines the unsymmetrical behavior due to imaging with the zoom objective.

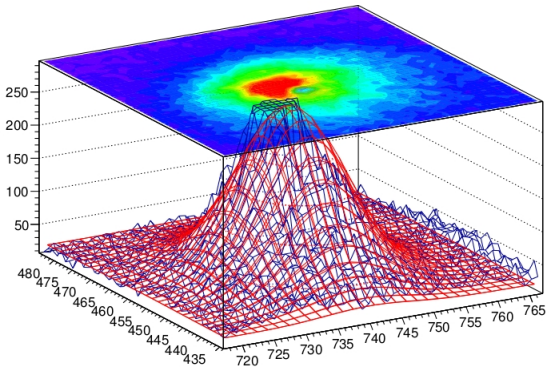

Figure 4.13: The histogram shows the pixel numbers (X- and Y-axis) with its corresponding pixel values (Z-axis) of the imaged Deneb star. A 3D Gaussian function is fitted over the histogram as it resembles the structure of an imaged star the most.

4.4.4 Conclusion

According to section 2.3.3 the determination of the center of gravity of the light distribution on the CCD sensor should be done with high precision. The angular resolution limit can be determined via error propagation of the field of view (Eq. 4.6) and the consideration of a small angle between the real center of gravity and the imaged one. Two main uncertainties affect the star imaging the most. The error $\sigma(\mathrm{f})$ results from the focal length measurement of the zoom objective. The error could be reduced to a minimum with a high precision measurement, e.g. by two well-known stars in the field of view. The other uncertainty $\sigma(\mathrm{I})$ introduced the imaging of the star. The imaging in the CCD camera returns small angle therefore the error of the resolution limit can be approximated by

$$\sigma(\alpha) = \sqrt{(\frac{1}{\mathrm{f}} \cdot \sigma(\mathrm{I}))^2 + (\frac{\mathrm{I}}{\mathrm{f}^2} \cdot \sigma(\mathrm{f}))^2}. \tag{4.10}$$

If it is considered that the light distribution has a Gaussian shape due to the broadening of the atmosphere, the uncertainty will be described as the ratio between the full width at half maximum (FWHM) and the square root of the counts assigned to a digital number caused by the star flux in the image $\sqrt{N}$

$$\sigma(\mathrm{I}) = \frac{\mathrm{FWHM}}{\sqrt{\mathrm{N}}} \approx \frac{2.4 \cdot \sigma^{\mathrm{total}}(\mathrm{f})}{\sqrt{\mathrm{N}}}. \tag{4.11}$$

In case of the Gaussian function the FWHM can be represented by the standard deviation σ. As described in the previous section the image distribution is broadened by different phenomena which convolute with each other. Those are diffraction, atmospheric turbulences and aberrations. They give the uncertainties of the maximum of the light distribution which scales with the focal length

$$\sigma^{\mathrm{total}}(\mathrm{f}) = (\sigma^{\mathrm{atmosphere}} \otimes \sigma^{\mathrm{diffraction}} \otimes \sigma^{\mathrm{aberrations}}) \cdot \mathrm{f}. \tag{4.12}$$

Thus the focal lengths will cancel each other out in Eq. 4.10. Hence the precision is not dependent on the focal length which was assumed by mistake during the development of the pointing method. If it is considered that the manufacturing is very precise the focal length, will even vanish totally from the equation. In this case not the focal length determines the image quality but aberrations, diffraction and the atmospheric turbulences.
Concerning the zoom objective the theoretical resolution limit was not achieved as was shown in Fig. 4.6. At this point it was concluded that aberrations are responsible for the insufficient resolution. This was confirmed by the star images. Their irregularly shaped structure is an indicator for primary aberrations e.g. spherical aberration, coma and astigmatism which mostly are a result of another optical component attached to the objective. Some of them scale with the lens' combination in the zoom objective therefore they have a larger influence on the resolution of the f_{max} focal length which leads to extensive errors. Those aberrations could be reduced by certain software tools in the offline analysis but as the aberrations cannot be determined exactly the software would not correct them.
Another mentionable effect is the high exposure time for bright stars which will result into deformations of the Gaussian function because of local atmospheric turbulences and vibrations according to the eigenfrequency of the prototype telescope.

For example for Vega with an apparent magnitude $m_a = +0.03$ the exposure time is around $t = 200$ms. As there are few stars visible in Berlin which appear brighter than Vega those effects will increase. Even if the telescope's vibrations are considered in the offline analysis the other causes of deformation remain. Apparently the zoom objective does not fit with the pointing method. Consequently, a new optic had to be selected.

Chapter 5

Alternative Optics and Sky CCD Pointing Method

The previous chapter described the inadequate optics regarding to the previous mentioned pointing method. Based on the outcomes, requirements on a new optic could be established which leads to a newly acquired objective. The specifications of the objective provide the possibility to a more precise pointing method which fits better to the night sky of Berlin.

5.1 Alternative Optics

5.1.1 Optical Requirements

Problems according to the zoom objective which caused troubles during measurements and analyzing were discussed in Sec. 4.4.4. Those technical problems imply requirements for new optics which should replace the old one.
The variance of the light distribution widens due to aberrations, atmospheric turbulences and diffraction as described in Eq. 4.12. The atmospheric turbulences can change within milliseconds. This can lead to an increasing variance of the light distribution and to an wider Gaussian function. If the exposure time is decreased, the errors occuring from atmospheric turbulences will be reduced .
This can be achieved by a bigger **aperture** and a smaller f-number, respectively. If the f-number is getting smaller, the same amount of photons hit the CCD chip during a smaller exposure time. Moreover, a smaller f-number reduces the diffraction effects which leads to reduction of the diffraction error. On the other hand the aberrations increase. Therefore a correction of the lens system is preferred. This can be achieved by constructing the objective with **aspherical lenses**.
The optics should also match with the **sensor format** of the CCD camera. As the sensor has a format of 1/2" with a diagonal of 8 mm, objectives which are designed for this sensor size or bigger can be used. If an optical system for a smaller sensor would be used an effect called vignetting will appear. This effect darkens the edges of the image and only a circle within the image is illuminated.
Even if a variety of objectives fits the sensor size of the CCD camera, not every one of them has the same mount as the camera. However, it is possible to match optical systems with a different mechanical mount to a camera via a **mount adapter**. An adapter does not change the image quality because it is only a non-optical camera extension but since it increases the distance between the lens and the sensor the

focal length would be changed. The Prosilica GC 1350 has a C-mount and therefore this extension is needed for every objective mount which is bigger than the C-mount. For the objective two requirements concerning the **focal length** need to be contemplated. At first it is significant to decide on a focal length which is either changeable or static. As the sensor needs much light and the optical aberrations should be minimized, a static focal length is more profitable. With a changeable focal length the light caught by the objective in the minimum focal length adjustment is distributed for a higher focal length to more pixel which results into a darker imaged object. The second point is the preferred high focal length. The best light intensive objective types are telephoto lenses which are mostly high in price.
As light intensive objectives with a focal length f $\geq$ 100 mm are too expensive, an objective with a smaller focal length was chosen. The choice fell on the "Walimex Pro 85 mm" objective.

5.1.2 Walimex Pro Objective

Figure 5.1: The Walimex Pro objective provides a bigger field size with a fixed focal length of f = 85 mm. In the left image the wide opening is presented which is very light intense. On the right the C-mount adapter is visible.

The purchased Walimex Pro has a focal length of f = 85 mm. Even if the focal length is too small according to the requirements, the other conditions fit very well. The aperture has a big opening so that a high number of photons can hit the sensor and aspherical lenses were used for the objective fabrication which minimizes aberrations. All specifications can be found in Tab. 5.1. As the objective is constructed for a Nikon system camera an adapter is needed.
The optics, which are composed of the adapter and the objective, can be seen in Fig. 5.1.

5.1.3 Resolution

The resolution of the Walimex objective had to be determined. Therefore, the setup and procedure of Sec. 4.4 was repeated. The Airy disc radius of the first minimum for the given optics has a value of $\rho_0 \approx 0.9$ μm. This represents the distance in which two points are distinguishable from each other. As the Airy disc radius is

Optics	**Walimex Pro**
Camera Format	36x24mm or smaller
Mount	F
Weight	≈ 480g
Length	72mm
Diameter	78mm maximum
Focal Length	85mm
Aperture	f/1.4 - closed
Other	aspherical glass lenses result into high imaging quality
Adapter	**HAMA camera adapter**
Lenses	none
Connection 1	C-Mount
Connection 2	F-Mount

Table 5.1: The specifications of the Walimex Pro 85mm objective [Med12]. The second part of the table gives the mount information for the non-optical camera adapter.

again smaller than the pixel size of the CCD camera, the pixel ascertains the resolution limit of the Walimex Pro objective.

All the measured data points are displayed in a diagram which can be seen in Fig.

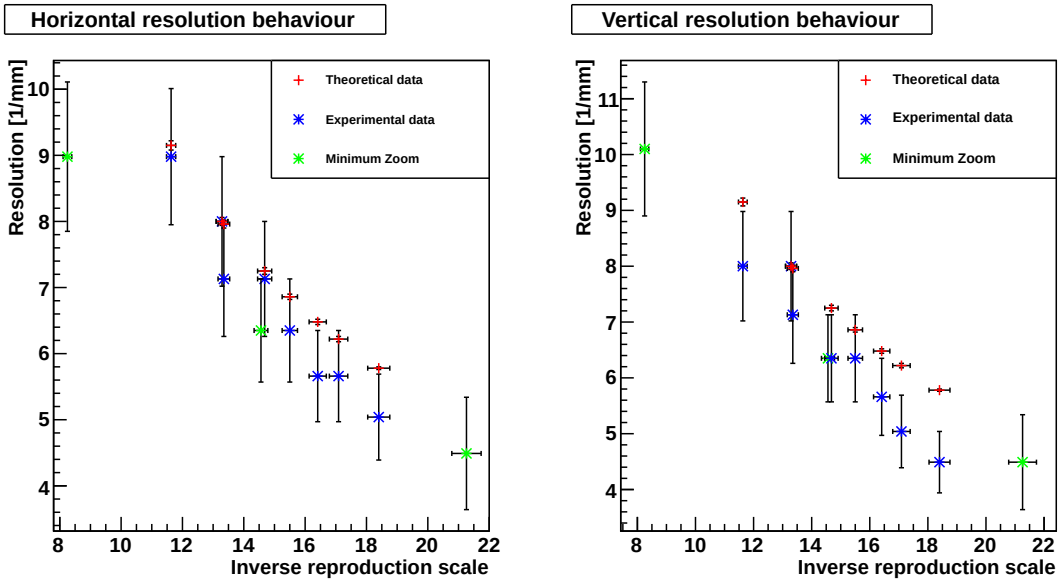

Figure 5.2: The inverse reproduction scale (X-axis) dependency of the Walimex objective's resolution (Y-axis) was measured in the laboratory (blue). The theoretical resolution behavior (red) of the Walimex objective as well as some data points from the $f_{\min}$ zoom objective are inserted (green).

5.2. The figure shows the inverse reproduction scale on the x-axis which depends on the resolution given in line pairs per millimeter mm^{-1}. The black data points represent the measurement whereas the red ones are the theoretical data. The data, diagrammed in green, is the measured resolution data from the f_{min} adjustment of the zoom objective and serves as a comparison between the old and the new optics. As in the previous chapter the measured data lies under the theoretical limit but is still in good agreement since the majority of the theoretical data is located within

the errors of the measured data. In comparison to the zoom objective at f_{min} the Walimex objective has an equivalent resolution. The resolution in horizontal direction is better than the zoom objective's resolution. Moreover, the resolution is better for a higher distance to the object as the resolution data fits well with the theoretical data at lower reproduction scales. However, it was not possible to reach the theoretical resolution data directly as the focusing is done manually and the precision of the grid's increments is the limiting factor.
All in all even if the focal length is higher than the f_{min} adjustment the resolution is comparable suitable. Furthermore, according to the horizontal resolution the Walimex objective's resolution is better than the zoom objective's. This leads to the conclusion that the aberrations are minimized due to the fabrication with aspherical lenses as it is stated in the instruction.
To sum it up the Walimex is more appropriate for taking star images as the resolution behavior for high distances is quite good and that only a small amount of distortions takes part in the image formation.

5.2 New Pointing Method

Due to the reduction of the objective's focal length to gain more light during a smaller exposure time the visual field gets bigger. Additionally, more stars are visible. As described in Sec. 2.3.3 the pointing method works with only one bright star in the image field. With the bigger extract of the sky more stars appear in the image which gives the possibility to use more than one center of gravity for the determination of the field of view center. A new method for handling the amount of center of gravities is needed which possibly increase the precision of the pointing model.

5.2.1 Astrometry

The new objective provides the possibility to observe several stars simultaneously. Moreover, the light collection area is much higher therefore the yield rises within a smaller exposure time. The astrometry method was chosen which uses at least three stars for identifying the location where the telescope is directed. For the purpose of this thesis the general principle of astrometry based on coordinate transformation was calculated. The calculation is outlined in appendix C.
A star with the equatorial coordinates (α, δ) is taken as a reference to represent the coordinates in terms of the pixel coordinates in the image plane. Thus, coordinate transformation lead to a right ascension of

$$\alpha = \alpha_0 + \arctan\left(\frac{-X}{\cos(\delta_0) + Y \cdot \sin(\delta_0)}\right) \tag{5.1}$$

where α_0 represents the right ascension where the optical axis intercept with the sky and X and Y are the pixel coordinates of the star. The declination is described by

$$\delta = \arcsin\left(\frac{\sin(\delta_0) + Y \cdot \cos(\delta_0)}{\sqrt{1 + X^2 + Y^2}}\right). \tag{5.2}$$

After transposing the two equations the coordinates of the star displayed on the image plane can be solely written by spherical coordinates

$$X = -\frac{\cos(\delta)\sin(\alpha-\alpha_0)}{\cos(\delta)\cos(\delta_0)\cos(\alpha-\alpha_0)+\sin(\delta)\sin(\delta_0)} \tag{5.3}$$

and

$$Y = -\frac{\sin(\delta_0)\cos(\delta)\cos(\alpha-\alpha_0)-\sin(\delta)\cos(\delta_0)}{\cos(\delta)\cos(\delta_0)\cos(\alpha-\alpha_0)+\sin(\delta)\sin(\delta_0)}\ . \tag{5.4}$$

While the coordinates (X, Y) are measured the standard coordinates (x,y) are received by dividing by the focal length. Moreover, the measured coordinates are often influenced by systematical errors. The systematical errors are represented by parameters, the plate constants. Each plate constant stands for a different uncertainty e.g. optical aberrations, the rotation of the coordinate axis or the mismatch of the system's origin point with the intersection of the optical axis with the image plane. The correction are taken into account in the general ansatz

$$X = a \cdot x + b \cdot y + c \tag{5.5}$$
$$Y = d \cdot x + e \cdot y + f \tag{5.6}$$

where a, b, c, d, e and f represent the plate constants [MP94].
The plate constants can be calculated via at least three stars since the system of equations is completely determined. If the amount of stars increases the plate constants will be determined more precisely with an accurate statistical analyzing method.
In comparison to the previous pointing method the bigger field of view makes the astrometry method more precise. The accuracy of the Astrometry method is much better as the center of gravity of multiple stars is used for determining the center of the field of view. Moreover, systematical errors of the optical system are taken into account during the measurement, which could not be implemented that easily in the previous method. To sum it up, the Astrometry method tends to be more appropriate with a bigger field of view in comparison to the single star method outlined before therefore, it is chosen for further measurements concerning the prototype.

5.2.2 Astrometry-Software

During this thesis a software was developed in order to find points in a given image with several stars. The resultant software used packages of the programming language Python but the execution time of several minutes was too long. Moreover, it was challenging to match the found points with actual stars therefore a software [Beh12], known as **Astrometry.net**, was used which was recommended by the VERITAS group and several other observatories. The software uses the coordinates of a taken image to transform them into sky coordinates in terms of the world coordinate system. Afterwards the image is tagged with the names of the found astronomical data.
The algorithm of astrometry.net works via defining features within an image. Those features consists of four stars which are adapted to star catalogues such that they can be found in different parts in the sky. For each part of the sky this feature gets an index. If all features in the image are labeled, the indices are compared and the

stars can be identified. For this method the developers of astrometry.net included a new hashing method which searches for possible matches in a fast and efficient way [LHM+10].
Since the possibility exists to use the approximate field size of the CCD camera the identification via astrometry.net takes only several seconds. For the identification of stars two main star catalogues were used by the astrometry.net developer:

- USNO-B, which is an all sky catalogue, provides about 10^9 objects taken from various Schmidt plates during observations of the last 50 years [MLC+07] and
- Tycho-2, which is a reference catalogue with 2.5 million brightest stars in the sky mapped by the ESA Hipparchos satellite [HFM+00].

As the software works fast and stable it was used for this thesis in order to focus more on the pointing technique itself and their technical equipment.

5.3 Further Optical Performance Tests

By means of the astrometry.net software the exact field of view for the Walimex objective can be determined. In the previous chapter the zoom objective has shown an imaged star with an irregular shape. In order to examine the symmetric behavior of the Walimex objective images of a star on different locations on the chip were analyzed with the aid of the Hillas parameter.

5.3.1 Field of View Determination

As the adapter is not accurately fitting to the objective the field of view probably is limited and the light intensity of the point sources is reduced. On this account the difference between the theoretical and experimental field of view has to be determined.
The theoretical field of view is calculated comparable to Eq. 4.6 by means of the new focal length whereas the experimental one is calculated by the astrometry.net software. On several days images with more than three stars were taken. On account of the distance of the stars the field size is determined. A variety of images is analyzed and according to them the mean of the field sizes and its error are computed. The

Field of View	
Theoretical	4.26° x 3.21°
Experimental	$(4.21 \pm 0.01)°$ x $(3.17 \pm 0.01)°$

Table 5.2: The theoretical field of view is determined by the angle of view formula. Mechanical change of the objective decreases the focal length and with it the field size which is experimentally proven by analyzing several star images. However, the change is not dramatic.

results are shown in Tab. 5.2 and they demonstrate a smaller field of view. However, the experimental field of view is only 1.2% smaller than the theoretical therefore the intensity is reduced likewise about 1%.

5.3.2 Symmetry Measurement

If an object moves away from the optical center aberrations will distort the object's shape. A star for example will not appear symmetrical anymore but will have an elliptical shape if it is effected by aberrations. To reduce the aberrations the Walimex objective is equipped with aspherical lenses which eliminate spherical aberrations and additionally decrease others. In order to examine possible distortions away from the optical center a star was recorded on different positions of the CCD chip. Useful parameters, which are typically used by γ-astronomers for the description of elliptical shape of a Cherenkov light distribution in the PMT camera, were proposed by Hillas [Hil85].

Hillas Parameter

The light distribution in a camera detecting Cherenkov light has an elliptical shape comparable to an image of a star effected by optical aberrations in a CCD camera. Consequently, the Hillas parameter are helpful to characterize the star's light intensity distribution. The ellipse shape is characterized by parameters written in terms of zero, second and third order of moments of the light distribution. They correspond to the position, orientation, shape and brightness of an image in the camera. In Fig. 5.3 are shown a few basic Hillas parameter.
Some of them contain information about the direction of a γ-ray shower (e.g. α, ϕ)

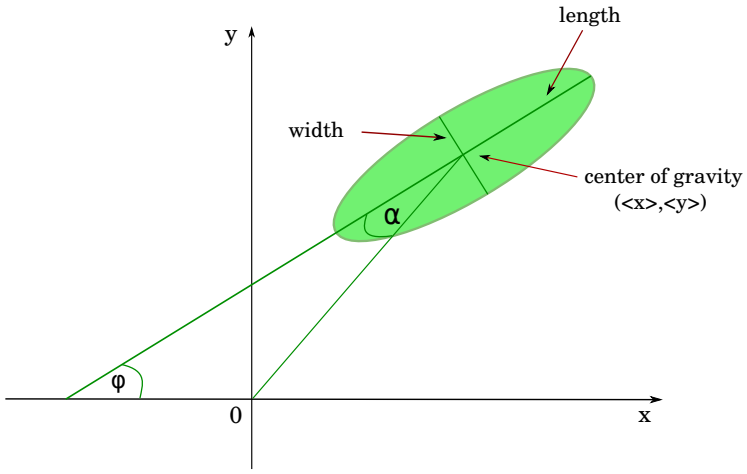

Figure 5.3: The Hillas parameter width, length, <x>, <y>, α and ϕ, are some basic parameters to describe the elliptical shape and direction of origin of a light distribution.

while others contain information about the shower size (e.g. Width, Length). For the purpose of examining the star's shape only the size parameters are of interest. The origin of the coordinate system presented in Fig. 5.3 is placed in the chip's center. Each pixel i has a x- and y-coordinate and a pixel intensity p_i given in digital numbers DN. The light distribution's center <x> and <y> are referred to center of gravity and are calculated by

$$<\mathrm{x}> = \frac{\sum_i p_i x_i}{\sum_i p_i} \qquad <\mathrm{y}> = \frac{\sum_i p_i y_i}{\sum_i p_i}. \tag{5.7}$$

The Hillas parameter width and length, which correspond to the RMS value of the light distribution along the ellipse's major and minor axis, can be derived from second order moments $<\mathrm{x}^2>$, $<\mathrm{y}^2>$ and <xy> of the light distribution . The width

σ_W is connected to the lateral axis and the length σ_L to the longitudinal axis of the star.
The second order moments give the entries of the covariance matrix

$$C = \begin{pmatrix} \sigma_x^2 & \sigma_{xy} \\ \sigma_{xy} & \sigma_y^2 \end{pmatrix} \tag{5.8}$$

given by $\sigma_x^2 = <x^2> - <x>^2$, $\sigma_y^2 = <y^2> - <y>^2$ and $\sigma_{xy} = <xy> - <x><y>$. The quadratic length σ_L^2 and width σ_W^2 are the Eigenvalues of the covariance matrix of the second moments matrix

$$\sigma_W = \sqrt{\frac{1}{2}\mathrm{tr}(C) - \sqrt{\frac{1}{4}\mathrm{tr}(C)^2 - \det(C)}} \tag{5.9}$$

$$\sigma_L = \sqrt{\frac{1}{2}\mathrm{tr}(C) + \sqrt{\frac{1}{4}\mathrm{tr}(C)^2 - \det(C)}} \tag{5.10}$$

Here $\mathrm{tr}(C)$ represents the trace of the matrix and $\det(C)$ the determinant.

Measurement Analysis

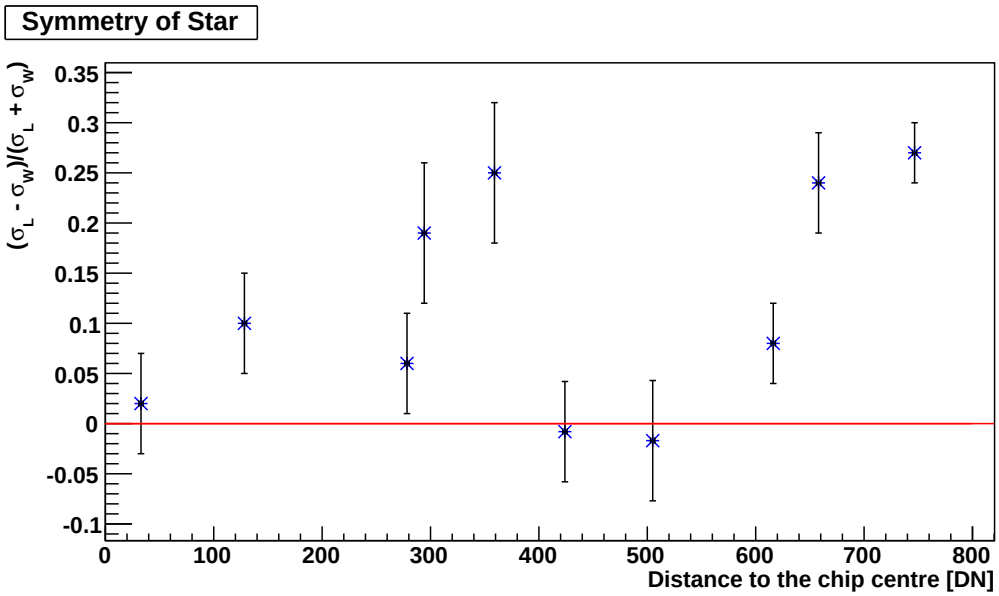

Figure 5.4: The distance to the chip centre according to the coordinates x and y on the sensor is displayed on the abscissa whereas the ordinate shows the symmetry factor based on the Hillas width and length of an imaged star. Underlying this depiction is the assumption that aberrations on a circle with same distance to the center are alike. Away from the chip centre the aberrations are supposed to increase therefore the symmetry value is expected to rise. A clear dependency is not apparent.

A star image located on ten different positions on the CCD camera chip was used to analyze the symmetrical behavior. It is assumed that the aberrations on a circle with the same distance to chip centre are a like and increase with the distance. In the offline analysis the star's coordinates were identified by the astrometry.net software. Afterwards they were verified by SIMBAD, an astronomical database [WOE+00]. With a distance of 0.18" to the star's center of gravity *29 Peg was specified by the

database.
With the implemented Hillas parameter the width σ_W and length σ_L for each star position were determined. For an evaluation of the symmetric behavior a symmetry value

$$S = \frac{\sigma_L - \sigma_W}{\sigma_L + \sigma_W} \tag{5.11}$$

by means of the Hillas parameters were calculated. If the symmetry value equals zero the shape of the star will be symmetric. The more the star shows an asymmetric behavior the symmetry value will strive against one.
The ascertained values depending on the distance from the chip center

$$r = \sqrt{(x^2 + y^2)} \tag{5.12}$$

are inserted into the diagram of Fig. 5.4.
The diagram shows that most data points are greater than zero which results from a greater length than width of the image. Moreover, the values show a high variation due to possible atmospheric disturbance or CCD chip distortion. Consequently, no immediate conclusion can be drawn concerning the reduction or increase of aberrations further away from the optical center. However, the images show good symmetry behavior since all values are smaller than $S = 0.3$.

Concluding from the previous arguments the combination of the instruments and methodology are promising for future measurements. The symmetry behavior and resolution are more than sufficient for a precise identification of the star imaged although more stars are detected in the bigger field of view.

Chapter 6

Star Imaging

After the introduction of the astrometry method and the Walimex objective star images were taken to investigate exposure times for further measurements. Additionally, Berlin's night sky background and the dynamic range were evaluated from the recorded images. For this purpose the following considerations will be based on images of the bright magnitude star Vega. The uncertainties in this section are calculated based on the noise term given in Sec. 3.2 by Eq. 3.4.

6.1 Flux

The incident radiation of a star is described by its flux F which is connected with the stellar magnitude system m by the formalism

$$m_x - m_{x,0} = -2.5\log_{10}(\frac{F_x}{F_{x,0}}). \tag{6.1}$$

Here $F_{x,0}$ represents the flux and $m_{x,0}$ the magnitude of a known reference star in the same band x. Since stars radiate over an extended wavelength region, wide band photometric systems for classifying stars according to their colors were developed. One widely used band system is the UBV system by H. L. Johnson [JMIW66]. Since then the system has been extended to the red with optical IR and near-infrared JHK filters. Fluxes in the Johnson system are normalized to that of Vega, which means that the conversion of Johnson magnitudes to absolute fluxes require the multiplication by the flux of Vega.

According to Bessel [Bes79] the number of photons for Vega striking the top of the atmosphere for different passbands are given in Tab. 6.1. In the table λ represents the wavelength of the passband where the flux is at its maximum.

The given fluxes for different wavelengths were evaluated to determine Vega's spectrum which is illustrated by the blue curve in Fig. 6.1.

6.1.1 Extinction

Since the light of stars traverses the atmosphere to be observed at the Earth's surface, the photons collide with the particles in the atmosphere which leads to absorption or scattering in different directions. Thus, not all photons reach the observer and as a result a smaller flux from the star will be detected compared to on an atmosphere-free planet.

The extinction of light depends on the air mass AM the photons have to pass

Passband	λ[nm]	Flux [$\frac{\text{photons}}{\text{s nm m}^2}$]
U	360	$7.59 \cdot 10^7$
B	440	$1.46 \cdot 10^8$
V	550	$9.71 \cdot 10^7$
R	670	$6.46 \cdot 10^7$
I	870	$3.90 \cdot 10^7$
J	1250	$1.97 \cdot 10^7$
H	1650	$9.6 \cdot 10^6$
K	2200	$4.5 \cdot 10^6$

Table 6.1: The flux maximum for a magnitude zero star at a wavelength λ is given for different Johnson filters.

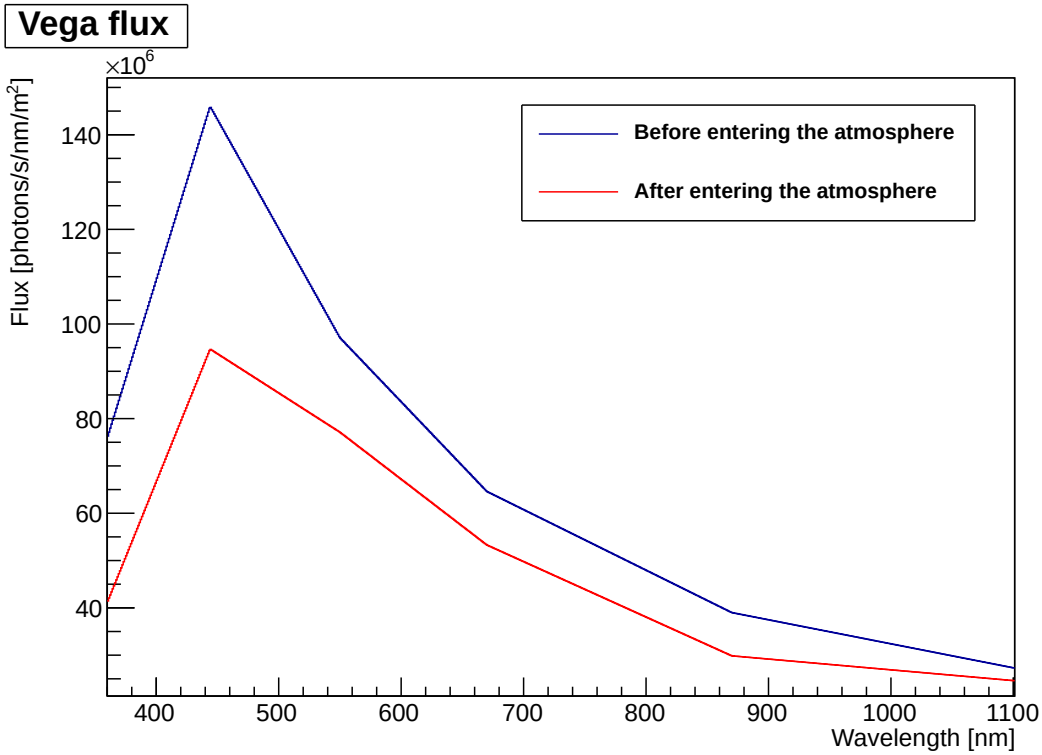

Figure 6.1: The flux (Y-axis) Vega produces at different wavelengths (X-axis) according to Bessel [Bes79]. The two graphs show the spectrum of Vega before the star light enters the atmosphere (blue) and afterwards (red) due to the extinction in the atmosphere.

through which is defined as $AM = 1$ if the radiation enters from the zenith. If the observed star is located away from the zenith the light has to travel through a higher amount of air which is illustrated in Fig. 6.2.

The longer way through the air is calculated

$$AM = \frac{1\ AM}{\cos(z)} \tag{6.2}$$

by means of the angle z which is opened by the perpendicular and the path the light penetrates the atmosphere. Thus, Vega's flux decreases with a greater angle. How bright a star appears in terms of magnitudes on the Earth's surface can be

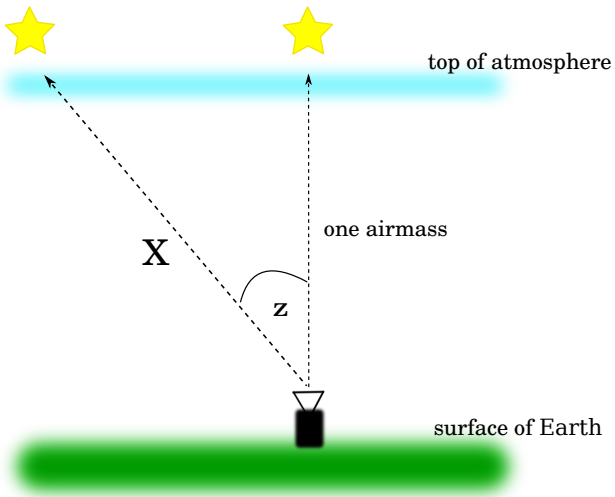

Figure 6.2: One air mass (AM) will be traversed by the star light in the atmosphere if the star is at zenith. The way will get longer if the star does not stand directly at zenith. Via the angle z this longer way can be determined.

expressed by

$$m(AM) = m_0 + \kappa \cdot AM \tag{6.3}$$

which is dependent on the star magnitude outside the atmosphere m_0, the extinction coefficient κ and the air mass AM. The extinction coefficient varies for different wavelengths and properties of the local atmosphere. Their values for the UBVRI filters are given in Tab. 6.2. With the information given in the table and an angle

Passband	**magnitude m_0**	κ **[mag · air mass^{-1}]**
U	0.005	0.6
B	0.03	0.4
V	0.03	0.2
R	0.1	0.1
I	0.2	0.08
J	-0.18	0.08

Table 6.2: The extinction coefficients κ are given for different Johnson passbands and their corresponding magnitude on an atmosphere-free Earth [Har59].

of $z = 26°$ on the day images were taken from Vega, the flux on the Earth surface was computed. The result is given by the red curve in Fig. 6.1 which clearly shows the effect of the atmosphere on the flux.

6.1.2 Signal

Before Vega's flux can produce a signal in the CCD detector the light has to travel through the optical system. Due to the transmission through a glass lens and the reflection on each glass/air boundary light losses occur. The Walimex objective consists of nine glass lenses of which each is provided with an anti-reflective coating. Thus, only 1% of light is lost at each boundary [Rot09]. The transmission within a

lens increases due to the anti-reflective coatings therefore for each lens a light loss of 1% is adopted. Consequently, the original flux is reduced by

$$(1 - 0.01 \cdot 3)^9 \approx 76\% \tag{6.4}$$

as three percent light loss occurs at each lens due to the glass/air boundaries and the transmission within a lens.
In order to determine the signal detected by the CCD camera the reduced flux at different wavelength is folded with the quantum efficiency curve of the Prosilica camera. Additionally, the product of the light collecting area of the Walimex objective

$$A = \pi \cdot \frac{(\frac{f}{1.4})^2}{4} \approx 29 \text{ cm}^2 \tag{6.5}$$

and the flux is computed. The expected Vega flux in the used instrument is shown in Fig. 6.3.

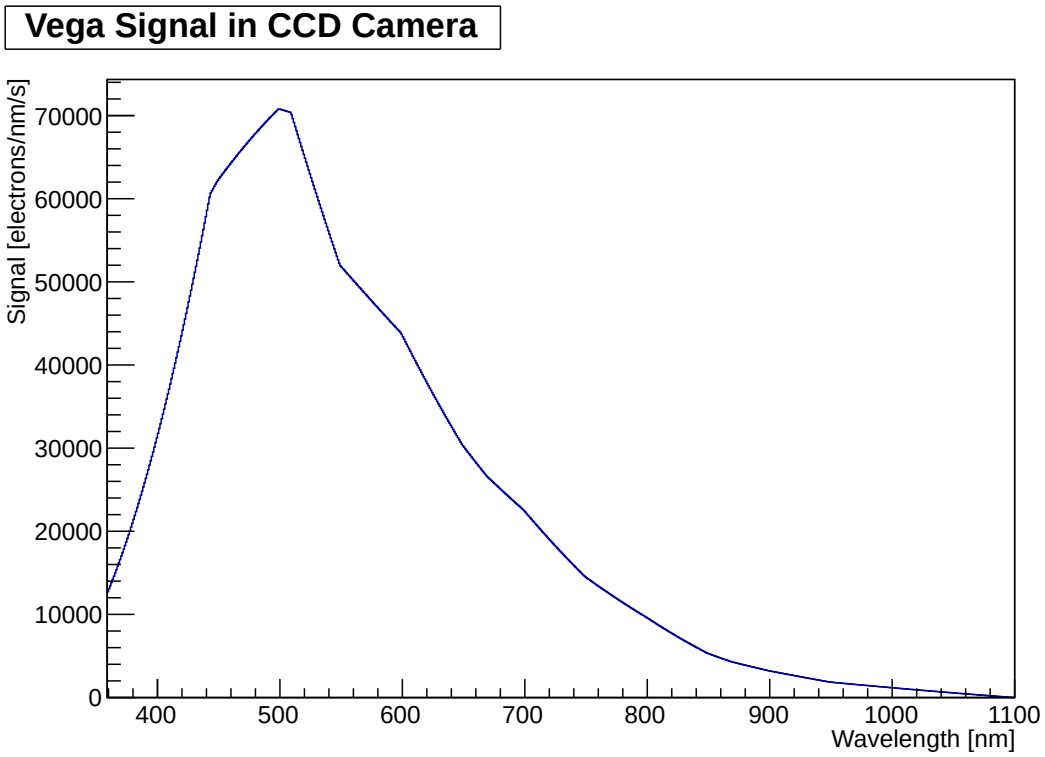

Figure 6.3: The computed signal (Y-axis) Vega produces in the Prosilica camera dependent on the wavelength (X-axis) according to Vega's flux on Earth surface and the quantum efficiency curve of the Prosilica camera.

6.2 Vega Images

Since the theoretic signal of Vega had been computed, a comparison between the measured signal and the theoretical is feasible. For this purpose Vega images were taken during one night without gain and exposure times varying from $t = 9 - 300$ ms. After the investigation of the maximum value in each Vega data the image with an exposure time of $t_{\text{exp}} = 50$ ms was found to be nearly in saturation with

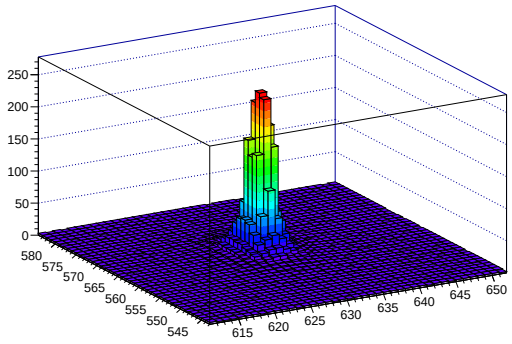

Figure 6.4: The histogram's pixel numbers (X- and Y-axis) with the corresponding intensity (Z-axis) of the imaged star Vega is shown. One pixel equals roughly three millidegree in the sky. The nearly saturated star's signal was obtained with gain $g = 0$ dB and an exposure time of $t = 50$ ms.

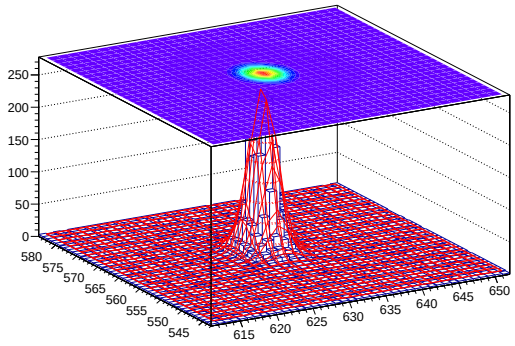

Figure 6.5: A Gaussian fit which was introduced in Sec. 4.4.3 was applied to the histogram shown on the left side. The fit agrees well with the imaged stars of the Walimex objective.

a maximum at $p = 253$ DN. It was chosen for further considerations and analyzed with the same analyzing tools of Sec. 4.4.3. The result is a 3D histogram shown in Fig. 6.4 which is used to determine the amount of digital numbers originating from the star light. Moreover, the Gaussian fit was performed on the histogram in order to quantify the image quality of the Walimex objective in comparison to the Zoom objective.

For the integral of the 3D histogram Vega's total digital signal $I_{\text{star}} = (15000 \pm 275)$ DN within 50 ms is received. By means of the signal which was computed in the previous chapter the amount of electrons per digital number, better known as inverse overall system gain $1/G$, can be determined. Therefore, the total theoretic flux I_{theo} was ascertained by integrating the curve in Fig. 6.3 over all wavelengths. The ratio between them is expected to yield the overall system gain

$$\frac{1}{G} = \frac{I_{\text{theo}} \cdot t_{\text{exp}}}{I_{\text{star}}} \approx (52 \pm 1)\frac{e^-}{\text{DN}}. \tag{6.6}$$

In comparison to the theoretic value of $1/G = 46\ e^-/\text{DN}$ the measured value is a bit higher which results from the difference between the theoretic calculated flux and the real measured flux, since for the light's path to the sensor only rough estimations were established. For example, the extinction coefficient κ for different wavebands was the result of one particular extinction model and will vary with each executed model. Moreover, the assumptions based on the extinction coefficient calculation are different for every observation position. Additionally, the light losses within the optical system are also only approximated. For a correct calculation those should be checked as well as the quantum efficiency data given by the manufacturer. By taking all the approximations into account the result is in good agreement with the theoretic data.

In addition to the flux comparison the fit quality of a Gaussian function on the star data were determined. On the first sight the histogram appears very symmetric and the fit yields a $\chi^2/ndf \approx 0.5$ which shows the improvement of the image quality

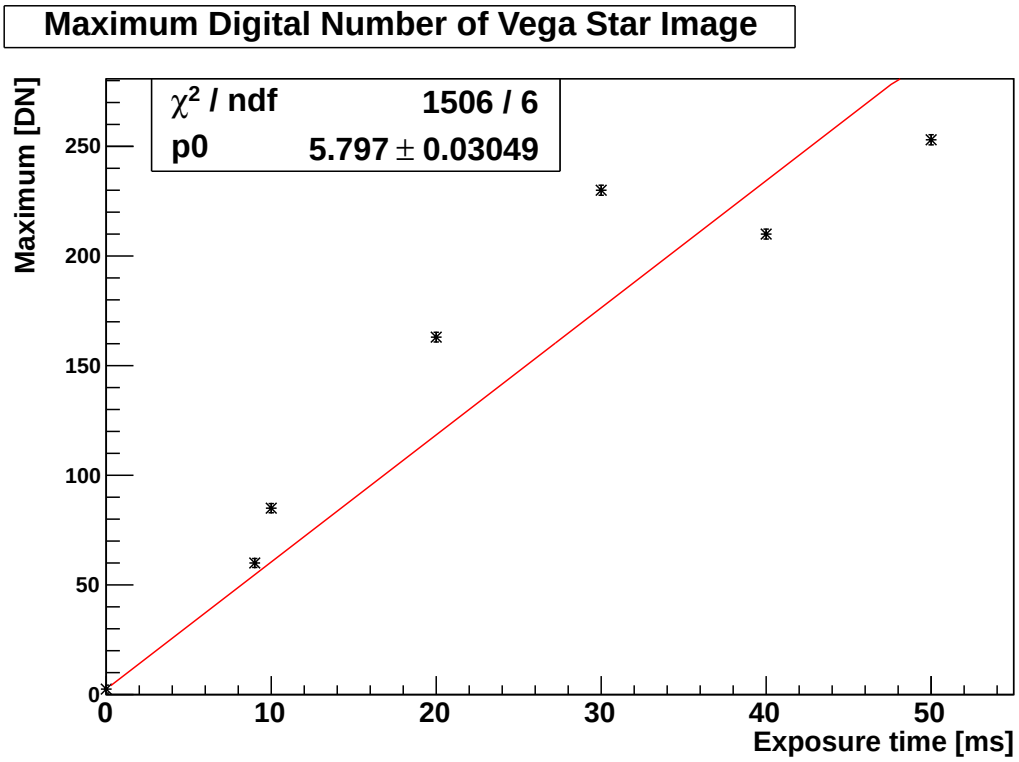

Figure 6.6: The maximum count in Vega images (Y-axis) for different exposure times (X-axis) was determined in order to evaluate when Vega's signal goes into saturation. The data points do not show a linear behavior due to side effects in the atmosphere. The linear fit was applied as it is known that the signal rises linear with the exposure time.

in comparison to the Zoom objective. Possibly, speckles existing from the different movement of atmospheric layers caused by the blowing of the wind blurred the Vega signal and therefore the fit worsened slightly.

6.3 Exposure Time

Compared to the previous basic measurements a more systematic approach was chosen. Instead of varying the exposure time of various bright stars sample shots were taken to derive dependencies between star brightness, exposure time and the collected data. In this process a range of exposure times between the first expected and the saturated signal was an appropriate ansatz for further parameter adjustments. As it was done in the previous sections Vega's signal serves as the reference for the calculation. By means of Eq. 6.1, the exposure times can be calculated by

$$t = \frac{I}{f_{\text{ref}}} \cdot 10^{-\frac{m_{\text{ref}}-m}{2.5}} = t_{\text{ref}} \cdot 10^{-\frac{m_{\text{ref}}-m}{2.5}}. \tag{6.7}$$

Here I represents the amount of counts the star with magnitude m should have within a certain exposure time t whereas f_{ref} characterizes the flux of the reference star with magnitude m_{ref}. Since the reference flux f_{ref} is directly correlated to the number of counts per reference exposure time (I/t_{ref}), the equation for the required exposure time becomes independent of the counts.
Thus, the exposure times for a saturated signal and the first expected signal for Vega

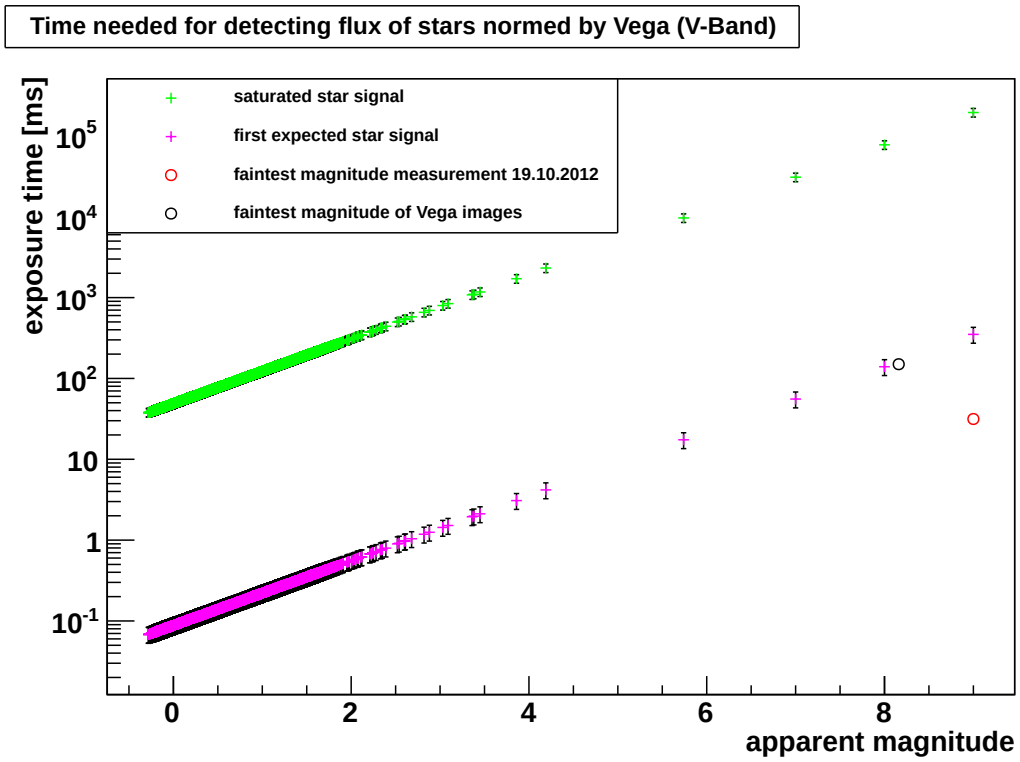

Figure 6.7: The apparent magnitude of a star (X-axis) with expected exposure times (Y-axis) based on measurements of Vega is shown in the logarithmix plot. The magnitudes were taken from the bright star catalogue [HWJ95]. Additionally, the magnitudes $m = 8$ and $m = 9$ are added for comparison between calculated signals (green, magenta) and measurements (black, red).

is required. A saturated Vega signal was yielded at $t = 50$ ms but the exposure time when the first signal is expected has to be determined. It is assumed that it arises slightly above the mean background value which corresponds to the counts of three digital numbers. In order to estimate the corresponding exposure time the maximum digital number in each Vega image below saturation was plotted against their exposure times which is shown in Fig. 6.6. The measurement points do not follow a straight line because atmospheric turbulences and speckles most likely influence the light detected by the CCD camera. Even so, a linear regression is applied on the data since it is known that the maximum digital number increases during longer exposition. However, this results in a bigger systematic error. The outcome exposure time for the signal of three digital numbers was received by using the fits slope and intercept. The yielded value is $t = (0.09 \pm 0.02)$ ms. Since the measurement data points do not follow a straight line, the saturated signal was determined by the linear regression in order to evaluate the uncertainty of its exposure time. This leads to an exposure time of $t = (50 \pm 6)$ ms for the saturated signal.

Due to Eq. 6.7 and the ascertained exposure values the diagram in Fig. 6.7 was plotted and shows the predicted exposure times for different stars. The star magnitudes were taken from the bright star catalogue [HWJ95] to ensure the apparent star magnitudes which are visible each night in Berlin. Additionally, two measurement points (magnitudes $m = 8$ and $m = 9$) were plotted in the diagram for comparing the calculated exposure times with the real measurement data. The black point indicates the faintest magnitude which could be investigated by the astrometry software

in the saturated Vega images. In comparison, the red point shows another measurement day on which the constellation Swan was imaged and the values for its faintest detected star were plotted.
The Vega measurement, which was performed on the same day as the images used for the calculation, agrees well with the computed first expected signal. In contrast, the Swan data does not match the prediction. A much smaller exposure time was used as supposed by the Vega calculation to image a faint magnitude star. This results possibly from a better seeing on the measurement day or a possible light pollution due to a very bright star like Vega in the field of view.
To sum it up, the prediction of exposure times based on Vega is satisfying as measurements of the same day match well with the calculation. This can be used as a basis for adjustement of the parameters for imaging other stars or under different conditions (e.g. weather).

6.4 Night Sky Brightness

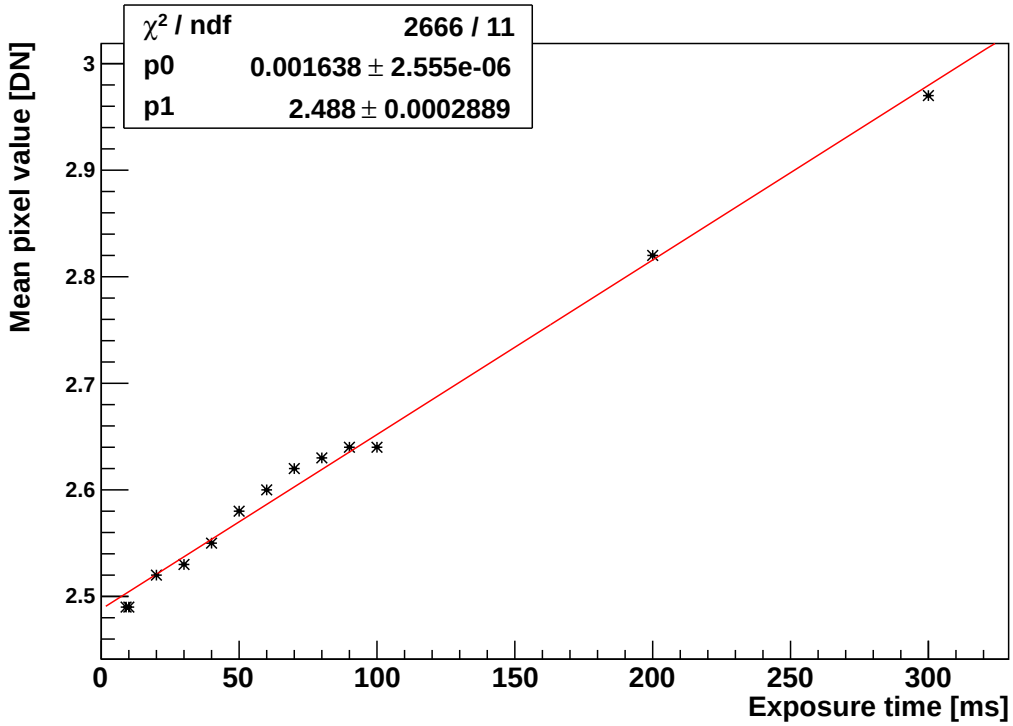

Figure 6.8: The mean pixel value (Y-axis) in Vega images increases with higher exposure time (X-axis). The intercept of the fit gives the electronic pedestal in the images. The mean pixel value provides the basis to evaluate the night sky brightness in Berlin.

The term "night sky brightness" (NSB) corresponds to the remaining light that is present in the night sky during dark, moonless nights. In the visible light range the NSB is mainly contributed by air glow, direct and scattered starlight and zodiacal light [HRW+11]. Sice cities produce a high amount of light pollution, the NSB is often dominated by artificial light sources. This implies a constant level of background on each pixel in the recorded image. The CCD camera's sensitivity can be effected by the fluctuations in the NSB and thus limits the ability for detecting fainter stars.

Therefore, the NSB in Berlin Biesdorf, which resembles the NSB of Berlin Adlershof, is examined in order to evaluate its noise for further measurements.
For this purpose the mean value μ for the different Vega images were determined and depending on their exposure times inserted into a diagram which is shown in Fig. 6.8. The intercept p_1 of the applied linear regression gives information about the electronic pedestal for this particular measurement in the images and will be used for further considerations.
Due to the formalism of Eq. 6.1 the surface brightness in terms of mag/arcsec^2 is calculated by

$$S = m_0 - 2.5\log(\frac{A_{\text{back}}}{A_{\text{star}}}). \tag{6.8}$$

Here A_{back} represents the background counts in one pixel of the optical system and A_{star} the counts of Vega in the image. By using the star Vega as a reference, the NSB is assumed to have the same spectrum as Vega. Additionally the star's light absorption in the atmosphere resembles the NSB absorption. For the background counts of one pixel the difference between the mean value μ and the electronic pedestal p_1 was calculated. If this value is divided by the squared pixel size of the optical system in the sky, here $p = 11$", the value A_{back} will be yielded. As a start the counts of Vega A_{star} have to be released from the pedestal. For this purpose for each Vega image whose star signal does not go into saturation, the mean star counts μ_{star} were computed which results from the counts of the star flux for its corresponding area. This value is subtracted by the pedestal p_1 and afterwards multiplied by the circle area the star covers.
For all the images mentioned before the surface brightness was computed. The results are illustrated in Tab. 6.3. In the table the surface brightness is assigned to two uncertainties. The first one describes the statistical and the second the systematical errors. The computed surface brightness tends to increase with a higher exposure time as more light is collected by the sensor. This was expected due to a higher mean background level with higher exposure times.

The Defense Metereological Satellite Program (DMSP) of the US Air Force has

Exposure Time [ms]	**Surface Brightness [mag/arcsec^2]**
9	$(20.6 \pm 0.1 \pm 0.5)$
10	$(20.6 \pm 0.1 \pm 0.5)$
20	$(18.1 \pm 0.1 \pm 0.5)$
30	$(17.9 \pm 0.1 \pm 0.5)$
40	$(17.9 \pm 0.1 \pm 0.5)$
50	$(17.5 \pm 0.1 \pm 0.5)$

Table 6.3: The computed surface brightness from Vega images taken with different exposure times. The night sky brightness increases with higher exposure times as more light (artificial and natural) shadows the actual star signal.

measured the upward light flux emitted by sources since 1998 [CFE02]. According to the light flux the effects on the night sky were computed by modeling the light propagation in the atmosphere. Consequently, a map for the total night sky brightness in Europe in the visible light regime was established which can be seen in Fig. 6.9. Berlin is shown in the center of Europe and varies from a dark red to a dark yellow

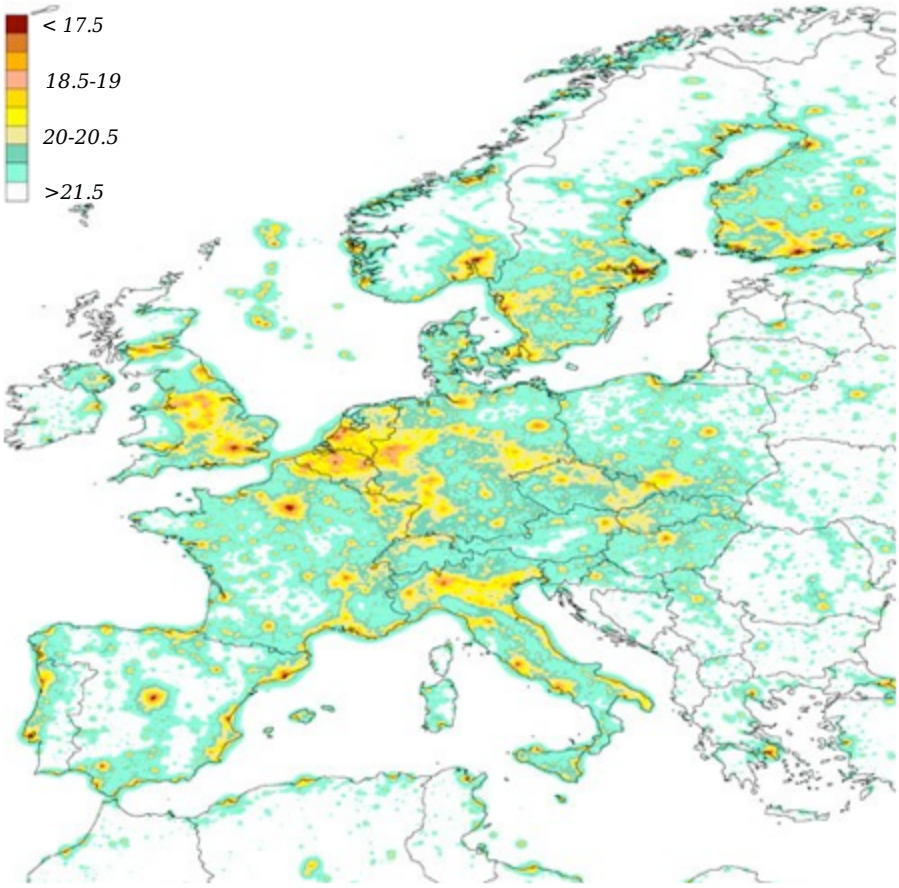

Figure 6.9: The map [CFE02] shows the night sky brightness in Europe which is illustrated by different colors. The scale on the left side shows the surface brightness for each color in terms of mag/arcsec^2. *Especially for densly populated areas the night sky brightness is very high which is indicated by a dark red color.*

color. Thus, the total NSB in Berlin is expected to vary from $17.5 - 19.5 \frac{mag}{arcsec^2}$.
In conclusion the NSB for Berlin was determined with the instruments given and matches accurately with satellite modeled data even using the assumption of similarities of the NSB spectrum with the characteristics of Vega's spectrum. Moreover, the CCD camera has the ability to detect small fractures of light in other wavelength areas whereas the map only shows the total sky brightness in the visible light range. The difference was taken into account for the calculation of the systematic uncertainties.

6.4.1 Dynamic Range

The dynamic range of a CCD camera gives the difference between the largest and smallest possible values and therefore the possibility to differentiate between the brightness levels. Typically, the dynamic range is determined by

$$D(\text{dB}) = 20 \cdot \log(\frac{\text{Full Well Capacity}}{\text{Read Noise}}) \approx 54\text{dB}. \tag{6.9}$$

This is nearly the same dynamic range the manufacturer provided (see appendix B). Since the NSB and the electronic pedestal adds also noise to the image the effective dynamic range changes to $D(\text{dB}) \approx 40\text{dB}$ with the mean background value determined previously.

The higher the exposure time the higher the NSB and therefore the differentiation of the brightness levels gets more difficult. This should not effect the astrometry.net software but should be investigated in more detail for the other tasks at the prototype.

Chapter 7

Planned Activities

In the previous chapters the CCD camera and its optics were characterized in order to evaluate their uncertainties for an exact post pointing calibration procedure. During the measurement process other tests to specify the optical system were developed but have not yet been carried out. In this concluding chapter some of them will be illustrated to point out future work within the topic. Furthermore, proposals for a user-optimized pointing method are described. At the end, the usability of the CCD camera for the CTA experiment is evaluated based on a comparison between the cameras of other IACT experiments.

7.1 Additional Measurements

7.1.1 Chip Deformation

If the operating temperature of the CCD camera rises, not only thermal noise and the corresponding dark current will effect the image quality but also the CCD chip can be deformed [vE13]. This will lead to a distortion of an imaged point source and higher uncertainties in the center of gravity determination.
Usually, CCD chips are used at temperatures down to several degrees Celsius below zero which is achieved by a Peltier element, a thermoelectric cooling device. If the purchase of a Peltier element is needed for the Prosilica cameras on the prototype, will be investigated. Therefore, the camera that is imaging a LED, will be equipped with a thermal sensor to monitor the temperature. Each time the temperature changes an image will be recorded. In order to examine an effect at higher temperatures the CCD camera will be installed in the climate chamber at DESY where temperatures up to 40° C can be simulated.
Due to the comparison of the imaged LEDs the deformation will be visible.

7.1.2 Use of Gain

As mentioned before, the gain amplifies the whole signal in a CCD camera. This allows imaging with lower exposure times or for imaging stars it is possible that a greater number of stars can be detected at the same exposure time. This has been already investigated while taking images of the constellation Swan. In this particular night the number of detected stars for an exposure time $t = 900$ ms rises from 14 at gain $g = 0$ dB to 26 at gain $g = 4$ dB. Since the star images were taken after several minutes, clouds or atmospheric turbulences could change the

imaging conditions. For this purpose, artificial light sources can be imaged on great distances with changing gain to check whether the gain will be useful during image taking. However, it should be considered that the noise is also amplified by the gain, therefore only small amplifications should be used where the noise will not dominate the image.

7.1.3 Measurement of Optical Aberrations

During this thesis the quality of the optical system was characterized based on star images. The measurements were sufficient to reveal optical problems with the Zoom objective. In comparison, the Walimex objective improved the task of the field of view identification nevertheless the image quality suffers from optical aberrations. In order to improve the method all the more, the aberrations should be evaluated in the laboratory.
The investigation can be accomplished by imaging a particular pattern whose characteristics are well known. Afterwards the image and the pattern can be compared by an algorithm developed by the Open Source Computer Vision library (OpenCV) [Ope08]. Among many algorithms one specific can be used to compute the intrinsic and extrinsic camera parameters. The model used in the algorithm is based on the pinhole camera model where a point with coordinates (X, Y, Z) is projected into the image plane expressed by the coordinates (u, v) in pixels. The transformation is formulated by

$$\begin{pmatrix} u \\ v \end{pmatrix} = A \cdot (R|\vec{t}) \cdot \begin{pmatrix} X \\ Y \\ Z \\ 1 \end{pmatrix} = \begin{pmatrix} f_x & 0 & c_x \\ 0 & f_y & c_y \\ 0 & 0 & 1 \end{pmatrix} \cdot \begin{pmatrix} r_{11} & r_{12} & r_{13} & t_1 \\ r_{21} & r_{22} & r_{23} & t_2 \\ r_{31} & r_{32} & r_{33} & t_3 \end{pmatrix} \cdot \begin{pmatrix} X \\ Y \\ Z \\ 1 \end{pmatrix} \tag{7.1}$$

where A represents the camera matrix with f_x and f_y as the focal length of the camera in pixel units. In addition c_x and c_y express the principal points which are usually located at the image center. The matrix $(R|t)$ describes the camera motion around a static scene or vice versa wherein each moment in space can be expressed by the rotation and the translation. The rotation is accomplished by multiplying with the rotation matrix R and the translation by addition with the translation vector $\vec{t}$, hence the 3D point (X, Y, Z) is extended to a 4D vector.
The same formalism is equivalent to

$$\begin{pmatrix} x \\ y \\ z \end{pmatrix} = R \begin{pmatrix} X \\ Y \\ Z \end{pmatrix} + \vec{t} \tag{7.2}$$

which is normalized by $z \neq 0$. This results in the expression of the image plane coordinates as

$$u = f_x \cdot x' + c_x \quad \text{with} x' = \frac{x}{z} \tag{7.3}$$

$$v = f_y \cdot y' + c_y \quad \text{with} y' = \frac{y}{z}, \tag{7.4}$$

which describes (f_x, f_y) and (c_x, c_y) by pixel coordinates.
Real lenses usually have some distortions, mostly radial and slight tangential, there-

fore the coordinates (x', y') are expressed by

$$\begin{pmatrix} x' \\ y' \end{pmatrix} = \frac{1 + k_1 \cdot r^2 + k_2 \cdot r^4 + k_3 \cdot r^6}{1 + k_4 \cdot r^2 + k_5 \cdot r^4 + k_6 \cdot r^6} \cdot \frac{1}{z} \begin{pmatrix} x \\ y \end{pmatrix} + \begin{pmatrix} 2 \cdot p_1 \cdot \frac{x \cdot y}{z} + p_2(r^3 + 2 \cdot (\frac{x}{z})^2) \\ p_1(r^2 + 2 \cdot (\frac{y}{z})^2) + 2 \cdot p_2 \frac{x \cdot y}{z} \end{pmatrix}$$

$$\text{with} \quad r^2 = (\frac{x}{z})^2 + (\frac{y}{z})^2.$$

The coefficients k_1 to k_6 as well as p_1 and p_2 are the algorithm's output parameters which characterize the radial (k_i) and tangential (p_i) distortions of the optic by means of the imaged pattern [odt13]. Additionally these parameters can be used to improve the quality of taken images therefore the tests should be done with all optical systems which will be used on the prototype.

7.2 Adaption of the Method

During the measurements for this thesis it was noticed that changes during the image taking procedure should be taken into account. For the first tests the results were sufficient but in the future the following remarks can improve the precision of the optical measurements.

12 Bit Images

Since the sensor of the Prosilica camera supports 12 Bit image saving the shots should be taken in this format. The used Video Client did not support image saving in 12 Bit therefore images had not been saved with such high digitization during the thesis. A new image saving and display program with a possibility of 12 Bit digitization will be used at the prototype.
The imaging will benefit from several advantages, e.g. the differentiation between 2^{12} brightness levels can improve the dynamic range as the read noise or pedestal is better distinguishable from the actual signal. Moreover, for the other optical tasks a higher digitization leads to a simpler determination between an artificial and natural light source.

Dark Frames

During the measurement artifacts, occurring from the CCD sensor or the objective, appear on the images. The artifacts especially dust and hot pixels, which are pixels with much higher dark current than their neighbors, can lead to confusion during the analysis procedure. Therefore before any measurement will be accomplished, dark frames should be taken to erase these artifacts before the images are analyzed.

Exposure Time

At the beginning of the thesis it was assumed that the exposure time would be changed till the brightest star in the field of view is nearly at saturation. Since the astrometry method was investigated, the saturation of stars has not been problematic, therefore the exposure time will be fixed to a constant number of stars in the field of view. According to the calculation based on Vega, between $t = 500$ ms and $t = 1$ s enough stars will be visible in the field of view. Tests showed that the exposure time range is sufficient for sky areas with comparably bright stars (apparent

magnitudes $m_a = 0 - 4$) and comparably dim stars ($m_a = 4 - 9$).

The quality of the images and the use of the astrometry method will improve significantly with the additional measurements and adaption during the imaging proceeding.

7.3 Evaluation of the Optical System's Usability at the CTA Project

7.3.1 Optical System's Comparison

In order to evaluate if the the CCD camera is a suitable device for the CTA project, the Prosilica camera used for the MST prototype is compared to the other CCD cameras at the three current major IACTs. For this purpose the specifications for the sky CCD cameras of each experiment were investigated. Finding information concerning the cameras at MAGIC were challenging, consequently only material about the LID CCD is represented [Kel11]. However, this camera has the demanding task to image the Cherenkov camera with the PSF and several LEDs as well as some stars which resembles the task of the H.E.S.S. LID CCD. The specification of the different CCD cameras are shown in Tab. 7.1.
Most similarities with the used MST prototype camera offers the VERITAS CCD camera [wik12a] since they are developed by the same manufacturerand use sensors from Sony. In contrast the cameras of H.E.S.S. and MAGIC use KODAK KAF sensors. All experiments use a higher digitization which leads to a high dynamic range. The highest dynamic range is provided by the MAGIC CCD camera which is necessary to distinguish between natural and artificial sources , a feature that is also used in the H.E.S.S. LID CCD camera. The biggest difference between the cameras and the MST camera is the full well capacity. Due to their large pixel size the capacity of holding electrons in one pixel. Especially for the detection of stars this is an important feature since the star's location can be determined more precisely. In addition, the effect of holding electrons in its relative pixel can be supported by a blooming suppression feature which transports the excessive charge.
The sensor's quantum efficiency curves are shown in Fig. 7.1. Only the QE curve of the MST prototype sensor shows a maximum while the other are characterized by a QE which is is above 30% for the whole range of the visible spectrum. Moreover, their maximum sensitivities are nearly twice as high as for the MST prototype sensor which leads to lower exposure times as more photons will be transmitted into electrons. Concerning star imaging a higher sensitivity can result in a greater detected number of stars in the field of view during exposure. However, there is an advantage from the low sensitivity in the infrared regions which usually changes the location of the center of the observed star. Since the number of detected photons, which is converted into charge, is so small no filters are needed.
The only characteristic which is comparable to the other Cherenkov experiments is the light collection. However, it only depends on the used optics. The Walimex objective provides a high light collection area which is nearly the same for the other experiments except for the H.E.S.S. sky CCD according to a different star imaging method.
Based on the comparison between the CCD cameras used at currently operating

IACTs and the MST prototype, the conclusion of using the MST prototype camera for the CTA project is straightforward.

7.3.2 Conclusion

According to the results of this thesis, the Prosilica GC 1350 works adequate for imaging stars in Berlin. Moreover, the operating tests for the prototype will not last as long as for IACT experiments thus the CCD's aging effects, e.g. an increasing number of hot pixels, will possibly not interfere with the tests. However, an improvement of image quality will be achieved for the sky CCD if a camera with higher full well capacity, dynamic range and QE is chosen, since the ability of detecting stars and locating their centers is increased by these features.
Even if the Prosilica GC 1350 is sufficient as sky CCD camera, problems can arise for other optical measurements. The test plan schedules the observation of the PSF and the LEDs on the Cherenkov dummy camera at day time which has not been tested so far. Due to the low dynamic range the differentiation between natural and artificial light sources could be challenging. Moreover, the low QE will lead to exposure times which will exceed the eigenfrequenzy of the telescope while it is moving. This results into blurring of the imaged point sources whose location will be determined laboriously.
In conclusion, the Prosilica 1350 GC CCD camera is adequate for the optical observation task on the MST prototype but for the task of PSF measurement during day time, the features of the camera could be insufficient which should be investigated in more detail. For the CTA project it is recommended to use a sky CCD which has at least a higher full well capacity and a PSF measurement CCD camera whose features are significantly better than those of the chosen MST prototype CCD camera. In comparison the optics could be a proper candidate for the CTA sky CCD as it agrees satisfactory with the other's light collection area. Possibly, the optics will be evaluated in more detail if the proposed measurements, mentioned before, are accomplished.

Properties	MST Prototype	H.E.S.S. (LID)	H.E.S.S. (Sky)	MAGIC (LID)	VERITAS (Sky)	
Camera	Prosilica GC 1350	Apogee Ap2EP	Apogee A1E	SBIG	Prosilica EC 1380	
Sensor	Sony ICX 205	KODAK KAF 1600	KODAK KAF 400E	KODAK KAF 1001E	Sony ICX 285 AL	
Chip size	1360x1024	1536x1024	768x512	1024x1024	1360x1024	
Pixel size (μm^2)	4.65x4.65	9x9	9x9	24x24	6.45x6.45	
Digitization (Bit)	12	16	14	16	12	
Full well depth (e^-)	11 000	100 000	80 000	150 000	18 000	
Lenses (mm)	85	135	800	180	75	
Focal Number	F/1.4	F/2.0	F/6.7	F/2.8	F/1.4	
Light Collection Area	29 cm^2	36 cm^2	112 cm^2	32 cm^2	23 cm^2	
Dynamic range (dB)	56	76	75	79-89	$\approx$ 55-73	
Resolution (arcsec)	11.14/pix	13.75/pix	2.32/pix	27.50/pix	17.74/pix	

Table 1: *The comparison between the CCD cameras of three major cherenkov telescope experiments and the MST prototype.*

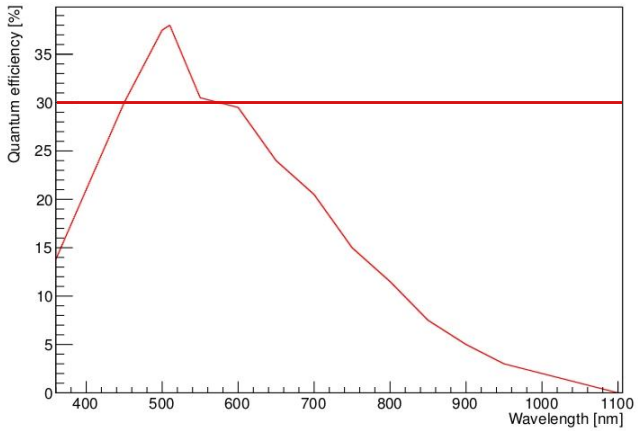

(a) *Sony ICX 205 (MST)*

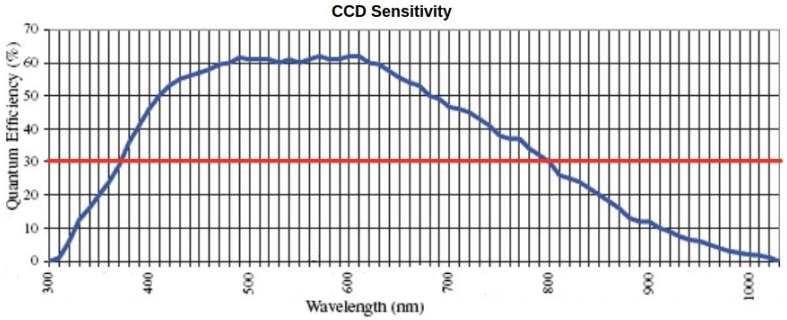

(b) *Sony ICX 285(VERITAS)*

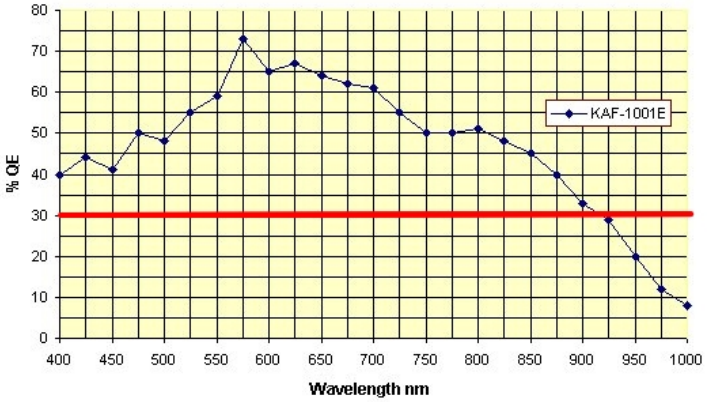

(c) *KODAK KAF 1001E (MAGIC-LID)*

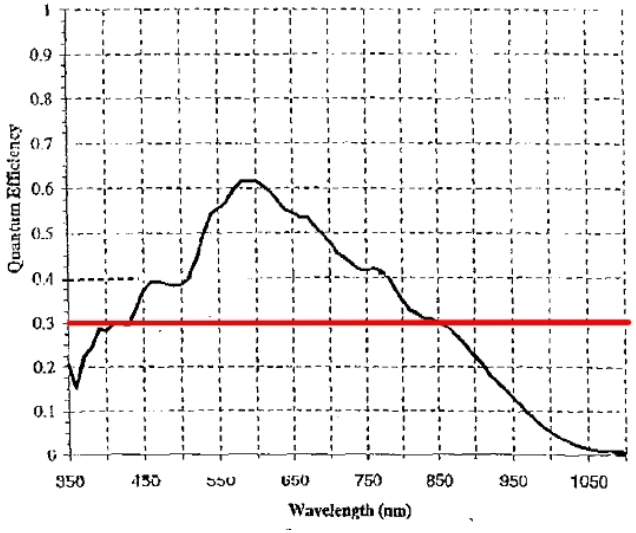

(d) *KODAK KAF 400E (H.E.S.S.)*

Figure 1: *The sensitivity curve of different sensors are shown. The X-axis gives the wavelength and the Y-axis the quantum efficiency.*

Chapter 8

Summary and Outlook

In this work preparations for a precise measurement of the pointing of a telescope prototype whose results will support the future development of the Cherenkov Telescope Array (CTA) project were carried out. For this purpose, the optical equipment and method for orientation in the sky were investigated.
The optical equipment consists of a Prosillica GC 1350 CCD camera and an exchangeable objective. The characteristics have been studied of which great attention was paid to the examination of noise, dark current and a pedestal within dark frames. The results agreed satisfactorily with the information provided by the manufacturer and demonstrated that for further measurements a relatively small gain should be used.
For the used zoom objective the focal length had to be determined initially since mechanical changes according to a teleconverter and a removed lens changed the objective's original focal length. Moreover, resolution measurements in the laboratory demonstrated a large discrepancy between the theoretical and the measured resolution behavior for the maximum focal length adjustment $f_{\max}$ which was supposed to be used at the prototype. The degree of the discrepancy became apparent after analyzing images of stars. The signal of the stars exhibited misshapenings in the image, resulting from the a sharpening problem of the optic. The zoom objective should provide a precise measurement of the center of gravity of a well known star which gives information about the detail of the imaged sky but the star images could not meet the requirements. For this purpose, considerations for a more suitable objective were taken into account which led to the purchase of the Walimex objective. The Walimex objective differs from the previous optics in a bigger aperture and, in comparison to the zoom objective's $f_{\max}$ adjustment, a smaller focal length. The resolution is even better or comparable to the $f_{\min}$ zoom objective's adjustment which agreed well with the theoretical resolution limit.
As the smaller focal length provided a larger field of view than the $f_{\max}$ adjustment of the zoom objective, a greater number of stars can be detected. In the single star method only one well known bright star's center of gravity is involved in the telescope's pointing measurement. Since the bright stars are limited in Berlin, a variety of detected stars provided the basis for a more flexible method, the astrometry method. With astrometry the stars within an image can be determined exactly by using at least three stars. The astrometry.net software supported the astrometry tests which demonstrated satisfying results. The imaged sky field of view could be determined rapidly and the star's center of gravities were identified precisely as the uncertainties typically have not exceeded one arcsecond.

Based on images of the star Vega taken with the Walimex objective, possible exposure times for stars with a different magnitude could be calculated. The calculated signals agree well with the measurements from the same day but differ with measurements taken on different days due to atmospherical turbulences, high atmospherical clouds and others change within days. Nevertheless, the computed values can simplify future measurements a lot. Furthermore, via the Vega images the night sky brightness in Berlin was determined, the results were even consistent with a satellite experiment.
However, more tests are currently under development to improve firstly the method procedure in the future and secondly the image quality due to a characterization of deformations according to the optics and the CCD chip.
Even if the optical system delivered proper results in comparison to sky CCD cameras used at other Cherenkov telescopes, the Prosilica GC 1350 camera would not be the best choice for the future CTA project. Due to a low full well capacity, imaging problems can easily occur which would significantly influence the precision. All in all, the measurements provided reasonable results with the used equipment and present a solid basis for future experiments.

Appendix A

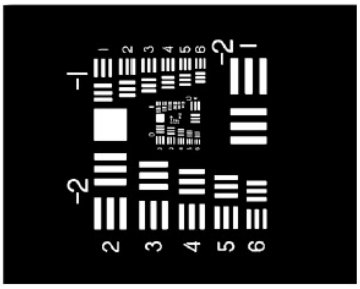

Gittertestplatten

- Zur schnellen und wirtschaftlichen Optikprüfung
- Zur Prüfung von Objektiven und fotografischen Schichten
- Objekte verschiedener Ortsfrequenzen
- Positive und negative Variante

- Zehn Gittergruppen bestehend aus je sechs Gitterpaaren
- Plattengröße: 101,6 x 82,6 x 2 mm

Auflösungstabelle für Gittertestplatten

Gitter-paar	Gruppe -2 L	Gruppe -2 S	Gruppe -1 L	Gruppe -1 S	Gruppe 0 L	Gruppe 0 S	Gruppe 1 L	Gruppe 1 S	Gruppe 2 L	Gruppe 2 S
1	0.25	2000	0.50	1000	1.00	500	2.00	250	4.00	125
2	0.28	1758	0.56	890	1.12	445	2.24	223	4.49	112
3	0.31	1590	0.63	790	1.26	395	2.52	198	5.04	99
4	0.35	1410	0.71	710	1.41	355	2.83	178	5.66	89
5	0.40	1260	0.79	630	1.59	315	3.17	158	6.35	79
6	0.44	1220	0.89	560	1.78	280	3.56	140	7.13	70

Gitter-paar	Gruppe 3 L	Gruppe 3 S	Gruppe 4 L	Gruppe 4 S	Gruppe 5 L	Gruppe 5 S	Gruppe 6 L	Gruppe 6 S	Gruppe 7 L	Gruppe 7 S
1	8.00	63	16.0	32	32.0	16	64.0	8	128	4
2	8.96	56	18.0	28	35.9	14	71.8	7	144	3.5
3	10.1	50	20.2	25	40.3	12	80.6	6.2	161	3.1
4	11.3	44	22.6	22	45.3	11	90.5	5.5	181	2.8
5	12.7	40	25.4	20	50.8	10	102	5	203	2.5
6	14.3	35	28.5	18	57.0	9	114	4.4	228	2.2

L = Anzahl der Linienpaare pro mm
S = Strich- bzw. Lückenbreite in µm

Gittertestplatten

Typ	Teilung	Grund	Order-No	Preis in Euro
Gittertestplatte, positiv	lichtundurchlässig	tranparent	G39 1200 000	890,00
Gittertestplatte, negativ	transparent	lichtundurchlässig	G39 1201 000	890,00

Figure A.1: The USAF 1951 grid for resolution limit measurement. It is imaged by the optical system and the smallest line group that were distinguishable from each other can be determined. By means of the table, the line group's label gives the resolution limit of the optical system.

Appendix B

PROSILICA

EMVA 1288 Standard Specification Sheet

Camera Information	
Vendor Name	Prosilica Inc.
Camera Name	GC1350
UID	100563
Serial Number	02-2130A-06219
Part Number	2130
Part Version	65
Interface ID	2
Interface Type	Gigabit Ethernet
Frame Resolution	1360x1024
Sensor Name	SONY ICX205
Sensor Type	Mono16
Pixel Bit Depth	12
Sensor Diagonal (mm)	7.9162
Pixel Dimensions (µm)	4.65x4.65
Number of Taps	1
Dark Current Compensation	Yes

Test Settings	
ROI	
x_start	630
y_start	462
x_length	100
y_length	100
Other	
Acquisition Mode	Freerun
Gain	0
Exposure Range (µs)	100 - 30000
Number of Data Points	30
Binning X	1
Binning Y	1
Housing Temperature (°C)	

Test Settings (Continued)	
Filter Wavelength (nm)	Light Intensity (W/m²)
546	1.4141E-02

Figure B.1: The specification sheet for the Prosilica camera provided by the manufactuer with additional information. Moreover, the test settings for a measurement task are listed. Possibly, during the measurement a laser was used as light source.

PROSILICA

Measurement Data (λ=546nm)									
Image #	T_{exp} (s)	$\mu_{y,dark}$ (DN)	$\sigma^2_{y,dark}$ (DN)	μ_y (DN)	σ^2_y (DN)	μ_p (Photons)	$\mu_y - \mu_{y,dark}$ (DN)	$\sigma^2_y - \sigma^2_{y,dark}$ (DN)	$SNR_y(\mu_p)$
1	0.000100	15.414	26.741	30.458	30.787	83.935	15.043	4.046	2.711180128
2	0.001131	15.413	26.764	182.846	93.316	949.331	167.434	66.552	17.33263724
3	0.002162	15.337	28.006	332.355	146.872	1814.728	317.018	118.866	26.15852213
4	0.003193	15.434	26.989	483.945	180.586	2680.124	468.511	153.597	34.86400613
5	0.004224	15.236	26.964	633.900	259.974	3545.521	618.664	233.009	38.36983459
6	0.005255	15.318	26.938	786.125	269.004	4410.917	770.807	242.066	46.99654352
7	0.006286	15.430	28.211	935.317	324.779	5276.314	919.886	296.569	51.04343348
8	0.007317	15.403	27.321	1083.301	379.253	6141.710	1067.898	351.932	54.83596338
9	0.008348	15.228	27.024	1231.726	458.778	7007.107	1216.497	431.754	56.7949972
10	0.009379	15.432	27.829	1379.320	478.876	7872.503	1363.889	451.047	62.32572067
11	0.010410	15.322	27.761	1523.347	466.986	8737.900	1508.025	439.225	69.7841131
12	0.011441	15.262	28.072	1666.521	570.741	9603.296	1651.259	542.669	69.11872161
13	0.012472	15.528	26.891	1806.997	500.047	10468.693	1791.469	473.156	80.11317159
14	0.013503	15.222	28.303	1944.490	551.583	11334.089	1929.268	523.280	82.14614056
15	0.014534	15.570	28.093	2079.499	570.615	12199.486	2063.929	542.522	86.40187923
16	0.015566	15.576	27.578	2217.754	643.908	13064.883	2202.179	616.330	86.78420555
17	0.016597	15.398	28.401	2350.762	664.784	13930.279	2335.364	636.382	90.5762774
18	0.017628	15.398	28.747	2483.629	686.025	14795.676	2468.231	657.277	94.23582655
19	0.018659	15.484	27.453	2614.124	722.034	15661.072	2598.640	694.581	96.70908622
20	0.019690	15.445	26.635	2748.201	797.880	16526.469	2732.756	771.245	96.7457639
21	0.020721	15.468	27.356	2876.644	747.324	17391.865	2861.176	719.968	104.6622247
22	0.021752	15.314	28.013	3005.610	773.078	18257.262	2990.296	745.066	107.5480105
23	0.022783	15.390	27.504	3131.653	839.941	19122.658	3116.264	812.436	107.5251084
24	0.023814	15.551	28.422	3261.167	828.611	19988.055	3245.616	800.189	112.7513839
25	0.024845	15.888	28.047	3383.382	829.414	20853.451	3367.495	801.367	116.9287531
26	0.025876	16.089	28.072	3507.153	823.370	21718.848	3491.064	795.299	121.663478
27	0.026907	16.301	28.691	3626.536	772.220	22584.244	3610.236	743.529	129.9167123
28	0.027938	16.393	28.154	3745.558	882.553	23449.641	3729.166	854.399	125.5281946
29	0.028969	15.838	28.015	3861.724	749.574	24315.037	3845.886	721.559	140.4717856

PROSILICA

Measurement Data									
Image #	T_{exp} (s)	$\mu_{y,dark}$ (DN)	$\sigma^2_{y,dark}$ (DN)	μ_y (DN)	σ^2_y (DN)	μ_p (Photons)	$\mu_y - \mu_{y,dark}$ (DN)	$\sigma^2_y - \sigma^2_{y,dark}$ (DN)	$SNR_y(\mu_p)$
30	0.030000	15.913	27.525	3971.839	639.534	25180.434	3955.926	612.008	156.428692

Figure B.2: The measurement data for a 12 bit recording are shown. For each image the exposure time T_{exp}, different means μ and standard deviations σ^2 were computed in order to determine the camera's characteristics.

PROSILICA

Model Parameters (λ=546nm)			
Parameter	**Symbol**	**Units**	**Value**
Inverse of Overall System Gain	1/K	e-/DN	3.5252
Total Quantum Efficiency	$\eta(\lambda)$	%	58.6643
Dark Current	N_d	e- / s	408.3124
Dark Noise for Exposure Time Zero	σ_{d0}	e-	18.3817
Full Well Capacity	$\mu_{e,sat}$	e-	11736.5720
Absolute Sensitivity Threshold	$\mu_{p,min}(\lambda)$	p~	31.3338
Dynamic Range	$DYN_{in} = DYN_{out}$	1	638.4914
Signal to Noise Ratio	SNR	dB	56.1031
Signal to Noise Ratio at Saturation	$SNR_y(\mu_{p,sat})$	1	115.7992
Standard Deviation of Spatial Gain Noise	S_g	%	
Standard Deviation of Spatial Offset Noise	σ_o	e-	
$PRNU_{1288}$		%	
$DSNU_{1288}$		e-	

Figure B.3: The table shows the result of the measurements by the manufacturer. Each parameter was determined by different graphs by means of the measurement data given in the table above.

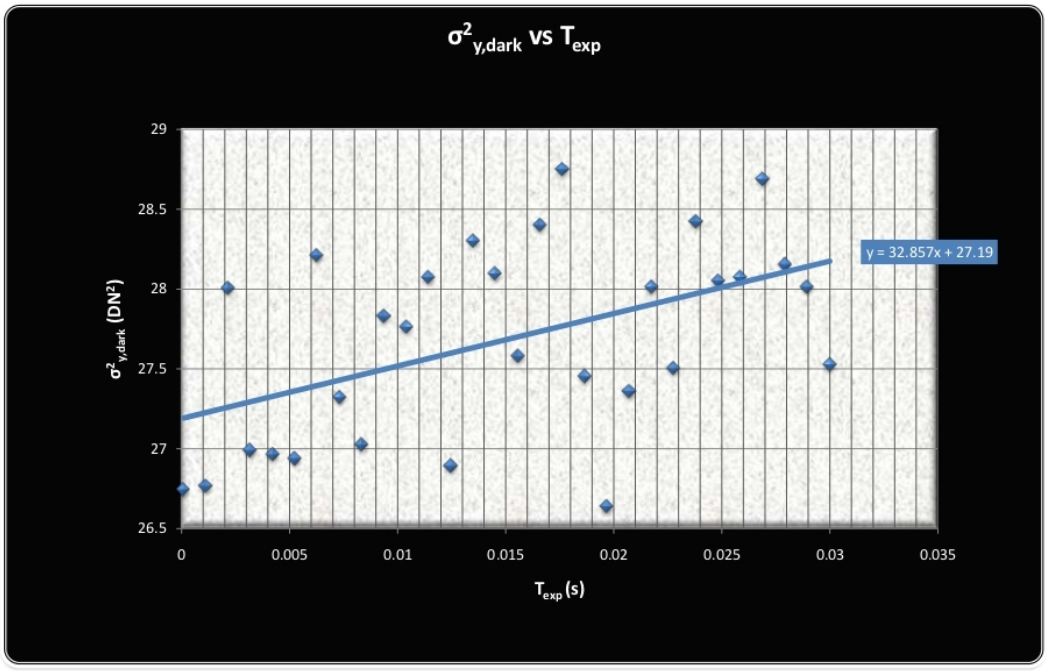

Figure B.4: The graph for the dark current calculation. The variance σ^2 of dark images were plotted against the exposure time in s. By means of the slope and the inverse overal system gain $1/K$ the dark current can be determined.

Appendix C

Astrometry Computation

The astrometry method is based on the assumption that a location in the sky can be determined via an image with at least three reference stars. The greater the imaged number of stars is the higher gets the precision of the determination of sky region imaged. The statement is underlaid by a simple computation [MP94]. The sketch in Fig. C.1 shows the path of light occuring from a star at position (α, δ) which is imaged on a point in the camera plane (x, y). The light rays are thereby focused by an objective O with a focal length F which constitutes the origin of a coordinate system a, b, c. In this coordinate system the axis a points towards the right ascension α_0 of the point (α_0, δ_0) where the camera's optical axis crosses the sky. C represents the objective height and b is perpendicular to both axis.

The vector $\vec{e}$ pointing from the origin to the star can be written in terms of the

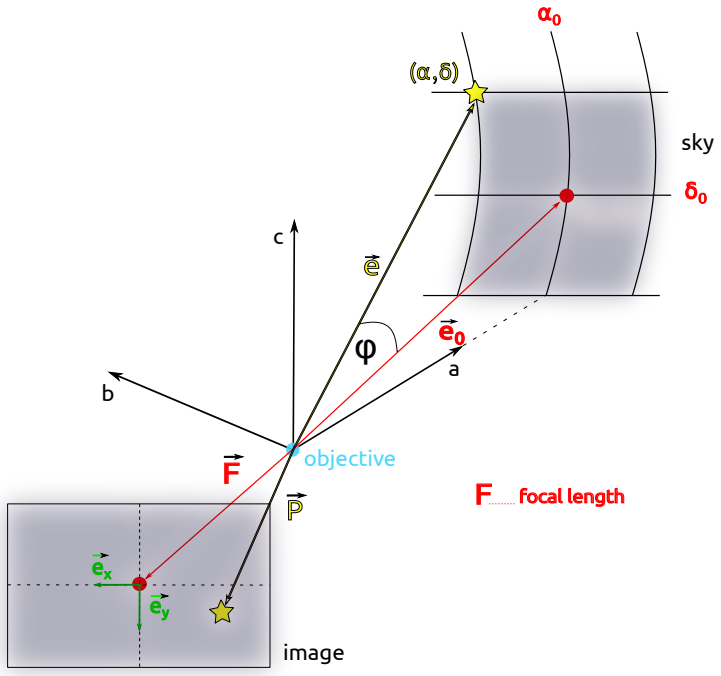

Figure C.1: The vectorial dependencies between a star on the sky and in an image are shown. Due to coordinate transformation the image coordinates can be expressed by the sky's spherical coordinates which is used in the astrometry method.

coordinate system by

$$\vec{e} = \begin{pmatrix} \cos(\delta)\cos(\alpha - \alpha_0) \\ \cos(\delta)\sin(\alpha - \alpha_0) \\ \sin(\delta) \end{pmatrix} \tag{C.1}$$

and its corresponding vector $\vec{e_0}$, which points to the location where the camera's optical axis intercepts the sky, expressed by

$$\vec{e_0} = \begin{pmatrix} \cos(\delta_0) \\ 0 \\ \sin(\delta_0) \end{pmatrix}. \tag{C.2}$$

By means of the vectors and the intrinsic camera parameters the optical path to the image centre is described by $\vec{F} = -F \cdot \vec{e_0}$ and to the imaged star position by $\vec{P} = p \cdot \vec{e}$. The two vectors draw an angle ϕ of

$$\cos(\phi) = \vec{e} \cdot \vec{e_0} = \cos(\delta_0)\cos(\delta)\cos(\alpha - \alpha_0) + \sin(\delta)\sin(\delta_0). \tag{C.3}$$

On the camera plane the unit vectors are orientated to the east-west and north-south direction in the sky which lead to the defintion of the coordinate system with

$$\vec{e_x} = \begin{pmatrix} 0 \\ 1 \\ 0 \end{pmatrix} \quad \text{and} \quad \vec{e_y} = \begin{pmatrix} \sin(\delta_0) \\ 0 \\ -\cos(\delta_0) \end{pmatrix}. \tag{C.4}$$

Due to the defintion of the coordinate system in the image plane, the vector $\vec{P}$ is written as

$$\vec{P} = \vec{F} + (F \cdot x)\vec{e_x} + (F \cdot Y)\vec{e_y} \tag{C.5}$$

by means of point p with coordinates X and Y in units of the focal length. If the equation is written component-by-component the relation between the point (α, δ) and (X, Y) will be expressed by the three equations

$$p \cdot \cos(\delta)\cos(\alpha - \alpha_0) = F \cdot \cos(\delta_0) - F \cdot Y \cdot \sin(\delta_0) \tag{C.6}$$

$$p \cdot \cos(\delta)\sin(\alpha - \alpha_0) = F \cdot X \tag{C.7}$$

$$p \cdot \sin(\delta) = F \cdot \sin(\delta_0) + F \cdot Y \cdot \cos(\delta_0). \tag{C.8}$$

Here p represents the norm of $\vec{P}$ which is described by

$$p = \left|\vec{P}\right| = \sqrt{1 + X^2 + Y^2}$$

or

$$p = \frac{F}{\cos(\phi)} = \frac{F}{\cos(\delta_0)\cos(\delta)\cos(\alpha - \alpha_0) + \sin(\delta)\sin(\delta_0)}.$$

Solving the equation for the star's right ascension α and declination δ yields after several conversions their relation in terms of the spherical coordinates

$$\alpha = \alpha_0 + \arctan\left(\frac{-X}{\cos(\delta_0) + Y \cdot \sin(\delta_0)}\right) \tag{C.9}$$

$$\delta = \arcsin\left(\frac{\sin(\delta_0) + Y \cdot \cos(\delta_0)}{\sqrt{1 + X^2 + Y^2}}\right). \tag{C.10}$$

The inverse of the equation is yielded by following the same procedure as before and is given by

$$X = -\frac{\cos(\delta)\sin(\alpha-\alpha_0)}{\cos(\delta)\cos(\delta_0)\cos(\alpha-\alpha_0)+\sin(\delta)\sin(\delta_0)} \tag{C.11}$$

$$Y = -\frac{\sin(\delta_0)\cos(\delta)\cos(\alpha-\alpha_0)-\sin(\delta)\cos(\delta_0)}{\cos(\delta)\cos(\delta_0)\cos(\alpha-\alpha_0)+\sin(\delta)\sin(\delta_0)}\ . \tag{C.12}$$

The non-dimensional coodinates X and Y are the standard coordinates since they do not depend on the optic's focal length. Moreover, they correspond to the coordinate system whose right ascension and declination lines are strongly parallel to the centre (α_0, δ_0) of the image.
For a conversion into standard coordinates, the measured coordinates are divided by the focal length

$$X = \frac{x}{F} \quad Y = \frac{Y}{F}. \tag{C.13}$$

Usually the origin of the used coordinate system does not match with the intercept of the optical axis with the image plane, therefore the standard coordinates are modified by adding a small shift $(\Delta x, \Delta y)$ to their equation

$$X = \frac{x}{F} - \frac{\Delta x}{F} \quad Y = \frac{Y}{F} - \frac{\Delta y}{F}. \tag{C.14}$$

Additional effects influence the relation between the measured and the standard coordinates, e.g. optical aberrations or rotation of the coordinate axis. For this purpose a general ansatz is assumed where the standard coordinate is not only influenced by its corresponding measured coordinate but also from the other

$$\begin{aligned} X &= a \cdot x + b \cdot y + c \\ Y &= d \cdot x + e \cdot y + f. \end{aligned}$$

Here a, b, c, d, e, f represent the so-called plate constants which include the effects influencing the difference between the coordinates. If the equatorial coordinates $(\alpha_i, \delta_i)_{i=1,2,3}$ of three reference stars are known, the corresponding standard coordinates $(X_i, Y_i)_{i=1,2,3}$ with their corresponding measured coordinates $(x_i, y_i)_{i=1,2,3}$ results from

$$\begin{aligned} X_1 &= a \cdot x_1 + b \cdot y_1 + c \\ X_2 &= a \cdot x_2 + b \cdot y_2 + c \\ X_3 &= a \cdot x_3 + b \cdot y_3 + c. \end{aligned}$$

The same relations are yielded for the Y coordinate. Due to the three reference stars, the system of equations is completely determined and the precision of the constants improves by a greater number of stars in the image plane.

Bibliography

[AAA+09a] VA Acciari, E. Aliu, T. Arlen, M. Beilicke, W. Benbow, M. Böttcher, SM Bradbury, JH Buckley, V. Bugaev, Y. Butt, et al. Veritas observations of a very high energy γ-ray flare from the blazar 3c 66a. *The Astrophysical Journal Letters*, 693(2):L104, 2009.

[AAA+09b] E. Aliu, H. Anderhub, LA Antonelli, P. Antoranz, M. Backes, C. Baixeras, S. Balestra, JA Barrio, H. Bartko, D. Bastieri, et al. Discovery of a very high energy gamma-ray signal from the 3c 66a/b region. *The Astrophysical Journal Letters*, 692(1):L29, 2009.

[AAA+09c] WB Atwood, Aous A Abdo, M Ackermann, W Althouse, B Anderson, M Axelsson, L Baldini, J Ballet, DL Band, G Barbiellini, et al. The large area telescope on the fermi gamma-ray space telescope mission. *The Astrophysical Journal*, 697(2):1071, 2009.

[AAA+10] J. Aleksić, LA Antonelli, P. Antoranz, M. Backes, JA Barrio, D. Bastieri, J.B. González, W. Bednarek, A. Berdyugin, K. Berger, et al. Observations of the blazar 3c 66a with the magic telescopes in stereoscopic mode. *The Astrophysical Journal*, 726(2):58, 2010.

[AAA+11] M. Actis, G. Agnetta, F. Aharonian, A. Akhperjanian, J. Aleksić, E. Aliu, D. Allan, I. Allekotte, F. Antico, LA Antonelli, et al. Design concepts for the cherenkov telescope array cta: an advanced facility for ground-based high-energy gamma-ray astronomy. *Experimental Astronomy*, pages 1–124, 2011.

[Adm13] Administrator. Veritas - the very energetic radiation imaging telescope array system, jan 2013.

[AKL+96] F Arqueros, A Karle, E Lorenz, S Martinez, R Plaga, and M Rozanska. Separation of gamma and hadron initiated air showers with energies between 20 and 500 tev. *Astroparticle Physics*, 4(4):309–332, 1996.

[Bae12a] J. Baehr. Modification of camera lens. private communication, 2012.

[Bae12b] J. Baehr. Status of the cta medium size telescope prototype. *arXiv preprint arXiv:1212.3110*, 2012.

[BBG+12] B. Behera, J. Bähr, S. Grünewald, G. Hughes, I. Oya, D. Melkumyan, S. Schlenstedt, and U. Schwanke. Optical design and calibration of a medium size telescope prototype for the cta. In *SPIE Astronomical Telescopes+ Instrumentation*, pages 844417–844417. International Society for Optics and Photonics, 2012.

[BCC+03] K Bernlöhr, O Carrol, R Cornils, S Elfahem, P Espigat, S Gillessen, G Heinzelmann, G Hermann, Werner Hofmann, D Horns, et al. The optical system of the hess imaging atmospheric cherenkov telescopes. part i: layout and components of the system. *Astroparticle Physics*, 20(2):111–128, 2003.

[BCH+12] E Birsin, J Colomé, D Hoffmann, H Koeppel, G Lamanna, T Le Flour, A Lopatin, E Lyard, D Melkumyan, I Oya, et al. Towards a flexible array control and operation framework for cta. *arXiv preprint arXiv:1211.5618*, 2012.

[BCS08] K Bernlöhr, E Carmona, and T Schweizer. Mc simulation and layout studies for a future cherenkov telescope array. In *International Cosmic Ray Conference*, volume 3, pages 1469–1472, 2008.

[Beh12] B. Behera. Astrometry.net software proposal. private communication, 2012.

[Bes79] MS Bessel. Ubvri photometry ii. *Publ. Astron. Soc. Pac*, 91:543–589, 1979.

[CFE02] Pierantonio Cinzano, Fabio Falchi, and Christopher D Elvidge. The first world atlas of the artificial night sky brightness. *Monthly Notices of the Royal Astronomical Society*, 328(3):689–707, 2002.

[CGJ+03] R. Cornils, S. Gillessen, I. Jung, W. Hofmann, M. Beilicke, K. Bernlöhr, O. Carrol, S. Elfahem, G. Heinzelmann, G. Hermann, et al. The optical system of the hess imaging atmospheric cherenkov telescopes. part ii: mirror alignment and point spread function. *Astroparticle Physics*, 20(2):129–143, 2003.

[Col13] H.E.S.S. Collaboration. The hess project: an array of imaging atmospheric cherenkov telescopes, jan 2013.

[D+] E Davis et al. Mechanical design of a medium-size telescope for cta. *CTA internal note*.

[DC57] John M Davies and Eugene S Cotton. Design of the quartermaster solar furnace. *Solar Energy*, 1(2):16–22, 1957.

[DE10] J.L.R. Dreyling-Eschweiler. Aufbau und test eines neuartigen ccd-kamerasystems zur kontrolle der optik eines h.e.s.s.-cherenkovteleskops. 2010.

[Dem05] Wolfgang Demtröder. *Experimentalphysik 3: Atome, Moleküle und Festkörper*, volume 3. Springer, 2005.

[Die04] Friedrich Dierks. Sensitivity and image quality of digital cameras. *Image_Quality_of_Digital_Cameras. pdf*, 2004.

[Doe12] R. Doe. Prosilica gc: Brochure, datasheets, manual - allied vision technologies, jan 2012.

[gra12] graftek. Optem - avimo precision instruments: Macro video zoom lens(18-108, f/2.5) - for video applications requiring larger fields-of-view, oct 2012.

[Gru05] C. Grupen. *Astroparticle physics*. Springer, 2005.

[Gyl50] K Gyldenkaerne. Atmospheric tremor and its influence on the intensity distribution of photographic stellar images. In *Annales d'Astrophysique*, volume 13, page 97, 1950.

[Har59] Robert Hardie. An improved method for measuring extinction. *The Astrophysical Journal*, 130:663, 1959.

[HB12] J. A. Hinton and K. Bernloehr. Mst requirements. Internal CTA requirements for MST prototype, dec 2012.

[Her10] German Hermann. Towards the future cherenkov telescope array cta. *Nuclear Instruments and Methods in Physics Research Section A: Accelerators, Spectrometers, Detectors and Associated Equipment*, 623(1):408–409, 2010.

[HFM+00] E. Høg, C. Fabricius, V.V. Makarov, S. Urban, T. Corbin, G. Wycoff, U. Bastian, P. Schwekendiek, and A. Wicenec. The tycho-2 catalogue of the 2.5 million brightest stars. *Astronomy and Astrophysics*, 355:L27–L30, 2000.

[Hil85] A Michael Hillas. Cerenkov light images of eas produced by primary gamma. In *International Cosmic Ray Conference*, volume 3, pages 445–448, 1985.

[How06] S.B. Howell. *Handbook of CCD astronomy*, volume 5. Cambridge Univ Press, 2006.

[HRW+11] D. Hampf, G. Rowell, N. Wild, T. Sudholz, D. Horns, and M. Tluczykont. Measurement of night sky brightness in southern australia. *Advances in Space Research*, 48(6):1017–1025, 2011.

[HWJ95] Dorrit Hoffleit and WH Warren Jr. Bright star catalogue, (hoffleit+, 1991). *VizieR Online Data Catalog*, 5050:0, 1995.

[JMIW66] HL Johnson, RI Mitchell, B Iriarte, and WZ Wisniewski. Ubv photometry of bright stars, commun. *Lunar & Planet. Lab*, 4:99, 1966.

[Kel11] Hanna Kellermann. Measuring the focused reflectivity of the magic mirrors, 2011. Slides of a talk given at DPG, March 28– April 1, 2011, KIT, Karlsruhe, Germany.

[Leo94] W.R. Leo. *Techniques for nuclear and particle physics experiments: a how-to approach*. Springer Verlag, 1994.

[LHM+10] D. Lang, D.W. Hogg, K. Mierle, M. Blanton, and S. Roweis. Astrometry. net: Blind astrometric calibration of arbitrary astronomical images. *The Astronomical Journal*, 139(5):1782, 2010.

[Med12] MediaNord. Walimex pro 85/1.4 datasheet, dec 2012.

[MHKM10] A. McCann, D. Hanna, J. Kildea, and M. McCutcheon. A new mirror alignment system for the veritas telescopes. *Astroparticle Physics*, 32(6):325–329, 2010.

[MLC+07] D.G. Monet, S.E. Levine, B. Canzian, H.D. Ables, A.R. Bird, C.C. Dahn, H.H. Guetter, H.C. Harris, A.A. Henden, S.K. Leggett, et al. The usno-b catalog. *The Astronomical Journal*, 125(2):984, 2007.

[MP94] Oliver Montenbruck and Thomas Pfleger. Astronomie mit dem personal computer. *Astronomie mit dem Personal Computer., by Montenbruck, O.; Pfleger, T.. Springer, Berlin (Germany), 1994, 317 p., ISBN 3-540-57701-7, Price DM 78.00.*, 1, 1994.

[OBB+12] I. Oya, B. Behera, E. Birsin, H. Koeppel, D. Melkumyan, T. Schmidt, U. Schwanke, P. Wegner, S. Wiesand, M. Winde, et al. Evaluating the control software for cta in a medium size telescope prototype. In *Journal of Physics: Conference Series*, volume 396, page 012037. IOP Publishing, 2012.

[odt13] opencv dev team. Camera calibration and 3d reconstruction, mar 2013.

[OG12] L. Oakes and S. Grünewald. Analysing program with gaussian fit function. private communication, 2012.

[Ope08] Learning OpenCV. Computer vision with the opencv library. *Gary Bradski, Adrian Kaehler*, 2008.

[Rot09] Günter D Roth. *Handbook of practical astronomy*. Springer, 2009.

[Sch01] V. Schönfelder. *The universe in gamma rays*. Springer, 2001.

[Sch13] A. Schubert. Current sensor arrangement. Internal sensor arrangement for MST prototype, feb 2013.

[SHLK87] L. Strüder, P. Holl, G. Lutz, and J. Kemmer. Development of fully depletable ccds for high energy physics applications. *Nuclear Instruments and Methods in Physics Research Section A: Accelerators, Spectrometers, Detectors and Associated Equipment*, 257(3):594–602, 1987.

[Sze08] S.M. Sze. *Semiconductor devices: physics and technology*. John Wiley & Sons, 2008.

[T+98] S.A. Taylor et al. Ccd and cmos imaging array technologies: technology review. *Relatorio tecnico EPC-1998-106, Cambridge Laboratory*, 1998.

[TBS+11] M. Teshima, O. Blanch, T Schweizer, J. A. Barrio, L. Brunetti, E. Carmona, P. Colin, J. Cortina, F. Dazzi, G. Deleglise, et al. Design study of a cta large size telescope (lst). In *Proc. of the 32nd Int. Cosmic Ray Conf., 32nd International Cosmic Ray Conference*, volume 9, page 149, 2011.

[Tea11] NASA/DOE/International LAT Team. The fermi lat all-sky map, dec 2011.

[Tea12] ROOT Development Team. Root - a data analysis framework, October 2012.

[VCM+13] S Vercellone, O Catalano, MC Maccarone, F Di Pierro, P Vallania, G Bonnoli, R Canestrari, G Pareschi, G Tosti, et al. The astri project: prototype status and future plans for a cherenkov dual-mirror small-telescope array. *arXiv preprint arXiv:1303.2024*, 2013.

[vE13] Christopher van Eldik. Discussion about ccd cameras. communication during a pointing meeting, 2013.

[VFB07] V. Vassiliev, S. Fegan, and P. Brousseau. Wide field aplanatic two-mirror telescopes for ground-based γ-ray astronomy. *Astroparticle Physics*, 28(1):10–27, 2007.

[Wag12] Robert Wagner. The magic telescopes, nov 2012.

[Wee03] T.C. Weekes. *Very high energy gamma-ray astronomy*. Taylor & Francis, 2003.

[wik12a] Veritas wiki webpage, mar 2012.

[Wik12b] Wikimedia. H.e.s.s. ii telescope array, dec 2012.

[WMD10] S. Weisse, D. Melkumyan, and P. Duval. Status, applicability and perspective of tine-powered video system, release 3. *PCaPAC2010*, 2010.

[WOE+00] M. Wenger, F. Ochsenbein, D. Egret, P. Dubois, F. Bonnarel, S. Borde, F. Genova, G. Jasniewicz, S. Laloe, S. Lesteven, et al. The simbad astronomical database. *Astronomy and Astrophysics Supplement Series*, 143(1):9–22, 2000.

[WT77] Trevor C Weekes and KE Turver. Gamma-ray astronomy from 10-100 gev: A new approach. In *Recent Advances in Gamma-Ray Astronomy*, volume 124, pages 279–286, 1977.

Selbständigkeitserklärung

Hiermit versichere ich, dass ich die vorliegende Arbeit selbständig verfasst und keine anderen als die angegebenen Quellen und Hilfsmittel verwendet habe.

Berlin, den 17. Juni 2013 Sandra Grünewald